ABSTRACT

Title of Dissertation: Atomistic Exploration of Water and Salt Confined in Sub-Nanometer and Nanometer Wide Boron-Nitride Nanotubes.

Bhargav Sai Chava, Doctor of Philosophy, 2023

Dissertation directed by: Professor Siddhartha Das, Department of Mechanical Engineering, University of Maryland.

In my dissertation, I will use atomistic simulations to study the behavior of water and salt solutions confined in sub-nanometer and nanometer wide boron nitride nanotubes (BNNTs). This study will provide fundamental insight into the effect of nanoconfinement on a) the structure of water-in-salt electrolytes (WiSEs) inside nanometer-wide BNNTs, b) structure, filling thermodynamics, and hydrogen bond (HB) kinetics and strength for water confined in BNNTs of various diameters.

For the past few decades, nanoconfined fluids are being actively researched by scientists and engineers due to their interesting properties that are absent in their bulk counterparts. Such fluids could play a crucial role in developing novel nanofluidic devices for application in the fields of energy storage, membrane separation, and bioengineering. In the context of nanoconfined

fluids, nanotubes are a very popular choice as structures used for confining these fluids. Among them, carbon nanotubes (CNTs) and boron nitride nanotubes (BNNTs) are two of the most well-studied nanotubes. They exhibit outstanding mechanical properties, chemical stability, and thermal conductivity. However, their electronic properties are dissimilar. CNTs are known to be semiconducting materials, while BNNTs are regarded as electrical insulators. These properties make each of these nanotube types quite unique. Also, due to the polar nature of the B-N bonds, the behavior of the fluid confined inside the BNNT is distinctly different compared to the fluid confined inside the CNT.

In chapter 2, I use all-atom molecular dynamics (MD) simulations to report a novel non-covalent endohedral nanotube-salt-water hybrid formed by confining a 10 molal (m) LiTFSI aqueous solution inside a (7, 7) BNNT that has an internal diameter comparable to the size of the TFSI anion. The simulation reveals that $TFSI^-$ ions and hydrated Li^+ ions form axially non-overlapping periodic blocks inside the (7, 7) BNNT. Also, the TFSI anions are immobile inside the hybrid, and as a result, traps the water encapsulated in between them. These circumstances lead to an interesting scenario where the entrapped water is confined in all directions resulting in zero-dimensional water blocks. Further, water exists in a liquid state in these zero-dimensional blocks. Finally, it is demonstrated (by detailed free energy curves) that this hybrid is stable against increasing temperature and the change of the surrounding chemical composition.

In chapter 3, I use all-atom MD simulations to show that water free localization of a $TFSI^-$ ion at the negative electrode is possible for a moderately concentrated LiTFSI based WiSE confined inside a 1-nm diameter BNNT. I explain this possibility as a combined effect of the affinity of the $TFSI^-$ ion to enter an empty nanometer-wide BNNT prior to other electrolyte molecules, and the size of the $TFSI^-$ being comparable to the diameter of the BNNT.

In chapter 4, I use ReaxFF MD simulations to study the water structure and thermodynamics inside BNNTs of various diameters. This study shows that water is thermodynamically more stable when confined inside BNNTs compared to bulk water. Also, entropic favorability is found to be the predominant factor in stabilizing BNNT-confined water despite the mild hydrophilicity of hexagonal boron nitride. Further, the factors dictating the entropic favorability varies with the BNNT diameter due to significant changes in water structure.

In chapter 5, I explore the effect of BNNT based confinement on the water hydrogen bond kinetics and strength. First, appropriate water HB definitions were devised for BNNT-confined water systems (with varying degrees of confinement). Using these definitions, pairs of water molecules with HB configurations are identified and the corresponding HB kinetics and strengths are quantified.

Atomistic Exploration of Water and Salt Confined in Sub-Nanometer and Nanometer Wide Boron-Nitride Nanotubes

by

Bhargav Sai Chava

Dissertation submitted to the Faculty of the Graduate School of the
University of Maryland, College Park, in partial fulfillment
of the requirements for the degree of
Doctor of Philosophy
2023

Advisory Committee:
Associate Professor Siddhartha Das, Chair
Assistant Professor Po-Yen Chen
Associate Professor Amir Riaz
Assistant Professor Pratyush Tiwary
Associate Professor Yifei Mo, Dean's Representative

Acknowledgements

I am grateful to my advisor, Dr. Siddhartha Das, for the continuous guidance and support. I thank my colleagues and my dissertation committee for their contribution to my dissertation. I acknowledge the computational support obtained from the Deepthought2 High-Performance Computing cluster at the University of Maryland.

Table of Contents

List of Abbreviations

Carbon nanotube (CNT)

Boron nitride nanotube (BNNT)

Molecular Dynamics (MD)

Water-in-salt electrolyte (WiSE)

Reactive Force Field (ReaxFF)

Hydrogen Bond (HB)

List of Figures

List of Tables

Chapter 1: Background and Motivation

1.1. Overview

Nanoconfined fluids have gained a lot of attention from scientists and engineers for the past few decades with the accelerated evolution of nanotechnology.[1] Such fluids were shown to exhibit remarkable properties that cannot be seen in their bulk counterparts. Exploration of such properties is not only of great importance to the progress of fundamental science, but also plays a crucial role in advancing many application-driven fields. Few of the industrial applications that take advantage of the unique properties of nanoconfined fluids include energy storage,[2] membrane technology,[3] and bioengineering.[4] Nanotubes are one of the common confining structures used in many studies involving nanoconfined fluids. These nanostructures come in a wide range of pore sizes, which directly affect the degree of confinement and therefore, the behavior of fluids confined in them. Carbon nanotubes (CNTs) and boron nitride nanotubes (BNNTs) are two of the most widely investigated nanotubes with CNT being the focus of numerous experimental and theoretical studies.[5-15] Unlike the C-C bonds in CNTs, the B-N bonds in BNNTs are polar in nature: accordingly, there are significant disparities in the structure and dynamics of water and salt solutions confined in these two types of nanotubes. While both the types of nanotubes possess excellent mechanical and thermal properties, their electronic properties are contrasting. BNNTs, for example, have a wide band gap of 5-6 eV making them excellent electric insulators; on the other hand, CNTs behave as semiconducting materials.[16] These characteristics make BNNTs desirable for applications requiring electric insulators with high thermal stability. Figure 1.1 shows the schematic of a BNNT with a chiral index of (7, 7) which corresponds to a diameter of approximately 1 nm.

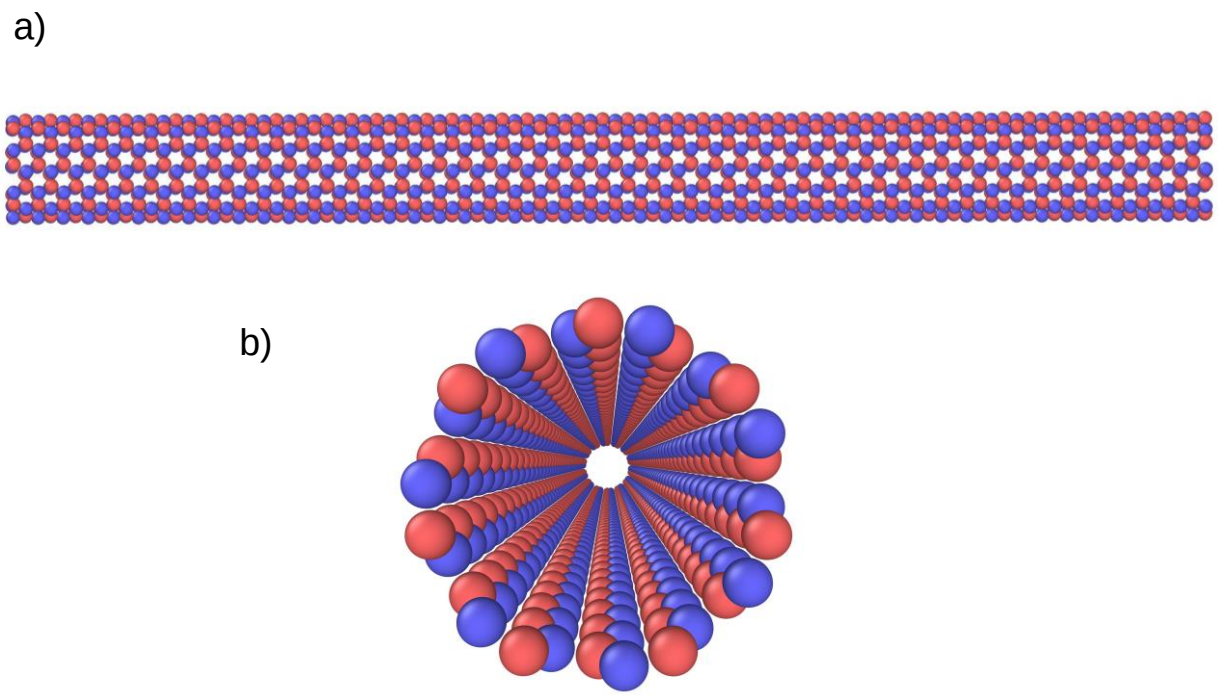

Figure 1.1 a) Axial and b) cross sectional view of a (7, 7) BNNT

Molecular dynamics (MD) simulations are an indispensable tool to explore the structural and dynamic properties of materials at an atomic-level resolution. In this thesis, we use (MD) simulations to study the behavior of water and salt solutions confined in sub-nanometer and nanometer wide BNNTs. We will explore the structure and filling behavior of moderately concentrated water-in-salt electrolytes (WiSE) confined in nanometer-wide BNNTs. Furthermore, the effect of the applied voltage on these properties will be investigated for potential applications in aqueous Li-ion batteries. Later, we will study the water hydrogen bond (HB) strength and the

thermodynamics dictating the water structure and density in BNNTs of various diameters. In addition, we will probe the effect of vacancy defects in BNNTs on the water friction confined in them. Finally, we will analyze the effects of confinement on the chemisorption of hydroxide ion at the inner surface of a BNNT.

1.2. Water-in-Salt Electrolytes Confined in Nanometer-wide BNNT: Effect of Confinement and Voltage on Structure and Filling Behavior

Water-in-salt electrolytes (WiSEs) refer to extremely large salt concentrations in an aqueous medium. The typical characteristic of WiSE systems is that the salt outnumbers water by both weight and volume, and some of the water molecules in the cation's hydration shell are replaced by anions. Recently, highly concentrated LiTFSI based WiSE systems have been found to enhance the electrochemical stability window of aqueous Li-ion batteries. Augmented ion pairing and a lack of free water in these systems have been found to be the primary reasons for the enhanced electrochemical stability.[17]

Previous computational works have shown that boron nitride sheet dispersion is thermodynamically more favorable in ionic liquids, containing $TFSI^-$ anion, compared to pure water.[18] Also, recent studies involving experiments and DFT calculations showed that hexagonal boron nitride induces trapping of $TFSI^-$ anion.[19] In addition to these results, the size of the $TFSI^-$ anion leads to some interesting questions as to how confinement in a nanometer-wide BNNT affects the structure and filling behavior of concentrated LiTFSI aqueous electrolytes. In chapters 2 and 3, we use all-atom MD simulations to answer these questions and assess the potential of

these nanoconfined aqueous electrolytes for application in aqueous Li-ion batteries and hybrid materials.

1.3. Water Confined in BNNTs

The exploration of structure and transport properties of nanoconfined water is of great relevance for developing state of the art nanofluidic systems. For specific applications requiring water confined in an electrically insulating, chemically and thermally stable nanostructure, BNNT is an excellent choice. Many previous MD studies have reported the structure and dynamics of water confined in BNNTs of various diameters.[15, 20, 21, 22] However, most of these studies use force field parameters that significantly underpredict the water contact angle on boron nitride (BN). The force field used in the above studies predict a water contact angle of 30° while the recent experimental studies report a water-BN contact angle of 66°.[23] Results from the above studies show that water spontaneously fills a (5, 5) BNNT and forms a steady continuous single file water in (5, 5) and (6, 6) BNNTs which could be a result of the overestimation of BNNT's hydrophilicity.[15, 20, 21] In chapter 4, I perform reactive MD simulations using the recently reported ReaxFF parameters which predict a water-BN contact angle of ~70°.[24] Here, I study the structure and the filling thermodynamics for water confined in BNNTs of various diameters. In chapter 5, I study the effect of BNNT induced confinement on the water hydrogen bond strength and kinetics using the above described ReaxFF MD simulations.

The contents of this chapter have been published as Chava, B. S., Wang, Y., & Das, S. (2021). Boron Nitride Nanotube–Salt–Water Hybrid: Toward Zero-Dimensional Liquid Water and Highly Trapped Immobile Single Anions Inside One-Dimensional Nanostructures. *The Journal of Physical Chemistry C*. *125*, 25, 14006–14013

Chapter 2: Boron-Nitride-Nanotube-Salt-Water Hybrid: Towards Zero-Dimensional Liquid Water and Highly Trapped Immobile Single Anions Inside One-Dimensional Nanostructures*

Abstract

Nanotube-molecules-based hybrid structures, where different chemical species are integrated with the nanotubes either exohedrally (i.e., attached on outer surface of the nanotubes) or endohedrally (i.e., encapsulated within the nanotubes) has enabled developing novel materials with unprecedented application potentials. In this paper, we describe our simulation-driven discovery of endohedral and non-covalent nanotube-salt-water (boron-nitride-nanotube-LiTFSI-water) hybrid structure, which forms when a 1-nm-diameter boron-nitride nanotube (BNNT), placed in a large-concentration LiTFSI electrolyte solution, gets filled with periodically repeating and axially separated non-overlapping blocks of TFSI anion and Li-ion-solvating water. In this hybrid structure, the TFSI anions are in highly trapped immobile state, while the water blocks are in a zero-dimensional configuration and a liquid (non-crystalline) state. Furthermore, subjecting the hybrid to elevated temperature or salt-free surrounding has little effect on the structure and properties of this hybrid. This, along with separate free energy simulations, confirms the most remarkable stability of this nanotube-salt-water hybrid system.

2.1 INTRODUCTION

Nanotubes (e.g., carbon nanotubes or CNTs, boron nitride nanotubes or BNNTs), characterized as hollow tubes with internal diameters ranging from few to tens of nanometers have emerged as most remarkable one-dimensional nanostructure that have found wide-scale

application in fabrication of sensors, transistors, conductors, batteries, energy-storage materials, light-emitting diodes, lithium-ion batteries, supercapacitors, light-weight composites, and flexible electronics as well as in applications such as waste-water treatment, water purification, chromatography, voltammetry, solid-phase extraction of drugs and biomolecules, drug targeting, controlled drug release, disease diagnosis and treatment, enabling anti-bacterial and anti-fungal properties, and many more.[16,25-35] While many of these applications use these nanotubes as filler materials for improving the properties of certain macroscopic materials (e.g., adding CNTs for improving the mechanical, thermal, and electric properties of CNT-polymer-based nanocomposites[36-39] or using CNTs to prepare mixtures/pastes that can be used for printing temperature sensors[40,41] and fabricating anti-bacterial coatings[42,43]), more exciting classes of studies and future applications (e.g., use as high-performance membranes,[44] or use in futuristic water treatment technologies,[45] or promoting specific chemical reactions[46]) involve probing the properties and transport of water, ions, and other species (e.g., alcohol, dyes, etc.) remaining encapsulated within or transporting through a single CNT or BNNT.[5,21,22,47-60] For example, water encapsulated within CNTs or BNNTs demonstrate one-dimensional structure with most fascinating properties.[5-9] Similarly, gas-filled CNTs have been touted to be used as nano-resonators with unprecedented properties.[10-12] Also, there have been massive interests in probing the behavior of nanotube-encapsulated salt systems.[13-15,61] One such example, where other species have been closely integrated with nanotubes are nanotube-molecules-based hybrid systems. Over the last several years, there has been a massive recent interest in designing and developing such nanotube-molecules-based hybrid systems,[62] where certain molecules get integrated with the nanotubes eventually enabling engineering of new materials with outstanding opto-electronic, magnetic, and other properties. These hybrid structures often appear as systems where these molecules are bound

to the nanotubes as side-attached structures (these structures are also identified as exohedral functionalized nanotube hybrids).[63-69] The examples include hybrid structures consisting of single-walled CNT-tetraphenylporphyrines (SWCNT/TPP)[63] or SWCNT-pyrelene derivatives for optical applications,[64] hybrid structures obtained by reacting CNTs with azidodichloro-triazine 1 and showing improved photo-luminescence behavior,[65] CNT-single-molecule-magnet-$TbPc_2$ hybrids demonstrating giant magnetoresistance,[66] CNT-tetrairon-III-single-molecule-magnet hybrid,[67] CNT-quantum-dots nanohybrids with DNA linkers showing improved optoelectronic performances,[68] DNA-SWCNT hybrid for detecting salt-concentration-dependent nucleobase distribution,[69] etc. Nanotube-based hybrid structures have also been studied for BNNTs (Boron Nitride Nanotubes). They include defect-induced formation of the BNNT-boron-nitride-nanosheet exohedral hybrids,[70] BNNT-nucleobases hybrid systems where the nucleobases have been physiosorped on the BNNT outer surface,[71] formation of structures where BNNTs are wrapped on their outer surfaces by ss-DNA molecules,[72] formation of hybrids where amphiphilic monomethoxy-poly(ethylene glycol)-*b*-poly(epsilon- caprolactone) diblock copolymers are attached as side structures to hydroxylated BNNTs,[73] etc. On the other hand, there are also several examples where such nanotube-based hybrids have been formed with the molecules (or other species) entering the nanotube and getting localized within the nanotubes (in other words, the hybrids are formed between the nanotubes and the moieties getting encapsulated within the nanotubes; these configurations are also known as endohedrally functionalized nanotube hybrids).[74-76] These include cases such as CNT-encapsulated DySc2N@C80-Single-Molecule-Magnetic-Metallofullerene hybrid demonstrating improved coercivity,[74] CNT-encapsulated-Mn_{12}Ac-Single-Molecule-Magnetic hybrid with possible applications in fabricating high-density magnetic data storage devices,[75] SWCANT-DANS (DANS: *p,p'-dimethylaminonitrostilbene*)

hybrid providing highly enhanced non-linear optical (NLO) response,[76] BNNT-based endohedral hybrid structures formed with BNNTs encapsulating and stabilizing polymeric nitrogen,[77] and BNNTs-based hybrids where coronene-based graphene nanoribbons are encapsulated in BNNTs.[78]

In this paper, we report our simulation-driven discovery of non-covalent and endohedral BNNT-LiTFSI-salt-water hybrid, where TFSI anions and Li-cation-solvating water blocks are encapsulated within a 1-nm-diamter BNNT. Within this hybrid, single TFSI anion and the water molecules appear as non-overlapping and periodically repeating axial blocks. This hybrid forms when (a) an empty BNNT is placed in a concentrated (10 m) LiTFSI aqueous solution and a single TFSI anion, due to its great affinity to the boron nitride,[19] enters the BNNT followed by the entry of the Li-cation-solvating water molecules and (b) this process of one-after-another entry of TFSI anion and Li-cation-solvating water molecules progresses until the BNNT is completely filled.[61] Interestingly, this formation does not involve any chemical bond formation: TFSI anions have large affinity towards BNNT that makes it enter the tube first and subsequently the electrostatic effects pulls the Li-ion-solvating water molecules inside the BNNT. We next study the properties of the TFSI ions and water pockets (constituting the BNNT-LiTFSI-salt-water hybrid) encapsulated within the BNNT. First, we establish that the TFSI ions are extremely strongly trapped and therefore demonstrate very little mobility or displacement. Such trapping of the TFSI ions by boron nitride has also been reported previously;[19] however, the diffusivity of the TFSI anions is significantly smaller in the present case. Second, we show that the water blocks (constituting the hybrid), trapped by the TFSI anions on either side, exhibit mobility that confirms the zero-dimensional nature of the water molecules within the hybrid. Therefore, within a nanostructure (namely nanotubes), where water is known to exist in a one-dimensional chain like structure,[7,51,79-81] we propose the existence of zero-dimensional water. While Abe *et al.* has

identified such zero-dimensional water in nanoconfined ionic liquids,[82] in general such zero-dimensional water has not been extensively observed. Third, we quantify the RCF (Re-orientational correlation function) of the dipole vectors of this zero-dimensional water establishing that the water, despite its zero-dimensional behavior, is in a non-crystalline liquid state.[83] Finally, we quantify the stability of this proposed BNNT-LiTFSI-water hybrid. The hybrid system is subjected to a significant increase in temperature as well as a significant change in the surrounding system (all the salt from the surrounding system is removed). Under either of these conditions, there is little change in the structure of the hybrid, or in the corresponding mobility of the TFSI ions, or in the zero-dimensional nature and crystallinity of the entrapped water. These findings, along with separate free energy calculations confirming a large free energy barrier experienced by the TFSI ions at the two ends of the BNNT against diffusing into the surrounding medium (consisting of salt-free water) from inside the BNNT, establish the remarkably large stability of the BNNT-LiTFSI-water hybrid structure. Such stability of the hybrid points to the exciting possibility of employing such hybrids in conditions that is vastly different from that in which they were fabricated.

In summary, the main target of this study is to use computations to shed light on the existence and the properties of a new type of nanotube-based material: namely, a BNNT based endohedral nanotube-salt-water hybrid (i.e., a new kind of endohedral nanotube-molecule hybrid). There has been a plethora of studies probing the interactions between nanotubes of different materials and dimensions with large concentrations of electrolyte salts: however, such a unique observation in the context of forming a new kind of material through such interactions has not been probed before. The ease of formation of such BNNT-salt-water hybrid makes it even more attractive: simulations predict that the moment a 1-nm-diameter BNNT is introduced inside a bulk

electrolyte solution of LiTFSI salt of large concentration, the attraction between the BNNT and the TFSI anions, followed by the electrostatic effect driven interactions, lead to the formation of such hybrids. The second facet is the structure of this hybrid: the large size of the TFSI anions (*i.e.*, large enough to be comparable to the internal diameter of the 1-nm-diameter BNNT) ensures that the hybrid is characterized by the presence of periodically repeating and non-overlapping blocks of TFSI anion and solvated Li cation. Such a structure eventually dictates all the salient properties of the hybrid, namely, (1) very weak mobility of the anions, (2) existence of water in zero-dimensional, yet non-crystalline water state, and (3) tremendous stability against different perturbations. In this present paper, we introduce the idea that such a structure is an example of an endohedral nanotube-salt-water hybrid: therefore, we identify this structure as a unique and new kind of nanotube-based nanomaterial. Furthermore, we unravel some of the most intriguing properties of the species (TFSI anion and water molecules) constituting this endohedral hybrid. These properties are unique in the sense that they are not commonly encountered in other systems. For example, we witness an almost immobile state of the TFSI anion, the existence of water in a zero-dimensional state despite being confined within a one-dimensional nanostructure, the existence of water in non-crystalline liquid state despite being in zero-dimensional state, and extreme stability of this entire hybrid structure (as well as extreme propensity of the individual constituents to maintain their respective states and properties) against different perturbations.

2.2 METHODS

We used the LAMMPS[84] parallel Molecular Dynamics (MD) package to perform all the simulations. The temperature and pressure were maintained at desired values using Nosé Hoover[85, 86] thermostat and barostat with damping constants of 100fs and 1000fs respectively. LiTFSI was

modeled using CL&P[87] force field parameters. Water was simulated using the SPC/E model.[88] BNNTs were simulated using the Tersoff potential[89,90] with the non-bonded force field parameters reported by Won and Aluru.[20,91] We used the geometric mixing rules to obtain the interatomic Lennard Jones (LJ) parameters and a cutoff distance of 12 Å for both the LJ and Columbic interactions. The long-range electrostatic interactions were calculated using the PPPM[92] solver with an accuracy of 0.0001. We outputted the data every 500 fs, and a time step of 1fs was used for all the simulations.

The BNNT-salt-water hybrid was formed by soaking a (7, 7) BNNT (1-nm diameter) in a 10 m (molal) LiTFSI aqueous solution. The BNNT is 10 nm long with 1120 atoms and was generated using VMD.[93] We used 1380 LiTFSI pairs and 8280 water molecules to generate the 10 m LiTFSI aqueous solution. The simulation box was initially filled with the solution atoms leaving enough space in the middle of the box to fit the BNNT. First, the solution surrounding the BNNT was pre-equilibrated for 100 ps in the isothermal-isobaric (NPT) ensemble with a temperature of 300 K and a pressure of 1 atmosphere. During this pre-equilibration, the ends of the BNNT were blocked to prevent filling at this stage. After the initial pre-equilibration, the aqueous LiTFSI solution was allowed to fill the nanotube. Also, we observed that anion enters the tube first from both of its ends. So, to prevent the initial trapping of anions inside the 1-nm-diameter BNNT, the solution was allowed to enter and fill the BNNT only through one of the two entrances. Once the BNNT is completely filled, the block was removed and the system was allowed to equilibrate. The simulation was performed in the isothermal-isobaric (NPT) ensemble with the temperature and pressure maintained at 300 K and 1 atmosphere, respectively. Periodic boundary conditions were used in all directions. Atoms at both ends of the BNNT were tethered to harmonic springs (k = 23

kcal/mol.Å^2), preventing the nanotube from drifting away. The simulation lasted for 20 ns with a production run of 10 ns used for data analysis. Equilibrated system configuration obtained from the above simulation was used as the initial state for follow-on simulations where the nanotube hybrid was surrounded by (a) 10 m LiTFSI at 350 K and (b) pure water at 300 K. For the latter case, the LiTFSI aqueous solution surrounding the nanotube hybrid was replaced by pure water consisting of 10,000 water molecules. Both the systems were further simulated in the NPT ensemble for 20 ns, and the data gathered from the last 10 ns was used for analysis.

Finally, we used the umbrella sampling method to obtain free energy curves as a function of the axial positions of centers of mass (COM) of the LiTFSI pairs at both ends of the BNNT-salt-water hybrid in a pure water environment. In each sampling simulation, the axial position of the center of mass of the LiTFSI pair at one of the ends was confined to a window centered at a specific location along the reaction coordinate using a harmonic potential with the stiffness ranging from 1-5 kcal/mol.Å^2 for various simulations. We used windows with z = -4, -3, -2, 0, 2 and 4 Å, and z = 95, 97, 99, 101 and 103 Å, as equilibrium positions for the harmonic potential, for the lower (near z = 0 Å) and upper (near z = 100 Å) LiTFSI pairs respectively. The radial position of the sample LiTFSI pair was confined within 5 Å about the BNNT axis using a cylindrical LJ wall outside the BNNT. Simulation snapshots of the nanotube hybrid in different windows are given in Fig. A1 of the appendix A. All the sampling simulations lasted for 4 ns. These simulations were performed in the NPT ensemble at a temperature of 300 K and a pressure of 1 atmosphere. The axial position of the COM of the sample LiTFSI pair was collected every 500 fs from the last 3.5 ns of each simulation. We used the weighted histogram analysis method (WHAM)[85, 86] to analyze the data obtained from umbrella sampling simulations.

2.3 RESULTS AND DISCUSSIONS

Formation of the BNNT-Salt-Water Hybrid

The BNNT-LiTFSI-water hybrid is formed by soaking a 10-nm long and 1-nm diameter open-ended (7, 7) BNNT in a 10 m aqueous electrolyte solution of LiTFSI. Under such conditions, the BNNT is spontaneously filled by the salt solution resulting in the BNNT-salt-water hybrid. The final equilibrium state of this hybrid is shown in Figure 2.1(a). The non-bonded interaction parameters used in the current study can be found in Table A1 in appendix A. These forcefield parameters have been previously used to study the structural properties of highly concentrated aqueous LiTFSI electrolytes.[96,97,98] Please see the Methods section for a more detailed discussion on the molecular dynamics or MD simulation set-up used to study this filling process. The BNNT-LiTFSI-water hybrid is an endohedral, non-covalent nanotube hybrid. It is characterized by the presence of the periodic, axial, and non-overlapping molecular ordering of single TFSI anions and lithium-ion-solvating water blocks within the BNNT (please see Figure 2.1(b)). Such an ordering is caused by the large size of the TFSI anion[99] that is comparable to the diameter of the BNNT. The bulkiness of the TFSI anion prevents it from occupying the same axial position as water molecules when confined in a nanometer wide (7, 7) BNNT (please see Figure 2.1(c)). We attribute the formation of this nanotube-salt-water hybrid to the strong affinity of TFSI anion to enter the BNNT. The TFSI anion has a higher affinity to enter the empty (7, 7) BNNT before other molecules of the electrolyte solution. The next molecule to enter the BNNT cannot be another TFSI anion due to electrostatic repulsions; as a consequence, lithium-ion-solvating water molecules enter the BNNT following the TFSI anion. This process continues throughout the filling process resulting in this ordered structure. This nanometer wide BNNT, therefore, acts as a

template[62] that hosts the unique ordered structure of TFSI anions and water blocks that would not have been possible in the absence of 1D nanoconfinement. To better understand the affinity of the TFSI anion towards the BNNT, we have tabulated the LJ and electrostatic contributions to the interaction energy (please see table A2 in the appendix A) between the BNNT and the TFSI ions, Li ions, and water molecules confined in it. From table A2, we can see that the adhesion between the BNNT and the TFSI anions is primarily caused by the van der Waals interactions between them. In chapter 3, we provide a more detailed discussion on the effects of salt concentration and nanotube diameter on structure of the salt solution confined inside the tube. Also, we provide free energy calculations to show that the TFSI anion has a higher affinity to enter the empty (7, 7) BNNT before other molecules of the electrolyte solution. In the following sections, we will discuss the structural properties and stability of this nanotube hybrid.

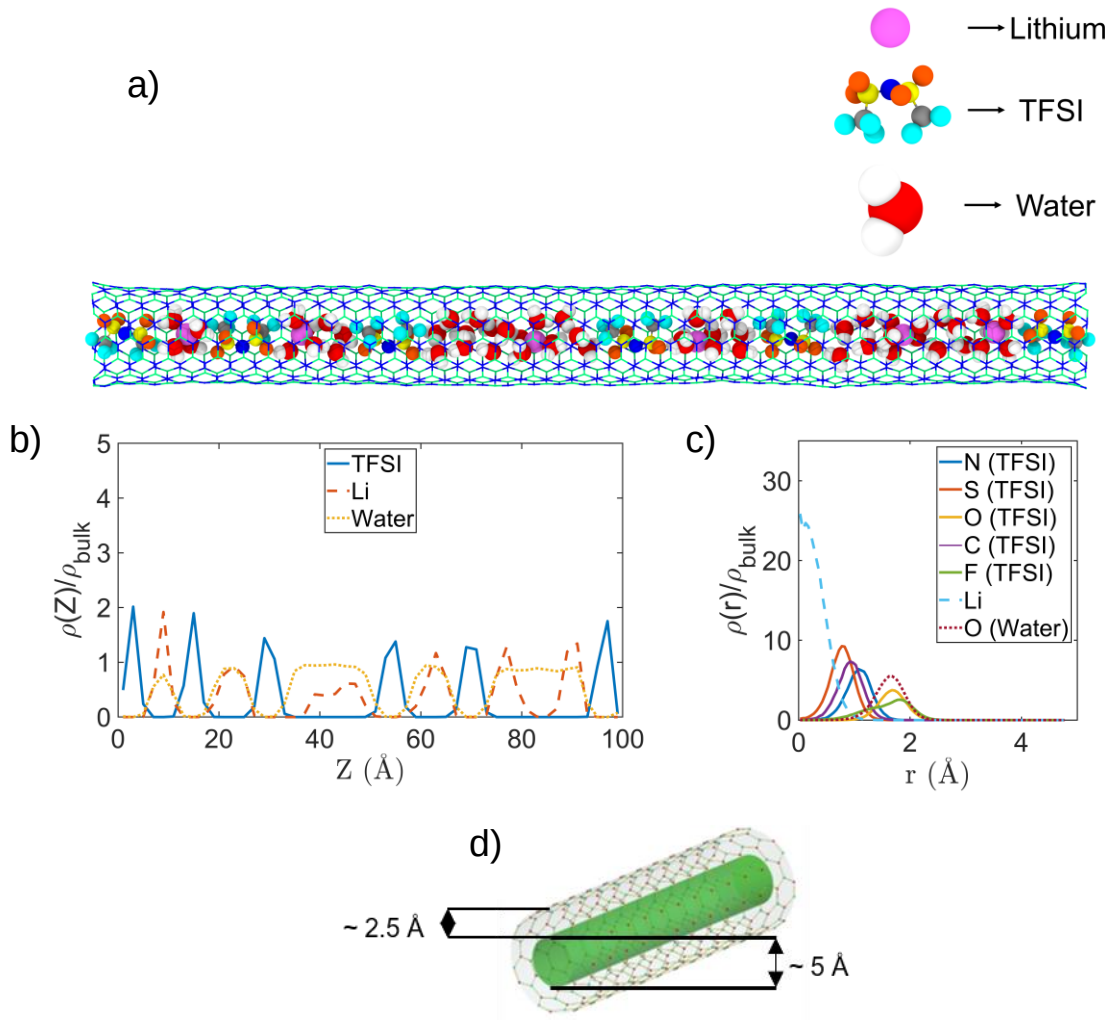

Figure 2.1. a) Simulation snapshot of the BNNT-salt-water hybrid formed through the non-covalent interaction between a 1-nm-diameter (7, 7) BNNT and a 10 m aqueous LiTFSI solution. The atoms surrounding the nanotube hybrid were removed to provide a clearer picture of the BNNT-salt-water hybrid structure. The snapshot is generated using OVITO.[100] b) Axial distribution of the nitrogen atoms (representing the $TFSI^-$ ion), Li^+ ions, and water oxygen atoms (representing the water molecules) confined inside the 1-nm-diameter (7, 7) BNNT. c) Radial distribution of the different atoms of the $TFSI^-$ ion, Li^+ ion, and the water oxygen atom confined inside the 1-nm-diameter (7, 7) BNNT. d) Schematic depicting the confinement-induced localization of all the species below a small (~2.5 Å) radial distance around the BNNT axis.

Structural and Dynamic Properties of the BNNT-Salt-Water Hybrid

Figure 2.2(a) shows the axial root mean square displacement of the nitrogen atoms of all the TFSI anions (there are six in all) confined inside the (7, 7) BNNT. We see that the nanoconfined TFSI anions are localized in the axial direction as confirmed by their very small axial displacement. More importantly, we find that these displacement values remain constant with time confirming negligibly small diffusivity (which is given by the slope of the variation of the mean square displacement with time) of all the TFSI anions within the BNNT and constituting the BNNT-LiTFSI-water hybrid. Two factors contribute to this extreme trapping of the TFSI ions leading to their virtually immobile states. First is their strong attraction to the boron nitride (see Ref. 9 and table A2 in appendix A). The second is the presence of the axial water blocks on either side of the TFSI anions within the nanoconfinement preventing them from any further axial motion. These dual factors ensure this negligibly small (much smaller than that reported by Li *et al.*[19] that probes the trapping of TFSI ions by boron nitride) diffusivity of the TFSI ions.

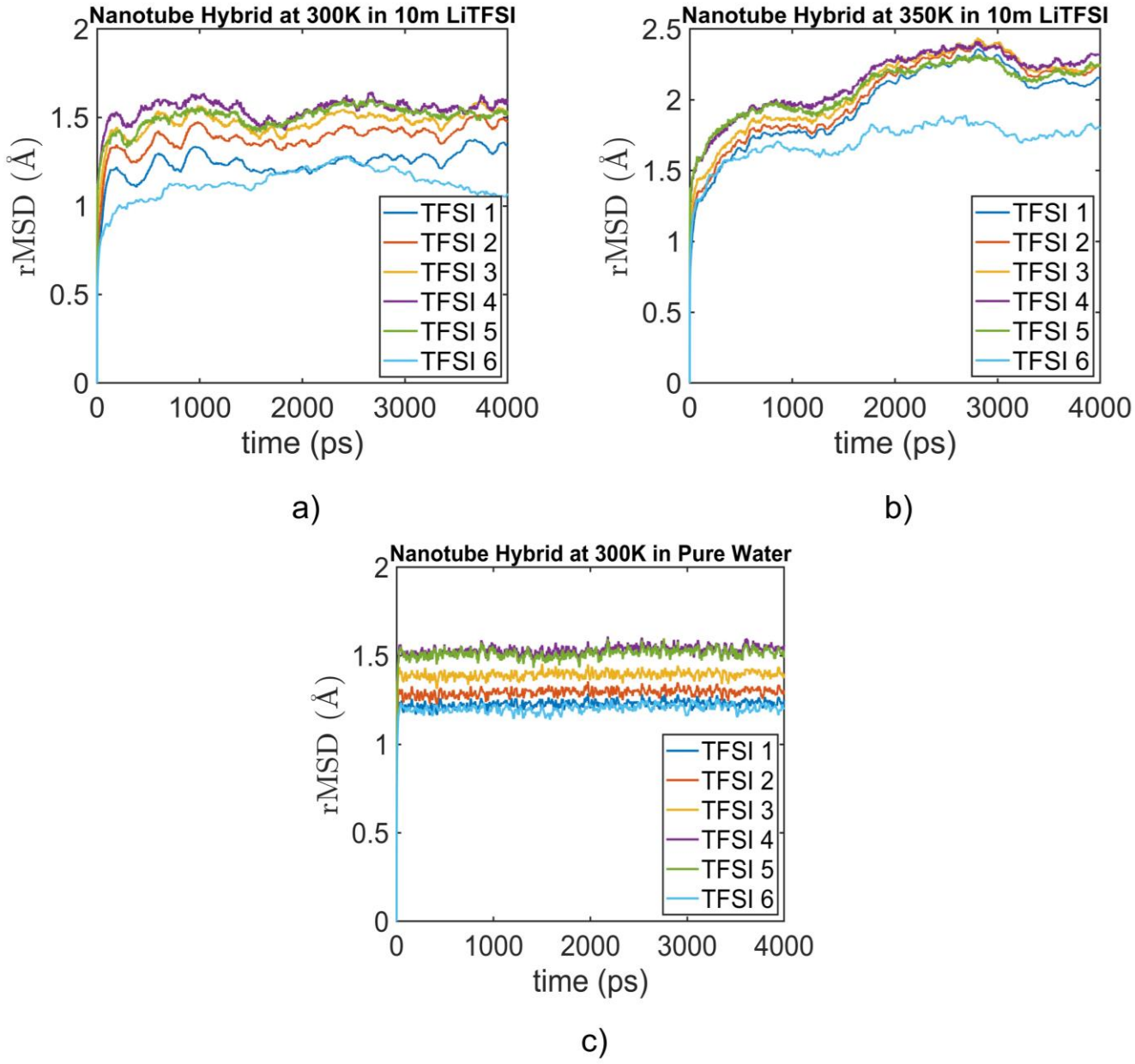

Figure 2.2. Axial root mean square displacement (rMSD) of the nitrogen atoms of all the TFSI anions (six in all) of the BNNT-salt-water hybrid system for the case when the hybrid is surrounded by a) 10m LiTFSI at 300K, b) 10m LiTFSI at 350K, and c) pure water at 300K.

Through our simulations, we observe that these immobilized TFSI anions themselves act as barriers for the individual water blocks that are present in between them resulting in the formation of zero-dimensional (0D) water blocks (as confirmed by Fig. 2.3). In figure 2.3, we provide the axial root Mean Square Displacement (axial-rMSD) of these water blocks/pockets (confined inside the BNNT and constituting the BNNT-LiTFSI-water hybrid). The axial-rMSD of the water saturates to approximately 6 Å. Saturation to such a value indicates that water experiences a strong confinement even in the axial direction, in addition to the radial confinement imposed by the (7, 7) BNNT. *As a result, these water blocks qualify as 0D water pockets due to confinement in all three directions*. In other words, our study confirms that in a set-up (namely, the nanotube that is a 1D nanostructure), which is known to orient the water molecules in 1D chains,[7,51,79-81] we encounter 0D water states. Such 0D water blocks/pockets were previously reported in experimental studies involving nano-confined water in room temperature ionic liquid.[82] One important difference between the current and previously reported water pockets/blocks (Ref. 82) is that confined water, in the present case, solvates the lithium cation in the pockets.

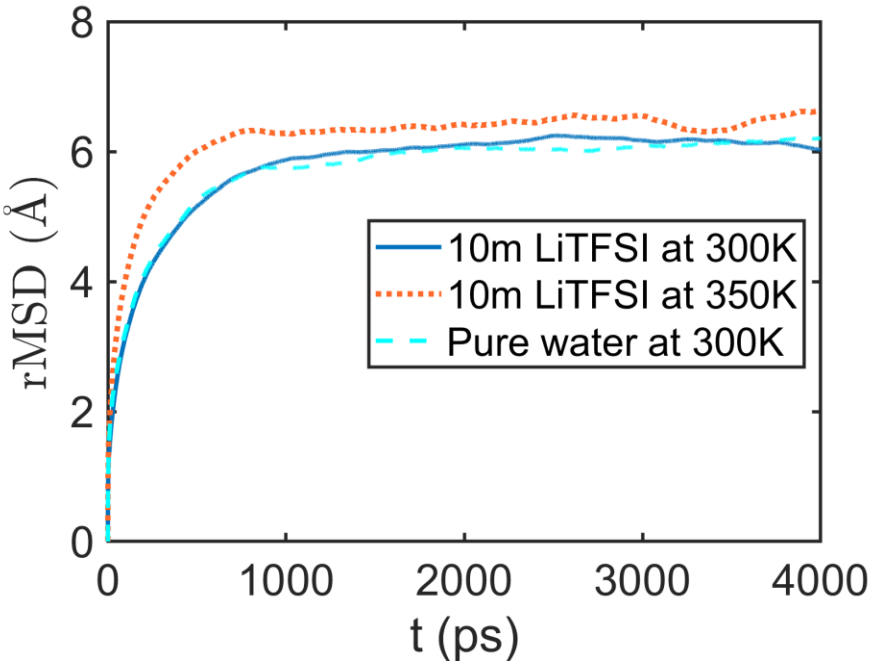

Figure 2.3. Axial root mean square displacement (rMSD) of the oxygen atoms of water molecules confined inside the BNNT-salt-water hybrid. The rMSD is obtained by averaging the MSD values of all the water molecules encapsulated within the BNNT.

Further, we examine the crystalline nature of these 0D water blocks/pockets mentioned above. Figure 2.4 shows the re-orientational correlation function (RCF) of the dipole vectors of these 0D water pockets. The RCF can be expressed as $\langle e_i(t).\, e_i(0)\rangle$, where e_i is the dipole vector of i^{th} water molecule and the bracket represents ensemble average. This RCF function indicates the time-dependent decay of dipole orientational memory of water molecules due to the random rotational motion. For the case of liquid water, this function decays towards zero.[83] On the other hand, in systems where the orientational motion of water is restricted (*e.g.*, ice), water RCF decays towards a non-zero value.[83] From Fig. 2.4, we see that the RCF of water molecules inside the hybrid decays to zero, similar to liquid water. Therefore, these results confirm that the 0D water blocks/packets

exist in a non-crystalline liquid state. Such properties of the 0D water could find applications in nano-heterogeneity engineering for cryo preservation.[82]

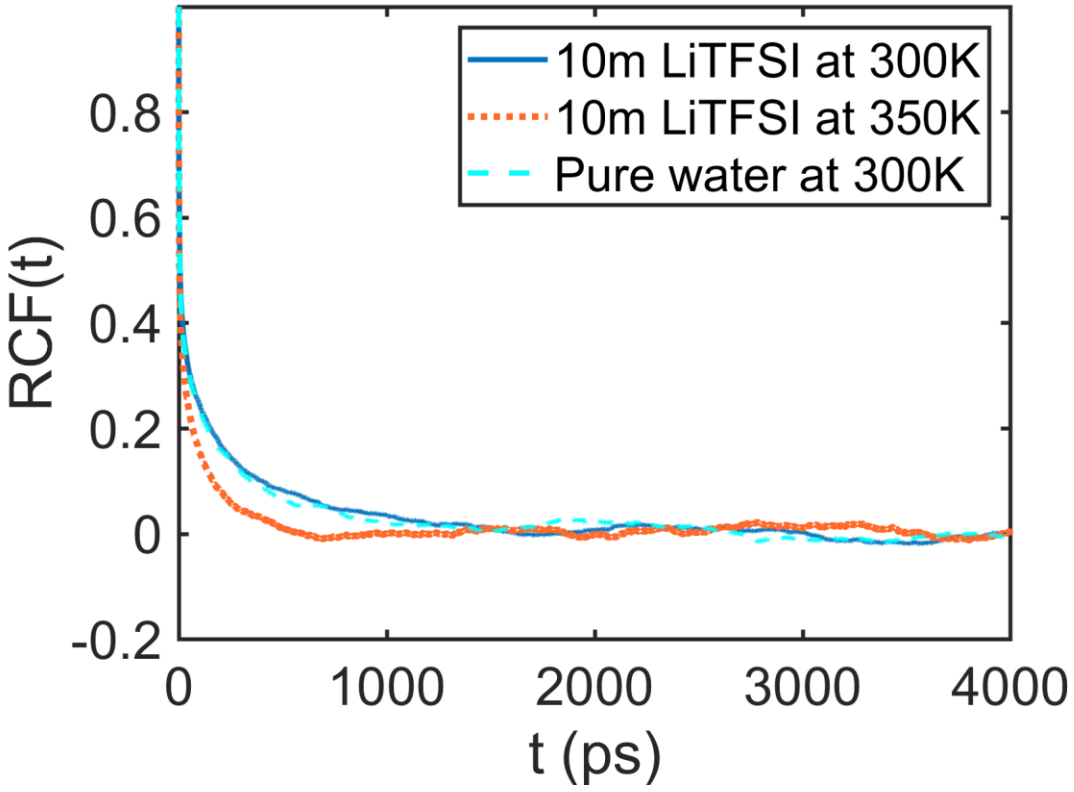

Figure 2.4. Re-orientational correlation function of the dipole vectors of water molecules (confined inside the BNNT and constituting the BNNT-LiTFSI-water hybrid).

Also, we have studied the effect of the BNNT on the ionic charge density distribution in the electrolyte solution surrounding the BNNT (*i.e.*, outside the BNNT). Figure 2.5 shows the ionic charge density, as a function of radial distance from the nanotube axis, for radial distances ranging from r = 5 Å (≈ nanotube radius) and r = 20 Å. For this analysis, we have considered 0.05 Å thick

cylindrical sheaths that are coaxial with the BNNT, and the radius of the cylindrical sheaths range from 5 Å to 20 Å. By computing the ionic charge density in each of these cylindrical sheaths, we have obtained the ionic charge density curve as a function of the radial distance from the nanotube axis. From figure 2.5, we observe a negative charge density peak at the BNNT-electrolyte interface which is accompanied by damped oscillations in ionic charge density that persist beyond a distance of 10 Å from the BNNT surface. This oscillatory behavior is a result of strong correlation between ions in a highly concentrated electrolyte[101-104] and the affinity of $TFSI^-$ ions towards BNNT surface (which is primarily caused by the van der Waals interaction between the BNNT walls and the $TFSI^-$ ions) (please see Table A2 in appendix A).

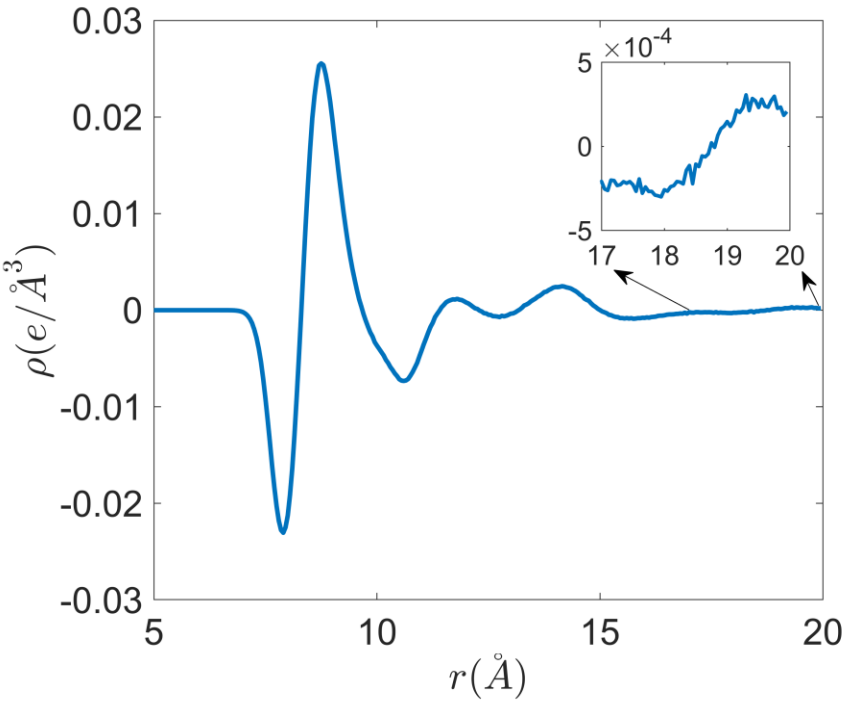

Figure 2.5. Ionic charge density, in the electrolyte solution surrounding the BNNT, as a function of radial distance from the axis of the BNNT. The ionic charge density variation for larger *r* has been magnified in the inset of the figure.

Stability of the BNNT-Salt-Water Hybrid

We have performed simulations (on the mobility of the TFSI anions and 0D state and crystallinity of the water pockets/blocks constituting the BNNT-LiTFSI-water hybrid) to check if the hybrid would be stable at temperatures significantly elevated (*i.e.*, at 350K) from the room temperature and in a pure water environment (*i.e.*, where all the salt from the surrounding outside the nanotube hybrid has been removed). Fig. 2.2(b) confirms that even at an elevated temperature of 350K, the rMSD of all the six TFSI ions confined within the BNNT are not significantly affected in comparison to those at room temperature [see Fig. 2.2(a)]. For the case of salt-depleted pure water surroundings, we find that the rMSD and the diffusivity of the TFSI ions [see Fig. 2.2(c)] are similar in magnitude to that of the case where the nanotube hybrid is surrounded by 10 m aqueous LiTFSI [see Fig. 2.2(a)]. These results indicate that the TFSI anions that form the nanotube-salt-water hybrid are immobilized inside the hybrid both at an elevated temperature and a pure water environment (surrounding the BNNT). Under such circumstances, we expect the water pockets/blocks, trapped axially between the between the TFSI anions, to continue to behave as a 0D system even in presence of elevated temperature or salt-free surroundings. Figure 2.3 compares the axial-rMSD of confined water for all the three cases described above. For all the three cases, the axial-rMSD of water saturates to a value around 6 Å, with the elevated temperature case showing a slightly larger saturation value. These results agree with our hypothesis that the immobilized TFSI anions impose an axial confinement on the water present inside the nanotube hybrid resulting in 0D water pockets for a variety of conditions (*e.g.*, the condition of significantly elevated temperature as well as the condition where the solution surrounding the hybrid has no salt). Finally, figure 2.4 compares the RCF of the dipole vectors of the 0D water for all the three cases: for each of the case, the RCF decays to zero indicating that water exists in a liquid phase

inside the 0D water pockets. These results confirm the stability of the BNNT-salt-water hybrid against an elevated temperature (350K) as well as a drastic change in the composition of the surrounding medium (i.e., when all the salt from the surrounding medium has been removed).

Finally, in Figure 2.6, we show the free energy curves as a function of the axial positions of centers of mass of the LiTFSI pairs at both ends of the BNNT-salt-water hybrid surrounded by a pure water environment. In Fig. A1 in appendix A, we schematically describe the procedure adopted to obtain these free energy curves. At both the ends of the nanotube hybrid, we see a free energy barrier of approximately 7 kcal/mol against the diffusion of LiTFSI, at those ends, into pure water. We attribute this diffusive tendency (or the lack of it) to the strong interaction between the TFSI anion and the BNNT, which is primarily caused by the van der Waals interactions between them (please see table A2 in the appendix A). These results further confirm the super stability of the endohedral nanotube-salt-water hybrid formed due to the non-covalent interactions between the LiTFSI aqueous solution and the (7, 7) BNNT. The non-diffusive nature of the TFSI anions at both the ends of the nanotube hybrid ensures that the adjacent 0D water does not leak out of the hybrid and these end-TFSI anions act as a seal that holds the BNNT-LiTFSI-water hybrid together.

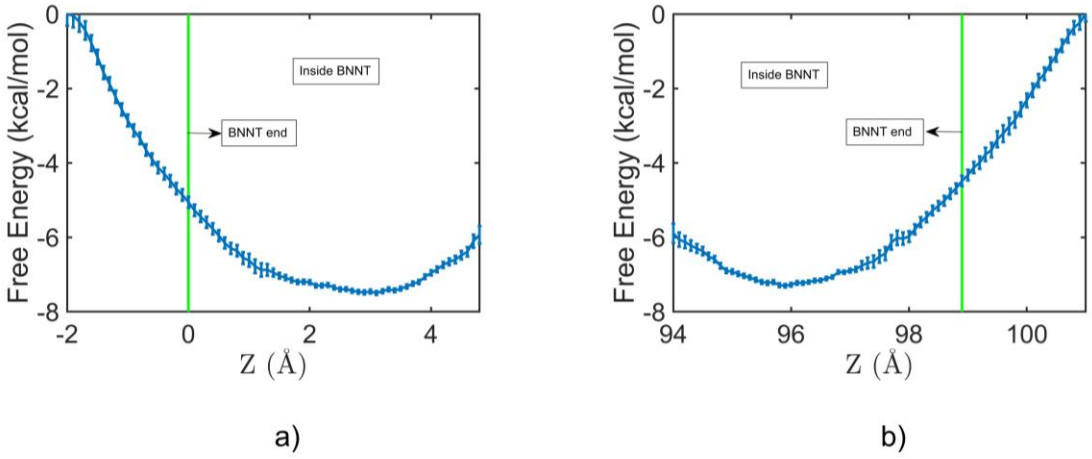

Figure 2.6. Free energy curves as a function of the axial position of the center of mass of the LiTFSI pair at a) the lower end (near z = 0 Å) and b) the upper end (near z = 100 Å) of the BNNT-salt-water hybrid surrounded by pure water at 300K.

2.4 CONCLUSIONS

The findings presented in this paper point to the simulation-motivated discovery of a new type of nanotube-based hybrid: the hybrid is a BNNT-salt-water hybrid, where the TFSI anions and Li-ion-solvating water molecules get encapsulated as periodic axially non-overlapping blocks in a BNNT that has similar internal diameter as the size of the TFSI anion. The hybrid is characterized by the ultimate immobility of the TFSI anions. The more interesting facet is the zero-dimensional (0D) and liquid state of the entrapped water constituting the hybrid. Equally interestingly, here we encounter 0D water in a nanostructure (namely nanotube) known to orient water molecules into 1D chains. Finally, the extreme stability of the BNNT-salt-water hybrid, as established from the free energy analysis as well as the response of this hybrid to different "perturbations" (*e.g.*, increase in temperature or changing the chemical composition of the surroundings), ensures the possibility of utilizing these hybrids in settings that are vastly different from the conditions that led to their formation. In summary, we can identify a combination of two critical factors driving the formation

of such unique nanotube-salt-water hybrid system: (1) the presence of an anion that is strongly attracted to the chosen nanotube and (2) the diameter of the nanotube being comparable to the dimensions of the anion. We anticipate that the present study will open up an entirely new area of study focused on designing and fabricating such nanotube-salt-water hybrids and towards utilizing such hybrids for multi-faceted applications.

The contents of this chapter have been published as Chava, B. S., Wang, Y., Sivasankar, V. S., & Das, S. (2020). Water-free Localization of Anion at Anode for Small-Concentration Water-in-Salt Electrolytes Confined in Boron-Nitride Nanotube. Cell Reports Physical Science, 1(11), 100246.

Chapter 3: Water-free Localization of Anion at Anode for Small Concentration Water-in-Salt Electrolytes Confined in Boron-Nitride Nanotube*

Abstract

Water-in-salt electrolyte (WISE) systems have been recently identified to significantly enhance the performance of aqueous Li-ion batteries owing to the formation of solid electrolyte interphase (SEI) due to localization of the cation-anion pair near the negative electrode in the absence of free water. Such localization occurs for an extremely large concentration of the electrolyte salt that enhances the interionic attraction between the salt cation and anion, thereby ensuring that the cation "carries" the anion with itself to the anode. Here we employ atomistic simulations to establish that for a LiTFSI electrolyte solution (LiTFSI is a salt that is well-known to form WISE systems) confined in a 1-nm-diamter boron nitride nanotube (BNNT), such water-free $TFSI^-$ anion localization at the anode surface is possible at a LiTFSI concentration that is several times smaller than that needed for such localization in a non-nanoconfined LiTFSI WISE system.

3.1 INTRODUCTION

Water-in-salt electrolyte (WISE) systems are characterized by the presence of an extremely large concentration of a salt (typically consisting of a small cation and a large anion) in an aqueous medium: the salt concentration is so large that the salt outnumbers water by both weight and volume and the anion replaces some water molecules in the hydration shell of the cation.[17] Typical examples of such WISE systems include large concentrations of salts like LiTFSI[17], LiOTf[105], LiBETI[106], NaOTf[107], LiFSI[108], NaFSI[109] $NaClO_4$[110], $LiNO_3$[111], $NaNO_3$[112], NaOAc[113], KOAc[114]

and $ZnCl_2$[115] dissolved in water. For the LiTFSI salt, for example, the "water-in-salt" characteristic (i.e., the scenario when the salt outnumbers water by both weight and volume) is witnessed for a salt concentration of 5 molal (m) and above.[17] Despite the long history of research on "solvent in salt" type systems,[116-121] it is only recently that WISE has been discovered to enhance the electrochemical performance of aqueous Li-ion[17,105,106,121] and Na-ion[107,109,110,112,113] batteries. For example, Suo *et al.*[17] showed a significant increase in the size of the electrochemical stability window (the stability window attained a value of 2.3 V) of the Li-ion batteries when LiTFSI WISE systems is used with 21 m concentration of LiTFSI salt. For such a large concentration of the LiTFSI salt, the $TFSI^-$ ions are able to replace some of the water molecules from the solvation shell of the Li^+ cation. As a result, there is a significant enhancement in the interionic attraction between the Li^+ and $TFSI^-$ ions, which allows some of the $TFSI^-$ ions to be "carried" by the Li^+ ion. Therefore, when a voltage difference is applied across the LiTFSI WISE system, the attraction of the Li^+ ion towards the negative electrode (anode) invariably draws some of the $TFSI^-$ ions (that are strongly attracted to the Li^+ ion) towards the anode. Hence such a highly concentrated WISE system creates a most remarkable scenario where the Li^+-$TFSI^-$ ion-pair remains in close proximity of the anode with very little probability of having any free water present in the same region. Such a scenario implies that the $TFSI^-$ ions can get reduced at the anode prior to the water getting reduced, which in turn helps to form a robust water-free SEI (solid electrolyte interphase) layer. In addition, the lack of free water near the negative electrode prevents hydrogen evolution.[17] These two factors help to extend the electrochemical stability window of the aqueous WISE. These effects are in direct contrast to what happens for the case of a standard electrolyte solution of 1m LiTFSI salt in the presence of an applied electrostatic potential difference: the weaker concentration of the LiTFSI salt implies a much weaker interionic coupling between the Li^+ and

$TFSI^-$ ions and accordingly, in the presence of an applied electrostatic potential difference, the Li^+ ions are driven closer to the anode, while the $TFSI^-$ ions are driven away from the anode. This justifies why the WISE systems are being extensively researched for battery applications.

Despite the benefits of utilizing the WISE systems for battery applications, the unavoidable use of large salt concentration (e.g., 21 m for LiTFSI-salt-based Li-ion batteries) makes the system extremely expensive (associated with the cost of using such large amounts of salt), which is one of the biggest bottlenecks for commercialization of such WISE-system-based Li-ion or Na-ion batteries.[110,112,113,114,122] Under such circumstances, researchers have used cheaper salts like $NaClO_4$[110] which, however, do not form a favorable fluorine based SEI resulting in poor cycling stability.[123,124,125] Other strategies such as coating the anode with highly fluorinated ether (HFE)[126] and using new electrolytes like hybrid aqueous/non-aqueous electrolyte (HANE),[127] hydrate melt electrolytes,[106] and inert-cation-assisted WISE[123] were developed by researchers to enhance the electrochemical stability window of aqueous electrolytes. However, the challenge to ensure localization of the large anions (e.g., the $TFSI^-$ ions for the LiTFSI WISE system) at the anode at a relatively smaller salt concentration remains unaddressed.

In this paper, we employ Molecular Dynamics (MD) simulations to establish the most remarkable possibility of such localization of the $TFSI^-$ ion near the anode for a LiTFSI WISE system at a significantly smaller salt concentration (as compared to 21 m) by nanoconfining the LiTFSI WISE in Boron Nitride nanotubes (BNNTs). BNNTs are chosen over other nanotubes (like carbon nanotubes) due to their excellent electrical insulation properties,[16,128] which could prevent the reduction of water confined in them. Besides, we find that the $TFSI^-$ ion shows a great affinity to enter the BNNT prior to any other molecule of the electrolyte. We investigate the structures of 5 m and 10 m LiTFSI WISE confined in BNNTs having diameters of 1.0 nm ((7, 7 BNNT)) and 1.4

nm ((10, 10) BNNT)[16,129]. We discover that for the LiTFSI WISE confined inside a 1-nm-diameter BNNT, the water molecules and the $TFSI^-$ ions prefer to form a strongly ordered structure, characterized by axially non-overlapping and repeating concentration peaks of $TFSI^-$ ion and the water molecules (please see Figure 3.1). This is possible due to the fact that the size of the $TFSI^-$ ion is very similar to the diameter of the 1-nm BNNT. We explain that such a scenario, combined with the greater affinity of $TFSI^-$ ion to enter the BNNT, leads to a water-free $TFSI^-$ peak near the negative electrode. More importantly, we find that this affinity of $TFSI^-$ ion to enter the BNNT (we consider a negative graphite surface at one end of the BNNT with the other end of the BNNT open to bulk electrolyte) is not nullified in the presence of a voltage difference (of strength as large as 5 V) applied across the LiTFSI WISE system with a large negative voltage (-2.5V) being applied to the graphite surface at the end of the BNNT. Under such circumstances, if a pre-lithiated anode[130-134] is used, one would have the $TFSI^-$ ions, and not the water molecules, get reduced at the anode resulting in the formation of SEI. Suo *et al.*[17] proposed such localization of the Li^+-$TFSI^-$ ion pair near the anode for a non-nanoconfined LiTFSI WISE system using an extremely large (21 m) salt concentration that enforced an augmented interionic attraction between the Li^+ and $TFSI^-$ ions, as discussed above. Our findings, on the other hand, establish that the interplay of confinement effect, with the confinement being strong enough so that it can induce the ordering of the $TFSI^-$ ions and water molecules, and the greater affinity of the $TFSI^-$ ion to enter the empty BNNT prior to other electrolyte molecules and ions, allows such water-free localization of the $TFSI^-$ ion and hence the formation of a stable SEI in the presence of a pre-lithiated negative electrode. Our MD simulations also reveal that the LiTFSI WISE confined in a relatively weaker nanoconfined system (BNNT of 1.4 nm diameter) does not have such a strong ordering effect in the axial distribution of the $TFSI^-$ ion and the water molecules. As a consequence, such water-free

localization (and hence the formation of the stable, water-free SEI) of the $TFSI^-$ ion near the anode surface is no longer possible for the case of LiTFSI enclosed in the BNNT of 1.4 nm diameter. We explain that such a strong dependence on the diameter of the BNNT stems from the fact that for the 1-nm-diameter BNNT, the size of the $TFSI^-$ ion becomes closely comparable to the size of the nanoconfinement, which restricts the degrees of freedom of the $TFSI^-$ ions enforcing this distinct ordering effect (between the $TFSI^-$ ion and the water molecules) that can be observed even in the presence of a large electric potential difference across the system. However, for the 1.4-nm-diameter BNNT, the degrees of freedom of $TFSI^-$ ions are not hindered with such severity, thereby disturbing this large ordering effect. Our simulations also reveal the effect of system parameters, e.g., the concentration of the LiTFSI salt on such anion localization at the anode surface inside the 1-nm-diameter BNNT. Finally, we further test our hypothesis of the nanoconfinement-driven water-free localization of the anion at the negative electrode for the aqueous solution of another salt, namely LiBETI, known to form WISE systems. We indeed find that the large size of the $BETI^-$ ion, coupled with the greater affinity of $BETI^-$ ion (as compared to the other existing species) to enter the BNNT, ensures a water-free localization of the $BETI^-$ ion at the anode surface in a 1-nm diameter BNNT.

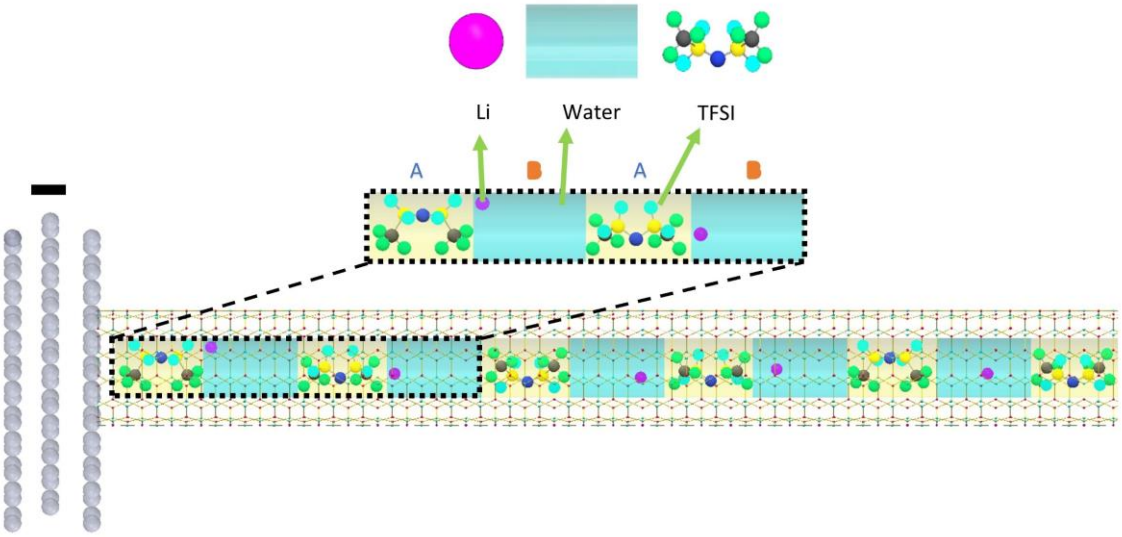

Figure 3.1. Schematic of the confinement induced molecular ordering of the $TFSI^-$ ions and the water molecules. Such an ordering refers to the presence of the non-overlapping blocks of A and B. Here Block A: $TFSI^-$ ion without any water and Block B: water molecules with a possible presence of a Li^+ ion (in other words, block B represents the Li^+ ion with its hydration shell). Here the confinement is a 1-nm-diameter BNNT that has negatively charged graphite electrode at one end while the other end is open to bulk electrolyte. The molecular ordering between the $TFSI^-$ ions and the water molecules, combined with the affinity of $TFSI^-$ ion to enter the BNNT prior to other molecules and ions (see Fig. B2 in the appendix B), helps to ensure the water-free localization of the $TFSI^-$ ions near the graphite negative electrode at the closed end of the BNNT. Therefore, in presence of negative voltage at the graphite surface where the $TFSI^-$ ion has localized, we can obtain a water-free $TFSI^-$ ion localization. In this figure, pink particle: lithium ion; blue rectangle: water medium; green particles: fluorine atoms of the $TFSI^-$ ion; grey particles: carbon atoms of the $TFSI^-$ ion; yellow particles: sulfur atoms in the $TFSI^-$ ion; cyan particles: oxygen atoms of the $TFSI^-$ ion; dark blue particles: nitrogen atoms in the $TFSI^-$ ion.

3.2 RESULTS

Axial Distribution of the Ions and Water Molecules in the Absence of any External Voltage Difference

We first probe the structure of the LiTFSI WISE at relatively low salt concentrations (5 m and 10 m) nanoconfined in BNNTs of diameters 1 nm (see Figure 3.2) and 1.4nm (see Figure 3.3). As shown in Figures 3.2A, D, 3.3A, D as well as Figure B1(a) in the appendix B, initially empty BNNTs were soaked in aqueous LiTFSI solutions and were filled with electrolyte molecules. Figures 3.2B, E and 3.3B, E show the distribution of the nitrogen atoms (representing the $TFSI^-$ ion), Li^+ ion, and the water oxygen atoms (representing the water molecules) along the axis of the BNNT. The tube length is divided in bins of width 2 Å and the number density of atoms in each bin is averaged over the entire production run. The atom number densities are normalized by their respective values in bulk solution. Figures 3.2B and 3.2E show the axial distribution of these ions and atoms confined in a 1-nm-diamter BNNT for 10 m and 5 m LiTFSI WISE, respectively. In both Figures 3.2B and 3.2E, we observe highly ordered, non-overlapping, and noticeable peaks of the nitrogen atoms (representing the $TFSI^-$ ion) and oxygen atoms (of the water molecules). This ordered distribution forms repeating alternate "blocks" of $TFSI^-$ ions and water molecules surrounding Li^+ ions, that continues along the entire nanotube axis, as evident from the corresponding snapshots (see Figures 3.2C and 3.2F). Here, we define a block as the region inside the 1-nm-diameter BNNT where the axial density of $TFSI^-$ ion (water molecules) is non-zero while the axial density of water molecules ($TFSI^-$ ion) is zero. Thus, we can clearly differentiate between the $TFSI^-$ blocks and water blocks inside the 1-nm-diameter BNNT based on the axial distribution profiles (more discussions on the properties of such "blocks" are provided in Note B1 and Table B1 in appendix B). This ordering is representative of the fact that the large degree of

nanoconfinement, which stems from the nanotube dimension being closely comparable to the size of the $TFSI^-$ ions, ensures that the water molecules and the $TFSI^-$ ion are forced to occupy different adjacent axial but similar radial locations (discussed in greater details in Figure 3.4). The peaks corresponding to the Li^+ ion distribution, and the peaks associated with the distribution of the water molecules overlap extensively, confirming that the Li^+ ions are solvated in water.

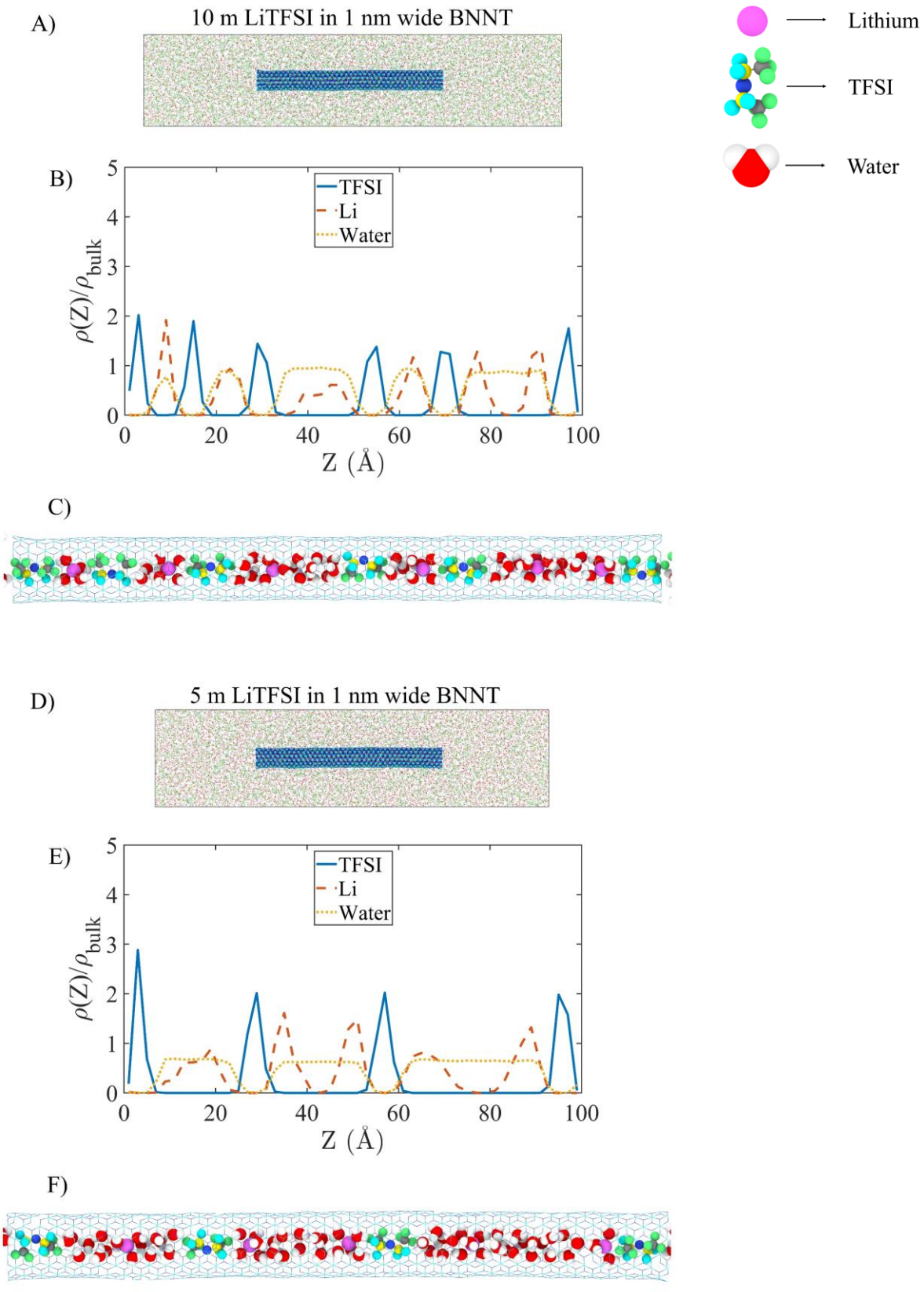
A)
10 m LiTFSI in 1 nm wide BNNT
Lithium
TFSI
Water
B)
TFSI
Li
Water
$\rho(Z)/\rho_{bulk}$
Z (Å)
C)
D)
5 m LiTFSI in 1 nm wide BNNT
E)
TFSI
Li
Water
$\rho(Z)/\rho_{bulk}$
Z (Å)
F)

Figure 3.2. MD simulation snapshots showing the entire system for the case of (A) 10 m LiTFSI WISE confined in 1-nm-diameter BNNT and (D) 5 m LiTFSI WISE confined in 1-nm-diameter BNNT. Axial distribution of the nitrogen atoms (representing the $TFSI^-$ ion), Li^+ ions, and water oxygen atoms (representing the water molecules) for the cases of (B) 10 m LiTFSI WISE confined in 1-nm-diameter BNNT (also reported in chapter 2) and (E) 5 m LiTFSI WISE confined in 1-nm-diameter BNNT. MD simulation snapshots showcasing the distribution of the different species including the local arrangement of salt ions and water molecules for the case of (C) 10 m LiTFSI WISE confined in 1-nm-diameter BNNT and (F) 5 m LiTFSI WISE confined in 1-nm-diameter BNNT. In (C) and (F), atoms surrounding the BNNT were removed, to provide a clearer picture of electrolyte distribution inside the BNNT. All the simulation snapshots are generated using OVITO[100].

Also, in both the simulations (with 1-nm-diameter BNNT soaked in 5 m and 10 m aqueous LiTFSI), $TFSI^-$ ion entered the BNNT first followed by water molecules and Li^+ ion as can be seen from Figures B2(a,b) (please see appendix B), which shows the filling process of 5 m and 10 m LiTFSI inside the 1-nm-diameter BNNT. This affinity of $TFSI^-$ ion to enter the initially empty BNNT prior to other electrolyte molecules will be discussed in detail in the following sections. Such a situation will imply that, when one end of the 1-nm-diameter BNNT is placed near an electrode (the set-up that will be tested for the case of the LiTFSI confined in 1-nm-diameter BNNT in presence of charged electrodes, see Figure 3.6) with the other end open to electrolyte, we might be able to leverage the size effect associated with the 1-nm-diameter BNNT to simultaneously drive the $TFSI^-$ ions towards and the water molecules away from the vicinity of this particular electrode resulting in a water-free $TFSI^-$ ion localization. A critical test would be to see if such a scenario could persist even in the presence of an electrode, with negative potential, near the BNNT end. We will analyze this exact setup in the following sections. If this scenario persists (as will be established later), *it will be possible to ensure the water-free localization of $TFSI^-$ ions at the negative electrode at a salt concentration that is significantly smaller as compared to that needed for localizing $TFSI^-$ ions at the anode in absence of any confinement.*

Figures 3.3B and 3.3E respectively show the axial distribution of the nitrogen atoms (representing the $TFSI^-$ ion), Li^+ ion, and water oxygen atoms (representing the water molecules) for 5 m and 10 m LiTFSI WISE confined in 1.4-nm-diameter BNNT. In this case, the lowering of the confinement effect (given that the BNNT diameter increases from 1 nm to 1.4 nm) weakens the extent of non-overlapping ordering of the $TFSI^-$ ions and the water molecules since the size of the $TFSI^-$ ions is no longer closely comparable to the diameter of the BNNT. Accordingly, we obtain only weakly pronounced peaks for both the nitrogen atoms (representing the $TFSI^-$ ion) and the water oxygen atoms and there is a significant overlap between these nitrogen atom and oxygen water atom peaks. In other words, we see a non-zero water density as well as a non-zero $TFSI^-$ ion density at nearly every axial position along the 1.4-nm-diameter BNNT. Thus, based on our definition of "block" that we previously mentioned, we do not see axially separated blocks of $TFSI^-$ ion and water molecules. This confirms that due to the weakening of the confinement effect, inside the BNNT with 1.4 nm diameter, the $TFSI^-$ ion will fail to restrict the water molecules from reaching the electrode, if placed at one end of the BNNT with the other end of the BNNT remaining open to bulk electrolyte.

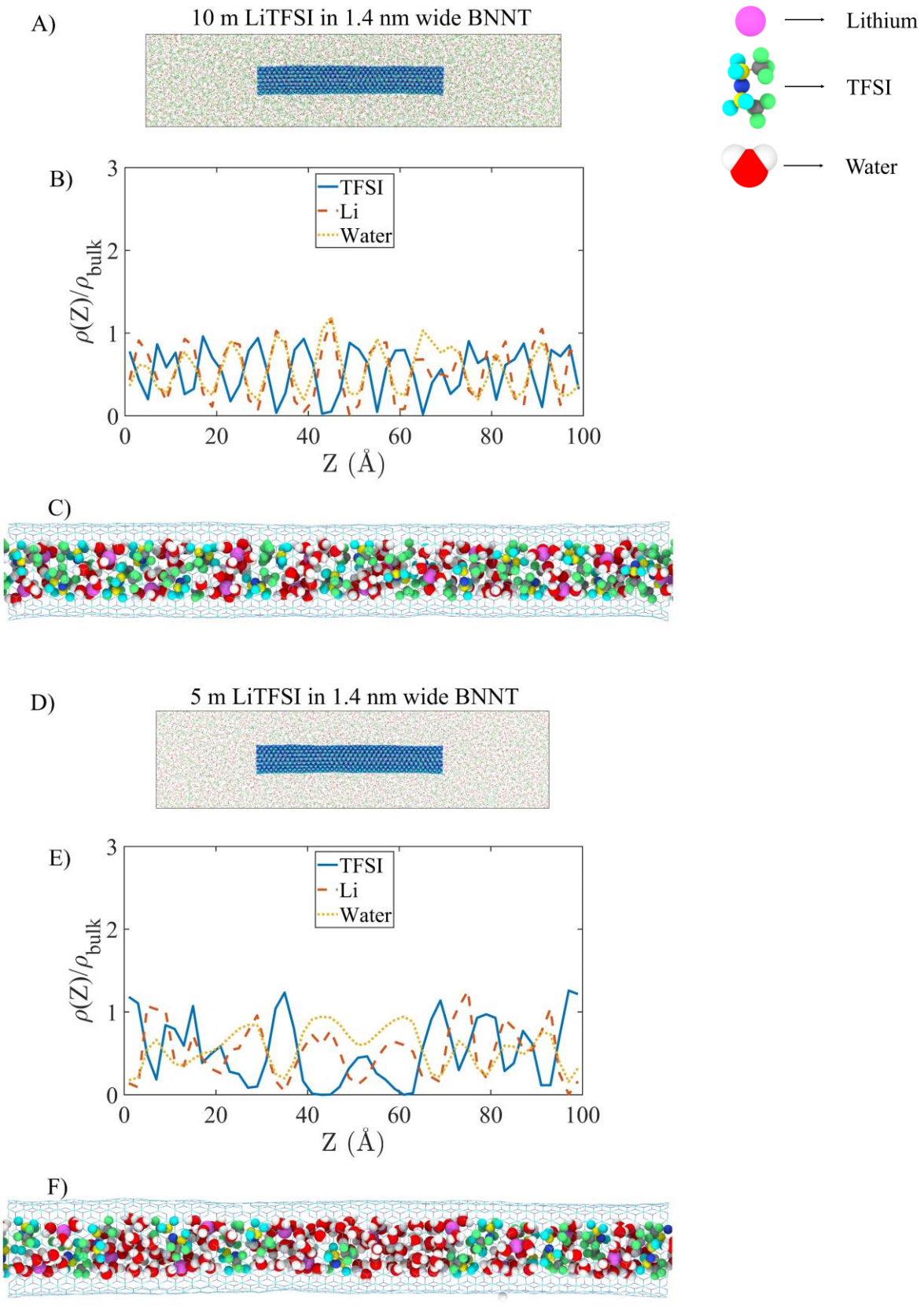
A)
10 m LiTFSI in 1.4 nm wide BNNT
Lithium
TFSI
Water
B)
TFSI
Li
Water
$\rho(Z)/\rho_{bulk}$
Z (Å)
C)
D)
5 m LiTFSI in 1.4 nm wide BNNT
E)
TFSI
Li
Water
$\rho(Z)/\rho_{bulk}$
Z (Å)
F)

Figure 3.3. MD simulation snapshots showing the entire system for the case of (A) 10 m LiTFSI WISE confined in 1.4-nm-diameter BNNT and (D) 5 m LiTFSI WISE confined in 1.4 nm diameter BNNT. Axial distribution of the nitrogen atoms (representing the $TFSI^-$ ion), Li^+ ions, and water oxygen atoms (representing the water molecules) for the cases of (B) 10 m LiTFSI WISE confined in 1.4-nm-diameter BNNT and (E) 5 m LiTFSI WISE confined in 1.4-nm-diameter BNNT. MD simulation snapshots showcasing the distribution of the different species including the local arrangement of salt ions and water molecules for the case of (C) 10 m LiTFSI WISE confined in 1.4-nm-diameter BNNT and (F) 5 m LiTFSI WISE confined in 1.4-nm-diameter BNNT. In (C) and (F), atoms surrounding the BNNT were removed, to provide a clearer picture of electrolyte distribution inside the BNNT. All the simulation snapshots are generated using OVITO[100].

Radial Distribution of the Ions and Water Molecules in the Absence of any External Voltage Difference

Figures 3.4 and 3.5 respectively provide the radial distributions of the different atoms of the $TFSI^-$ ion, Li^+ ion, and the oxygen atom of the water molecule for 5m and 10m LiTFSI WISE confined in 1-nm and 1.4-nm diameter BNNTs. For each case, the nanotube radius was divided in bins of width 0.05 Å and the normalized number density of every species present in each bin was calculated by averaging over the entire production run. Figures 3.4A and 3.4B respectively provide the radial distribution of the different species for 10 m and 5 m LiTFSI WISE confined in 1-nm-diameter BNNT. These radial distribution profiles help to explain the occurrence of the non-overlapping, periodic ordering in the axial distribution of the $TFSI^-$ ions and water molecules. These profiles show that all the atoms are present near the axis of the BNNT and there is a very little probability of finding any atom or ion at a radial location beyond 2.5 Å away from the axis of the BNNT (this is depicted schematically in Figure 3.4C). This is due to the interaction of the BNNT atoms with the different atoms and ions of the LiTFSI WISE system under the condition that the distance between them (i.e., the BNNT atom and an atom/ion of the LiTFSI WISE system)

cannot be smaller than the sum of their van der Waals radii (which is approximately in the range of 2.5 Å < σ_{ij} < 3.5 Å). Such a confinement effect, coupled with the large size of the $TFSI^-$ ion[99] (closely comparable to the diameter of the 1-nm-diameter BNNT) implies that a $TFSI^-$ ion and a water molecule can never occupy the same axial position and are forced to occupy a similar radial location (near the axis of the 1-nm-diameter BNNT) [see Figure 3.4D]. This is also confirmed by the combination of the axial (see Figure 3.2) and radial (see Figures 3.4A and 3.4B) distributions of the $TFSI^-$ ion and water molecules and explains the occurrence of the non-overlapping axial distribution peaks of the nitrogen atoms (representing the $TFSI^-$ ions) and the water oxygen atoms.

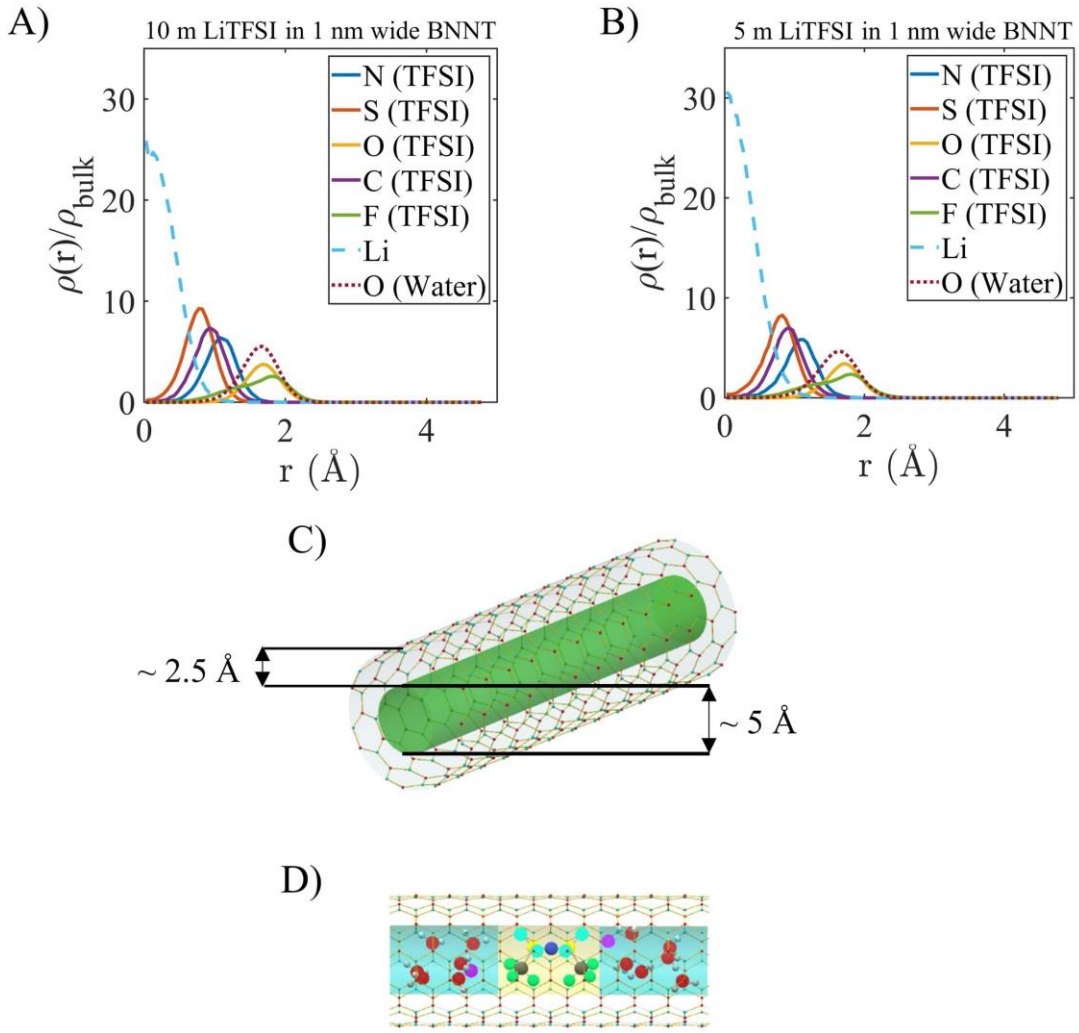

Figure 3.4. Radial distribution of the different atoms of the $TFSI^-$ ion, Li^+ ion, and the water oxygen atom for the cases of (A) 10 m LiTFSI WISE confined in 1-nm-diameter BNNT (also reported in chapter 2) and (B) 5 m LiTFSI WISE confined in 1-nm-diameter BNNT. (C) Schematic depicting the confinement-induced localization of all the species at small (~2.5 Å) radial distances around the BNNT axis (also reported in chapter 2). (D) Schematic depicting the manner in which this localization [identified in (C)] combines with the large size of the $TFSI^-$ ion (the size of the $TFSI^-$ ion is closely comparable to the diameter of the 1-nm-diameter BNNT) to enforce the $TFSI^-$ ion and the water molecules to occupy similar radial (around this BNNT axis) but different axial locations. In figure 4D, pink particle: lithium ion; blue rectangle: water medium; green particles: fluorine atoms of the $TFSI^-$ ion; grey particles: carbon atoms of the $TFSI^-$ ion; yellow particles: sulfur atoms in the $TFSI^-$ ion; cyan particles: oxygen atoms of the $TFSI^-$ ion; dark blue particles: nitrogen atoms in the $TFSI^-$ ion.

On the other hand, for the cases of the 10 m and 5 m WISE confined in the 1.4-nm-diamter BNNT (see Figures 3.5A and 3.5B), the peaks characterizing the radial distribution profiles of the different atoms of the $TFSI^-$ ion, Li^+ ion, and the water oxygen atom are distributed over a much larger range of radial distances owing to a weakening of the confinement effect. For this case too, the atoms and the ions of the LiTFSI WISE system are prevented from coming to a proximity from the BNNT wall that is less than the sum of their van der Waals radii (i.e., the sum of the radii of the BNNT atom and an atom/ion of the LiTFSI WISE system). However, here the diameter of the BNNT being larger (1.4 nm), it allows the atoms and ions of the LiTFSI WISE system to distribute across a much larger radial distance (~4.5 Å) around the BNNT axis (depicted schematically in Figure 3.5C). Within this larger radial space, unlike what happens for the case of 1-nm-diameter BNNT, it becomes possible to accommodate a $TFSI^-$ ion and a water molecule at the same axial location, but different radial location (depicted schematically in Figure 3.5D). This explains the overlap of the axial density profiles of water and $TFSI^-$ ion and why $TFSI^-$ ion will be unable to block water from reaching the electrode surface placed at one end of the 1.4-nm-diameter BNNT with the other end of the BNNT remaining open to bulk electrolyte. Under such circumstances, there appear two separate peaks in the radial distribution of the water oxygen atoms. The first peak near the BNNT axis (i.e., at a smaller *r* value) corresponds to the water (which is hydrating the Li^+ ion) that is not present at the same axial position as $TFSI^-$; on the other hand, the second water peak, far away from the BNNT axis, corresponds to the water that shares the same axial position with $TFSI^-$ ion. In the 1.4-nm-diameter BNNT, unlike in the 1-nm-diameter BNNT, the weakening of the confinement effect ensures that the longest dimension of $TFSI^-$ ions is not aligned parallel

to the BNNT axis resulting in the appearance of multiple peaks in the radial distribution of the different atoms of the $TFSI^-$ ion.

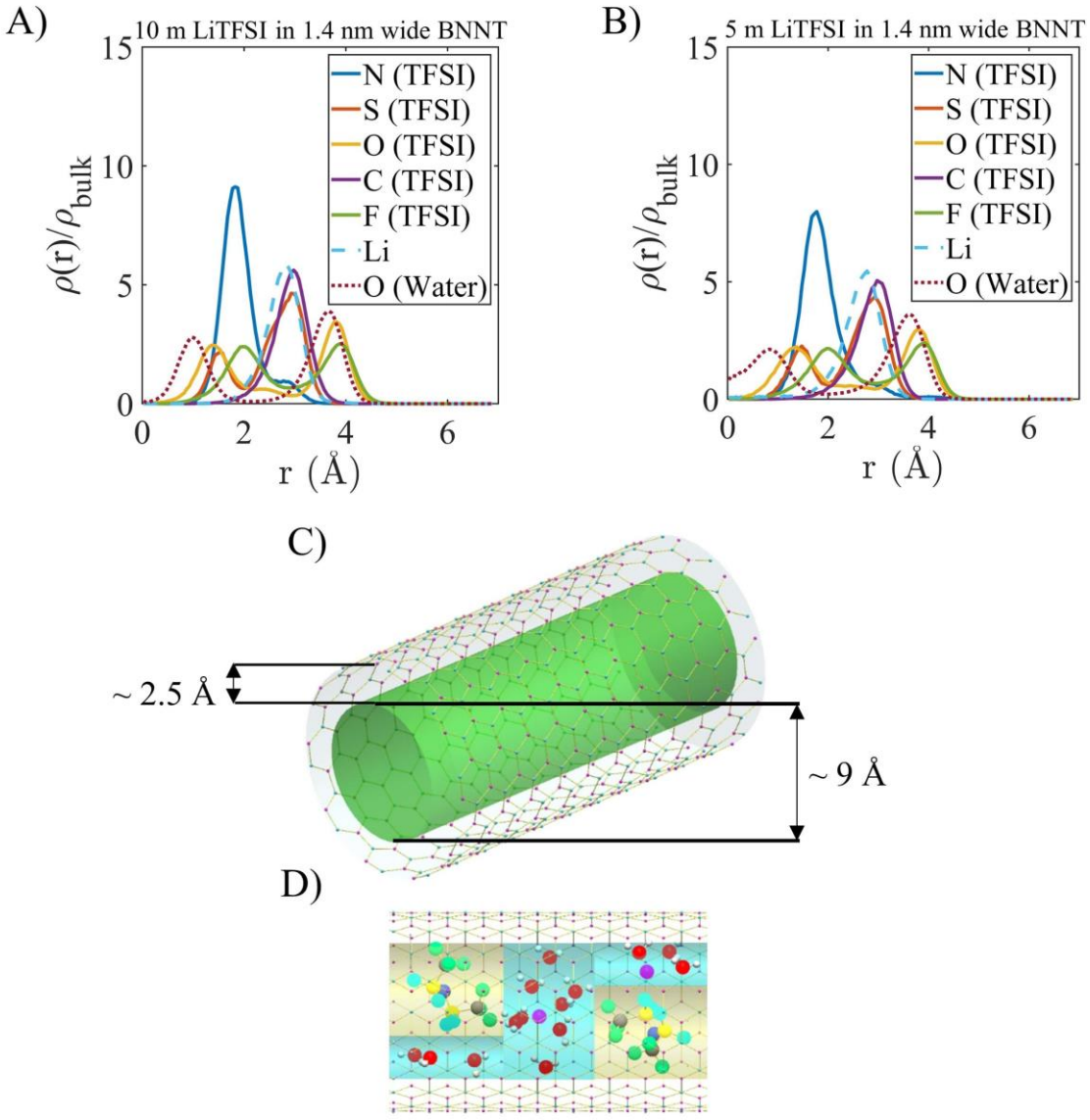

Figure 3.5. Radial distribution of the different atoms of the $TFSI^-$ ion, Li^+ ion, and the water oxygen atom for the cases of (A) 10 m LiTFSI WISE confined in a 1.4-nm-diameter BNNT and (B) 5 m LiTFSI WISE confined in 1.4-nm-diameter BNNT. (C) Schematic depicting the localization of all the species at much larger (as compared to the case of 1-nm-diamater BNNT, see Fig. 4C) radial distances (~ 4.5 Å) around the BNNT axis. (D) Schematic depicting the manner in which this localization at much larger radial distances around the BNNT axis [identified in (D)] allows the $TFSI^-$ ion and the water molecules to occupy the same axial but different radial locations. In figure 5D, pink particle: lithium ion; blue rectangle: water medium; green particles: fluorine atoms of the $TFSI^-$ ion; grey particles: carbon atoms of the $TFSI^-$ ion; yellow particles:

sulfur atoms in the $TFSI^-$ ion; cyan particles: oxygen atoms of the $TFSI^-$ ion; dark blue particles: nitrogen atoms in the $TFSI^-$ ion.

Axial and Radial Distribution of the Ions and Water Molecules in the Presence of an External Voltage Difference

To study the effect of the presence of the charged electrodes on the molecular ordering within the 1-nm-diameter BNNT, we consider the filling of the 1-nm-diameter BNNT with the BNNT being placed perpendicular to the negative electrode with one end of the BNNT blocked by the negative electrode while the other end of the BNNT being open to the bulk electrolyte. On the other hand, the positive electrode surface is entirely open to the electrolyte solution without the presence of a BNNT nearby. The set-up is illustrated in Figures 3.6A, 3.6D, and B1(b) (in appendix B). We applied an electric potential of -2.5 V on the left graphite electrode ($z < 0$) and the right graphite electrode was maintained at a potential of +2.5 V [see Figures 3.6A and 3.6D]. The BNNTs were initially empty, and were allowed to be filled by the electrolyte solution in presence of the applied electric potential difference. More details regarding the simulation procedure can be found in the Supplemental Experimental Procedures. In Figures 3.6B and 6E, we show the axial distribution of the nitrogen atoms (representing $TFSI^-$ ion), Li^+ ion, and water oxygen atoms (representing the water molecules) along the axis of the BNNT for the 10 m and 5 m WISE confined in 1-nm diameter BNNT in presence of an external axial voltage difference of 5V applied between the two graphite electrodes. *Most importantly, we observe that even in the presence of this applied voltage difference, $TFSI^-$ ion entered the BNNT prior to other electrolyte molecules [this is confirmed by Figures B2(c,d) in the appendix B], and the nanoconfinement-driven (or driven by the fact that the size of the $TFSI^-$ is very close to the diameter of the 1-nm*

BNNT) non-overlapping axial distributions of the nitrogen atoms (representing the TFSI- ions) and the water oxygen atoms (i.e., non-overlapping axial "blocks" of TFSI- ion and water molecules) persist resulting in the axial distribution profiles shown in Figures 3.6B and 3.6E. In other words, the axial distribution profiles of the nitrogen atoms and the water oxygen atoms for this case where there is an externally applied axial voltage difference are similar to the case where there is no externally applied axial voltage difference (see Figures 3.2B and 3.2E). In addition, we see a water-free $TFSI^-$ ion peak near the negative electrode as the $TFSI^-$ ion (that entered the BNNT first) restricts water from reaching the negative electrode due to the confinement effect of 1-nm-diameter BNNT. This confirms that water-free localization of the $TFSI^-$ at the negative electrode is possible even in the presence of a large applied voltage difference.

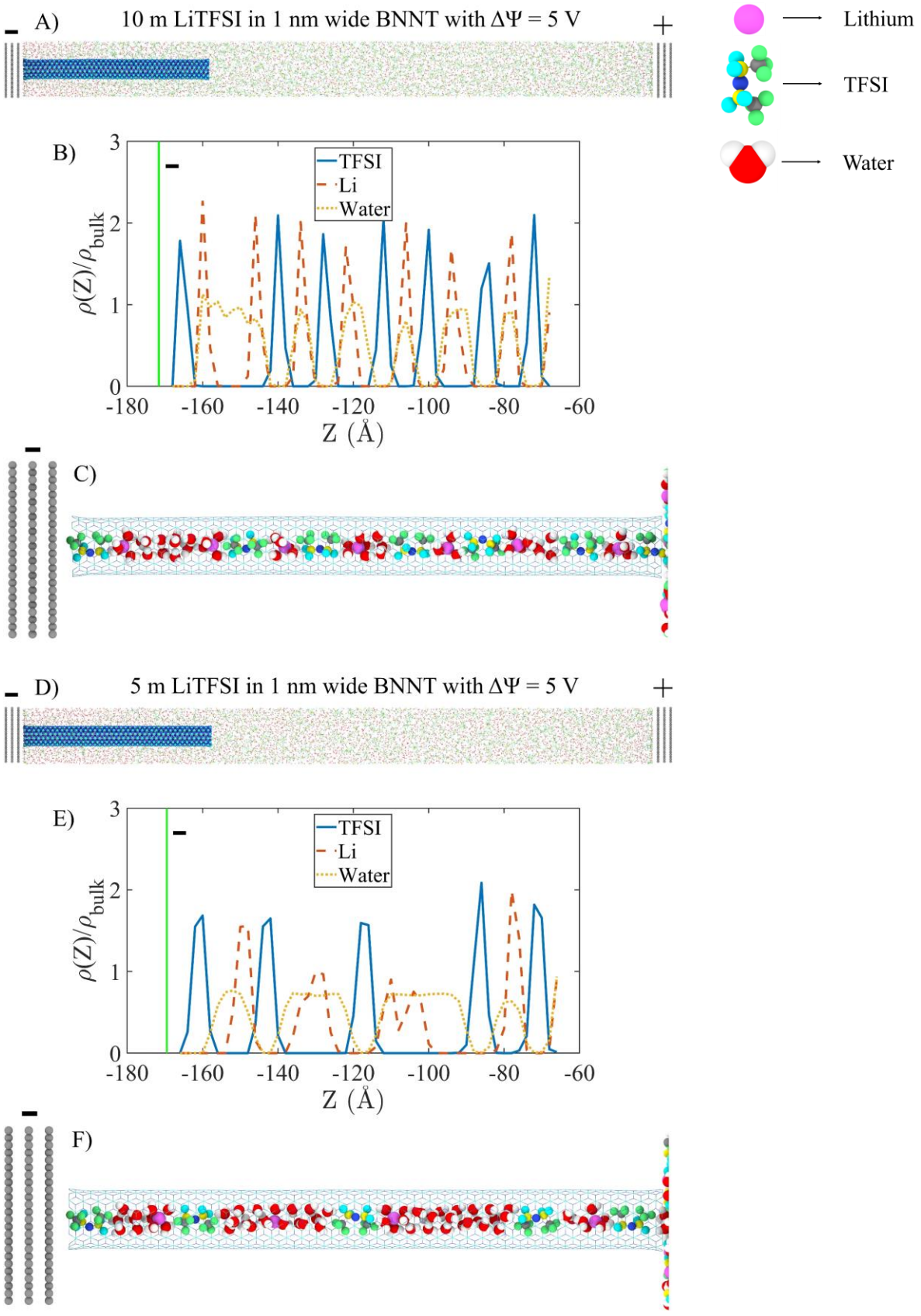
A)
10 m LiTFSI in 1 nm wide BNNT with ΔΨ = 5 V
B)
TFSI
Li
Water
ρ(Z)/ρbulk
Z (Å)
C)
D)
5 m LiTFSI in 1 nm wide BNNT with ΔΨ = 5 V
E)
TFSI
Li
Water
ρ(Z)/ρbulk
Z (Å)
F)
Lithium
TFSI
Water

Figure 3.6. MD simulation snapshots showing the entire system for the case of (A) 10 m LiTFSI WISE confined in 1-nm-diameter BNNT and (D) 5 m LiTFSI WISE confined in 1-nm-diameter BNNT. For this case an electric potential difference of 5 V is applied across these systems. The negative and positive electrodes are labeled accordingly and the electric potentials associated with those electrodes are -2.5 V and 2.5 V respectively. One end of the BNNT is placed near the negative electrode, while the other end is open to the bulk. Axial distribution of the nitrogen atoms (representing the $TFSI^-$ ion), Li^+ ions, and water oxygen atoms (representing the water molecules) for the cases of (B) 10 m LiTFSI WISE confined in 1-nm-diameter BNNT in presence of charged electrodes and (E) 5 m LiTFSI WISE confined in 1-nm-diameter BNNT in presence of charged electrodes. The green lines indicate the presence of a negative electrode with a potential of -2.5 V MD simulation snapshots showcasing the distribution of the different species including the local arrangement of salt ions and water molecules for the case of (C) 10 m LiTFSI WISE confined in 1-nm-diameter BNNT in presence of charged electrodes and (F) 5 m LiTFSI WISE confined in 1-nm-diameter BNNT in presence of charged electrodes. In (C) and (F), atoms surrounding the BNNT were removed, to provide a clearer picture of electrolyte distribution inside the BNNT. All the simulation snapshots are generated using OVITO[100].

The persistence of a non-overlapping axial distribution of $TFSI^-$ ions and the water molecules in the presence of the applied voltage difference is also established by the corresponding radial distribution profiles of the different atoms of the $TFSI^-$ ion and the water oxygen atom. These radial distributions (please see Figure B3 in the appendix B) are very similar to the corresponding radial distribution profiles in the absence of external voltage difference (see Figures 3.4A and 3.4B). Once the 1 nm BNNT is completely filled resulting in the non-overlapping, alternate blocks of $TFSI^-$ ions and water molecules, the electrolyte molecules cannot jump from one block to another due to the steric repulsions caused by the BNNT walls.

The distribution of nitrogen atoms (representing $TFSI^-$ ion), Li^+ ion, and water oxygen atoms near the positive electrode, which is completely open to the electrolyte, is shown in Figure B4 in the appendix B. Near the positive electrode, we see a $TFSI^-$ ion peak, for both 5 m and 10 m

aqueous LiTFSI. This shows the $TFSI^-$ anion dominance in the first interfacial layer, which agrees with previously reported studies.[97,135,136]

Therefore, by leveraging the combined effect of $TFSI^-$ ion's affinity to enter the BNNT prior to other electrolyte ions and molecules and the severe nanoconfinement effect caused by 1-nm-diameter BNNT (to the extent where the size of the $TFSI^-$ ion becomes closely comparable to the diameter of the 1-nm-diameter BNNT), we are able to create a most remarkable scenario where $TFSI^-$ ions are localized near the negative electrode in the complete absence of water. If a partially pre-lithiated anode[130,131,132,133,134] is utilized in this scenario, it might be possible to ensure the reduction of $TFSI^-$ ion and thus the formation of the SEI and prevention of the water reduction near the negative electrode. Such water-free localization of cation-anion pair near the negative electrode has been the broad purpose of using the WISE systems.[17] However, for achieving a cation-anion pair localization at the negative electrode, the existing LiTFSI WISE system (in absence of any confinement effect) needs to use a very large concentration (~ 21 m) of the salt.[17] On the contrary, by using an appropriate nanoconfinement (1-nm-diameter BNNT) and utilizing $TFSI^-$ ion's tendency to enter the BNNT prior to other moieties, we are able to achieve $TFSI^-$ ion localization at the negative electrode at a much smaller (5-10 m) concentration of the LiTFSI salt. This is the most important message of this paper. Therefore, this study also aims to provide a potential solution to address a key limitation of the existing WISE-based battery architectures stemming from the requirement of using a very large concentration of the electrolyte salt.

Affinity of $TFSI^-$ Ion to Enter the 1 nm-wide BNNT Prior to Hydrated Li^+ Ion

In Figure B5 of appendix B, we provide the free energy curves, as a function of axial position with respect to the BNNT entrance, corresponding to the entry of $TFSI^-$ ion and $Li^+(H_2O)_4$ (Li^+ along with its primary hydration shell) from bulk 5 m aqueous LiTFSI solution into the 1-nm diameter empty BNNT in the presence of an applied electric potential difference of 5 V (with an electric potential of -2.5 V at the negative electrode). We used the simulation setup as shown in Figure 3.6(D) to obtain these free energy curves. One end of the empty BNNT is blocked by negative electrode while the other end is open to the entry of $TFSI^-$ ion (or hydrated Li^+ ion). Further details regarding the simulations can be found in Supplemental Experimental Procedures in the SI. The free energy change associated with the entry of $TFSI^-$ ion is -7.55 kcal/mol and the change corresponding to the entry of hydrated Li^+ is -1.24 kcal/mol. While the entry of both, $TFSI^-$ ion and hydrated Li^+, is thermodynamically favorable, we can clearly see the greater affinity of $TFSI^-$ ion to enter the 1-nm diameter BNNT prior to the hydrated Li^+ ion. Also, we see a free energy barrier of 0.76 kcal/mol, outside the BNNT, associated with the entry of hydrated Li^+ into the BNNT. This was caused by the presence of a $TFSI^-$ ion, outside the BNNT and near the entrance, which was competing with hydrated Li^+ to enter the BNNT. This indicates that, when one end of the BNNT is grafted to negative electrode with the other end open to electrolyte, the first molecule that enters the BNNT through the open end will most likely be $TFSI^-$ ion. As the filling further proceeds and once the BNNT is completely filled, $TFSI^-$ ion gets localized, without any water, at the other end near negative electrode. We propose such a filling protocol to ensure the water free localization $TFSI^-$ ion inside the BNNT near negative electrode. Once the BNNT is completely filled, resulting in axial distributions as shown in Fig 3.6(B, E), $TFSI^-$ ion and water molecules cannot switch position due to the steric repulsion caused by the walls of 1 nm wide BNNT as

discussed in the above sections. These free energy curves support our claim that the $TFSI^-$ ion has higher affinity to enter the 1 nm wide BNNT prior to other species of the solution. A stronger binding effect between $TFSI^-$ anion and boron nitride (BN), compared to that of Li^+ and BN was previously reported in [19] through experiments and DFT studies. However, water was absent in that study and a comparison between binding effects of $TFSI^-$-BN and water-BN is crucial to support our findings.

Also, we have performed multiple filling simulations with different initial configurations, for both the cases of 5 m and 10 m aqueous LiTFSI, until the first species completely enters the BNNT and the results were reported in Figs B6 and B7 of appendix B (further details on the simulations can be found in Supplemental Experimental Procedures in the appendix B). These simulations were performed in order to check if our observations hold true for a significant number of filling events. As we can see from the filling profiles reported in Figs B6 and B7 (in appendix B), in all the twenty simulations (ten simulations each for the cases of 10 m and 5 m LiTFSI solutions), $TFSI^-$ ion is always the first species to completely enter the 1 nm wide BNNT. In a few simulations (like simulation 7 in Fig B6 and simulation 1 in Fig B7 in appendix B), even though we see an initial presence of water molecules at the BNNT entrance (indicated by the initial non-zero water count), those water molecules were eventually replaced by a nearby competing $TFSI^-$ ion which caused the water count to drop to zero and the $TFSI^-$ ion count to raise. These results, which conclusively prove that *the event of the TFSI anion entering a neutral BNNT before water or Li+ entering BNNT is indeed a highly significant event that occurs all the time*, add strength to our prediction that the $TFSI^-$ ion has a much higher affinity to enter the 1 nm wide BNNT prior to other species of the solution.

Finally, it will be useful for the readers to have a mechanistic description (that get unraveled from our MD simulations) dictating the filling of the BNNT. First, when the BNNT is allowed to be filled, it is observed that every time, regardless of the initial conditions starting from which the BNNT is allowed to be filled, $TFSI^-$ ion is always the first species to completely enter the 1 nm wide BNNT. This becomes possible since the $TFSI^-$ ion has a much larger affinity to the BNNT, as compared to the affinity of water (or the hydrated Li^+ ion) to the BNNT. Second, once one $TFSI^-$ ion has entered the BNNT, the next species to enter the BNNT cannot be another $TFSI^-$ ion due to the fact that this second $TFSI^-$ will be strongly repelled away by the first $TFSI^-$ that has entered the BNNT. Accordingly, the second species to enter BNNT will be the water molecule (or a hydrated Li^+ ion). The fact that the size of the $TFSI^-$ ion is very close to the diameter of the 1-nm BNNT, this water molecule (or a hydrated Li^+ ion) will invariably trail behind the $TFSI^-$ ion. In other words, this water molecule will never be able to cross over the $TFSI^-$ ion and come in between the already entered $TFSI^-$ ion and the negative electrode and therefore, will always remain in between the $TFSI^-$ ion and the entrance of the BNNT. This sequential entry mechanism will continue and coupled with the fact that the size of the $TFSI^-$ ion is very similar to the diameter of the 1-nm BNNT, thereby forbidding any water molecule from crossing over the TFSI- ion, will ensure the attainment of our proposed structure where there are axially non-overlapping "blocks" of the $TFSI^-$ ion and the water molecules (or hydrated Li^+ ion) confined within the 1-nm BNNT. The critical thing to note here is that this entire filling procedure takes places in presence of a negative electrode localized at the other end (the closed and non-filling end) of the BNNT. Accordingly, given the fact the $TFSI^-$ ion is always the first species to enter the BNNT and there is no cross-over between the axially separated "blocks", it is this $TFSI^-$ ion that gets localized near the negative electrode at the end of the filling process. It is important to note that while $TFSI^-$ ion is the species that is closest

to the negative electrode, the repulsion from the negative electrode ensures that there is an axial gap of nearly 0.5 to 1 nm (depending on the electrolyte concentration) between the location of the negative electrode and the position of the nitrogen atom of $TFSI^-$ ion (representing the location of the local peak in the TFSI ion density, see Figures 3.6B,E) where majority of the negative charge density is present. Also, this $TFSI^-$ ion stays in the vicinity of the negative electrode despite this repulsive force since it is not possible for it to leave the BNNT. Firstly, it is not possible to leave the BNNT in the radial direction, given the presence of the BNNT walls. Secondly, given the fact that the size effect (i.e., the fact that the size of the BNNT closely resembles the diameter of the 1-nm BNNT) prevents any crossing over of the axially separated blocks, in order to escape axially, this $TFSI^-$ ion must first force all the other species that have entered the BNNT after it out of the BNNT. This is extremely unfavorable energetically, given that all the species have spontaneously entered the BNNT. Since such a scenario is not possible, this $TFSI^-$ ion that had entered the BNNT first remains in its position with its nitrogen atom at a certain distance (0.5 – 1 nm) away from the negative electrode and our proposed structure, where there are axially separated "blocks" of $TFSI^-$ ion and hydrated Li^+ ion confined in the 1-nm-diameter BNNT, remains stable.

Effect of Weaker LiTFSI Concentration on the Anion Localization at the Anode

In Figure B8 in appendix B, we provide the results for the case of much weaker concentration of the LiTFSI salt (1 m) confined within the 1-nm diameter BNNT in presence of an axial voltage differnce of 5 V with -2.5 V being employed at the negative electrode near a BNNT end, as shown in Figure B8(a) (see appendix B). Results [Figure B8(b) in appendix B] show that while the localization of the $TFSI^-$ ion still persists near the negative electrode, the Li^+ ion concentration peak is deviated further away from the negative electrode and there is a lack of Li^+ ion near the

negative electrode. This is caused by the combined effect of lower availability of Li^+ near the BNNT entrance (due to weaker concentration) and the higher affinity of $TFSI^-$ ion to enter the tube. This lack of Li^+ ion, at a weaker LiTFSI concentration, in the vicinity of anode could hinder the (de)lithiation process and such hindrance is detrimental to battery performance. While we don't identify a critical value, we work with a concentration (5 m and 10 m) of the LiTFSI salt that is large enough to ensure that the Li^+ ions will be immediately available for (de)lithiation process once the $TFSI^-$ ion near the partially pre-lithiated anode reduces to form a SEI.

Water-free Localization of Anion at the Anode for Other Types of Salts Known to Form WISE Systems

Finally, we test our hypothesis of water-free localization of anion at the negative electrode, driven by a BNNT of 1-nm diameter, for another type of salt, namely LiBETI, well-known to form WISE systems.[106] (the results are provided in Figure B9 in appendix B). We consider a solution of 5m LiBETI, with the simulation setup as shown in Figure B9(a) (please see appendix B), and study the axial distributions of the different atoms and ions of the electrolyte in the 1-nm diameter BNNT in presence of an axial voltage difference of 5 V [see Figure B9(b) in apppendix B]. A negative potential of -2.5 V is applied to the negative electrode near a BNNT end as shown in subfigure B9(a) (in appendix B). As can be seen from the axial distribution profiles, we indeed observe a water-free $BETI^-$ ion localization near the negative electrode. This stems from the fact that $BETI^-$ ion, a derivative of $TFSI^-$ ion, is large enough to become closely comparable to the size of the 1-nm-diameter BNNT and has higher affinity to enter the BNNT prior to hydrated Li^+ (please see Figure B10 in appendix B). These findings for the solutions of different salts help to establish our hypothesis of nanometer wide BNNT driven water-free localization of anion near the negative

electrode using an aqueous solution of a salt with a large anion derived from $TFSI^-$ (typically those known to form WISE systems).

3.3 DISCUSSIONS

In this paper, we employ MD simulations to propose a most remarkable possiblity of ensuring water-free localization of anion near the negative electrode with aqueous solution of TFSI derived salts (known to form WISE systems) using nanometer wide BNNT. Most importantly, we find that such localization occurs at a salt concentration that is several times smaller than that needed for localization of the cation-anion pair for the aquoeus solution of the same salt in absence of any confinement. Such cation-anion pair localization at the negative electrode, with the anion based on fluoroalkyl sulfonylimide or fluoroalkyl sulfonate, and the lack of free water have been identifed as important factors that result in the formation of a stable SEI, which leads to the large efficacy of using WISE systems for battery applications.[17] Of course, a key bottleneck of using such WISE systems stems from the need of employing a very large concentration of the such salt. For example, ~21 m of LiTFSI salt is needed for achieving such cation-anion pair localization that improves the electrochemical stability window for the batter application.[17] On the other hand, by using nanoconfinement effect caused by nanometer wide BNNT, we observe such water-free localization of the $TFSI^-$ anion at the negative electrode for much smaller concentration of the salt (5 m and 10 m). The nanoconfinement effect refers to the size of the $TFSI^-$ ion becoming closely comparable to the diameter of the 1-nm BNNT which results in the formation of non-overlapping blocks of $TFSI^-$ ions and water molecules. The affinity of $TFSI^-$ ion to enter the BNNT prior to hydrated Li^+, in addition to the above mentioned nanoconfinement effect, further ensures the

presense of water-free $TFSI^-$ ion localization inside 1-nm-diameter BNNT near the negative electrode. If a partially pre-lithiated anode is utilised in this scenario, one can ensure the formation of the SEI and prevent water reduction resulting in a safe aqueous lithium ion battery. Our hypothesis is further established by studying the behavior of the solutions of other salts known to form WISE systems (e.g., LiBETI) in 1-nm-diameter BNNT: for the LiBETI, the $BETI^-$ ion, a derivative of $TFSI^-$ ion, is closely comparable to the size of the 1-nm-diameter BNNT and has a higer affinity to enter the BNNT prior to hydrated Li^+ ion leading to such water-free localiation of the $BETI^-$ ion at the negative electrode. We expect that in future extensive experiments could be conducted to confirm our simulation-driven hypothesis of water-free anion localization at anode.

3.4 Methods

Molecular Dynamics Simulations

All the simulations were performed using the LAMMPS parallel MD package.[84] In all the simulations, a Nosé Hoover thermostat,[85,86] with a damping constant of 100 fs, was used. Also, for simulations involving isobaric equilibration, a Nosé Hoover barostat was used with a damping constant of 1000 fs. We used CL&P[87] force field parameters to model LiTFSI and LiBETI. Originally developed for the ionic liquids, these force fields were shown to be capable of accurately predicting the structural properties of the WISE solutions.[97] Water was simulated using the SPC/E model.[88] The non-bonded force field parameters for the BNNTs were obtained from Won and Aluru[20, 91] and for both the tubes [1.0-nm (7, 7) BNNT) and 1.4 nm (10, 10) BNNT)], we included the charges on the BNNT surface in the presence of water that have been reported in previous studies.[20] The interatomic Lennard Jones (LJ) parameters were obtained using the geometric mixing rules. A cutoff distance of 12 Å was used for both the Lennard Jones (LJ) and Columbic interactions. The PPPM[92] solver was used, with an accuracy of 0.0001, to calculate long-range electrostatic interactions. For simulations involving isobaric equilibration, the interaction between atoms within the BNNTs were modeled using the Tersoff potential[89] with parameters given in Kınacı *et al.*[90] We used the constant potential method (CPM),[137, 138] implemented in LAMMPS by Wang *et al.*,[139] to maintain a desired electric potential difference between the electrodes. A time step of 1 fs was used for all the simulations and, unless mentioned otherwise, all the data was outputted every 500 time steps.

First, we performed MD simulations in which open-ended boron nitride nanotubes (BNNTs) with 1 nm diameter [BNNT (7, 7)] and 1.4 nm diameter [BNNT (10, 10)] were soaked in 5 m and 10 m LiTFSI aqueous solutions. A bond distance of 1.446 Å between the boron and

nitrogen atoms was considered[20] and the nanotubes were generated using the VMD.[93] Since the charges on (7, 7) BNNT were not reported, we have used the values reported for nanotube with nearest size [(6, 6) BNNT].[20] For simulations with 5 m LiTFSI, 996 LiTFSI pairs along with 10956 water molecules were used and for simulations involving 10 m LiTFSI, 1380 LiTFSI pairs and 8280 water molecules were used. In all these simulations, the simulation box was initially filled with the solution atoms leaving enough space in the middle of the box to fit the BNNT. Both the 1-nm and 1.4-nm diameter BNNTs were 10 nm long containing 1120 and 1600 atoms, respectively. First, the solution surrounding the BNNTs was pre-equilibrated for 100 ps in the isothermal-isobaric (NPT) ensemble with a temperature of 300 K and a pressure of 1 atmosphere. During this pre-equilibration, the ends of the BNNTs were blocked to prevent filling at this stage. After the initial pre-equilibration, the aqueous LiTFSI solution was allowed to fill the nanotube and all the atoms were simulated in the NPT ensemble at a temperature of 300 K and a pressure of 1 atmosphere. In order to prevent the nanotubes from drifting away, boron and nitrogen atoms at the two ends of the BNNT were tethered to their initial positions using springs with a stiffness of 23 kcal/mol.Å^2. Periodic boundary conditions were used in all the three directions. The simulation snapshot of 1-nm-diameter BNNT soaked in 10 m LiTFSI aqueous solution is shown in Fig B1(a). All these simulations lasted for 15 ns, and the data from the last 5 ns was used for the analysis. From these simulations, we confirm the molecular ordering of LiTFSI aqueous solution confined in a 1-nm-diameter BNNT. Also, in all the simulations involving 1-nm-diameter BNNT, we observed that anion enters the tube first from both of its ends. So, to prevent the initial trapping of anions inside the 1-nm-diameter BNNT, the solution was allowed to enter and fill the BNNT only through one of the two entrances. Once the BNNT is completely filled, the blocks were removed

and the system was allowed to equilibrate. The first 300 ps of the filling process of 5 m and 10 m LiTFSI inside the 1-nm-diameter BNNT can be seen in Fig. B2(a,b) in appendix B.

Later, we have performed simulations in which we place graphite electrodes at both the ends of the 10 m and 5 m WiSE systems with a 10 nm long (7, 7) BNNT (1 nm diameter) placed near the left electrode ($z < 0$) where we apply a negative electric potential [see Fig. B1(b) in appendix B]. As shown in Fig. B1(b), the axis of the BNNT is perpendicular to the negative electrode with one of its ends blocked by the negative electrode while the other end is open to bulk electrolyte. The BNNTs and electrodes were fixed during these simulations and the BNNT was initially geometry optimized, using Tersoff potential,[89] with the electrolyte solution surrounding it. First, we equilibrate these systems, without applying an electric potential difference between the electrodes, in the isobaric-isothermal ensemble with a temperature of 300 K and the z component of the pressure tensor maintained at 1 atm. Periodic boundary conditions were used, in all three dimensions, during these runs. These simulations lasted for 5 ns and the data from last 1 ns was used to calculate the equilibrated box length in the z direction. Using the equilibrated system sizes obtained from the above simulations, we have simulated the filling of the 1-nm-diameter BNNTs in the presence of an applied electric potential difference of 5 V between the electrodes. These simulations were performed in the canonical ensemble with a temperature of 300 K. The BNNTs were initially empty and the surrounding electrolyte was pre-equilibrated for 1.5 ns before starting the filling process. To block the solution from entering the BNNT during pre-equilibration, we have used a circular Lennard Jones (LJ) wall (with a radius of 5 Å) at entrance of the BNNT. The interaction parameters, namely epsilon and sigma, between this LJ wall and all the solution atoms is given by 0.02 kcal/mol and 1 Å respectively. Also, to ensure a minimal effect of this LJ wall on the solution atoms away from the BNNT entrance, a cutoff distance of 1 Å was

used beyond which the wall interactions disappear. A negative electric potential of -2.5 V is applied to the electrode that is blocking one end of the BNNT while a positive electric potential of 2.5 V is applied to the opposite electrode, which is far away from the BNNT. The carbon atoms in the graphite electrodes were modeled using the OPLS-AA[140] force field parameters and each graphite electrode consisted of three graphene layers. The BNNTs and electrodes were fixed during these simulations with electrodes being parallel to the x-y plane and the BNNT aligned along the z-axis. The simulation cell dimensions were 29.4726 Å × 29.778 Å in the x-y plane and the box length in z dimension varied from 360 Å to 347 Å for the various systems we simulated. Periodic boundary conditions were used in the x and y directions and a volume factor of 3 was used to account for the slab correction[94] in the z direction while calculating the long-range Columbic forces. We used the constant potential method (CPM),[137, 138] implemented in LAMMPS by Wang *et al.*,[139] to maintain the electric potential difference between the left (z<0) and the right (z>0) graphite electrodes at 5 V (-2.5 V and 2.5 V respectively on the left and right electrodes). The charges on the electrodes were updated every 100 fs and a Gaussian width parameter of 0.5 Å was used. All these simulations lasted for 15 ns and the data obtained from the last 5 ns was used for the analysis. For this case too, we find that that the $TFSI^-$ ion enters the BNNT first. The first 300 ps of the filling process of 5 m and 10 m LiTFSI inside the 1-nm-diameter BNNT in presence of the charged electrode can be seen in Fig. B2(c,d) in appendix B. Other results from the simulation are provided in Fig. 6 in the main paper and Fig. B3. We have also performed simulations, following the procedure described above, with 1 m LiTFSI aqueous solutions (results reported in Fig. B5 in appendix B) and 5 m LiBETI (results reported in Fig. B6 in appendix B) filling the 1-nm-diameter BNNT in the presence of an external potential difference of 5 V.

The free energy curves corresponding to the entry of $TFSI^-$ ion and hydrated Li^+ ion into the empty 1 nm diameter BNNT were obtained by employing umbrella sampling method on the system, with 5 m LiTFSI surrounding 1 nm wide BNNT in the presence of an applied electric potential difference of 5 V [please see the system setup shown in Fig. 3.6(A)]. In these simulations, the axial position of the $TFSI^-$ ion (or the hydrated Li^+ ion) with respect to the BNNT entrance is considered as the reaction coordinate. The whole range of the reaction coordinate was divided into windows and the center of mass for sample $TFSI^-$ ion (or hydrated Li^+ ion) is constrained to these windows using a harmonic potential with spring constants varying from 1-8 kcal/mol.$Å^2$. For the case of $TFSI^-$ ion, we used five windows with z = -64 Å, -65.5 Å, -67 Å, -68.5 Å and -70 Å as the equilibrium positions for the constraining harmonic potential in those windows. On the other hand, we used four windows for the case of hydrated lithium with z = -65.5 Å, -67 Å, -68.5 Å and -70 Å as the equilibrium positions for the constraining harmonic potential. The BNNT entrance was located at z = -67.8 Å, and the $TFSI^-$ ion (or hydrated lithium ion) center of mass axial positions were sampled from -2.7 Å (inside BNNT) to 2.8 Å (outside BNNT) with respect to the BNNT entrance. The radial position, with respect to BNNT axis, of sample $TFSI^-$ and hydrated lithium are constrained to a radius of 5 Å outside the BNNT using a cylindrical LJ wall. Only the sample $TFSI^-$ ion or the sample hydrated lithium ion are allowed to enter the BNNT during sampling. The sample hydrated lithium is generated by coupling four water molecules to Li^+ (the solvation number of Li^+ at 5 m LiTFSI concentration) at a radial distance of 2 Å (first peak of Li – water oxygen RDF) with springs of 5 kcal/mol.$Å^2$ stiffness. The BNNT was empty in all these simulations (except for the presence of sample $TFSI^-$ or hydrated lithium) and the electrolyte surrounding the BNNT was pre-equilibrated for 1.5 ns. All these simulations lasted for 4 ns and the data collected from the last 3.5 ns was used for analysis. The axial positions of the sample

molecules were output every 500 fs and the weighted histogram analysis method (WHAM)[94, 95] was used to analyze the data generated from umbrella sampling. The free energy curves are reported in Fig. B5 (please see appendix B) by taking the value of free energy outside the BNNT (at the axial position of 2.8 Å with respect to BNNT entrance) as the reference.

Finally, different initial configurations for multiple filling simulations (results reported in Figs. B6 and B7 in appendix B), of 5 m and 10 m LiTFSI filling into 1 nm wide BNNT in the presence of an applied electric potential difference of 5 V, are generated in the following manner. First, we have pre-equilibrated the electrolyte solution surrounding the empty BNNT, in presence of an applied electric potential difference of 5 V, in the canonical ensemble at a temperature of 300 K. The pre-equilibration lasted for 3 ns and the solution was blocked from entering the BNNT, using a LJ wall as described in previous paragraphs, during this period. Later, from the last 2 ns of the above described pre-equilibration, we have selected a system configuration every 200 ps resulting in ten different states corresponding to timesteps at 1.2, 1.4, 1.6, 1.8, 2.0, 2.2, 2.4, 2.6, 2.8 and 3.0 ns. We have used these ten different states as initial system configurations for the filling-simulations. Further, to make sure that these different initial states do not have memory of each other, we have randomized the velocities of solution atoms before starting the filling simulations. We have followed the above described procedure for both the cases of 10 m and 5 m aqueous LiTFSI solutions. Using these initial states, we have performed filling-simulations, in the canonical ensemble at a temperature of 300 K, for 500 ps in the presence of an applied electric potential difference of 5 V.

The contents of this chapter have been published as Chava, B. S., Chandel, G. R., & Das, S. (2023). Water-Structure-Specific Entropic Dominance in the Filling of Boron Nitride Nanotubes. *The Journal of Physical Chemistry C, 127*(14), 7009–7018.

Chapter 4: Water-Structure-Specific Entropic Dominance in the Filling of Boron Nitride Nanotubes*

Abstract

The filling of nanometer and sub-nanometer channels/tubes with water governs applications ranging from desalination and filtration to nanoscale energy conversion. Here we report the most non-intuitive entropy-dominated filling of mildly hydrophilic boron nitride nanotubes (BNNTs) from 0.85 to 1.69 nm diameters. For all the BNNT sizes, water inside the BNNT is more stable than water in the bulk. The factor dictating the favorable nature of the entropy depends on the specific-BNNT-diameter-dictated structure of the water molecules. For example, for the 0.85-nm BNNT, rotational entropic component dominates due to the presence of a significant fraction of the dangling water OH bonds that do not participate in hydrogen bonding. The fraction of such dangling OH bonds (the average HBs per molecule) decreases (increases) with an increase in the BNNT diameter leading to a progressively reduced contribution of the rotational entropy. For the 1-nm BNNT, translational entropic component dominates stemming from the enhanced in-plane motion of the water molecules caused by the single-file nature of water molecules spanning a significant radial expanse inside the BNNT. For larger BNNTs, translational entropy decreases with an increase in BNNT diameter, although it remains the dominant factor governing the entropy driven filling of BNNTs. This favorable translational entropy for larger BNNTs can be associated to (1) the presence of chain-like regions formed by water in 1.13-nm BNNT and (2) the presence of high specific water volume and reduced number of HBs per molecule (as compared to bulk water) in 1.27-nm, 1.41-nm, 1.55-nm, and 1.69-nm BNNTs.

4.1 Introduction

Nanofluidics,[141-145] over the past couple of decades, have emerged as a subject of great significance with applications ranging from sensing,[146,147] water treatment (such as desalination[148-150] and purification[151,152]), nanoscale energy conversion,[153,154] and many more. The dominant role of the surface physics and the specific structure of the nanochannel and the liquid molecules (water molecules) govern all these applications. Therefore, there have been immense interests in the fundamental explorations of the behavior and properties of liquid molecules (or more specifically, water molecules) inside the more commonly available (or manufacturable) nanochannels and nanotubes. Carbon nanotube (CNT) is an example of one such most commonly used nanotube and extensive research has elucidated a myriad of most fascinating effects associated with the transport of water confined inside the CNTs[155-158] and the manner in which these properties are leveraged for a wide-ranging nanofluidic applications.[13,159-161] In comparison, the fundamental exploration of the behavior and properties of water inside boron nitride nanotubes (BNNTs), which very much like the CNTs are easily fabricable with diameters being in the range from less than one nanometer to a few nanometers,[162] have been significantly less and the existing studies[15,20,21,22,61,163-168] rarely shed much light on the BNNT-diameter-dependent changes in the thermodynamic factors (free energy, internal energy, and entropy) dictating the stability of water inside the BNNTs. Such knowledge of the water behavior inside the BNNTs is key for a more widespread use of BNNTs (and non-graphene, non-CNT-based nanomaterials, in general) in nanofluidic devices.

In this paper, we conduct molecular dynamics (MD) simulations using Reax force field (ReaxFF) parameters to study the thermodynamic factors dictating the stability of water inside BNNTs of diameters (D) ranging from 0.85 nm to 1.69 nm. Fig. 4.1(a-g) provides the MD simulation snapshots showing the distribution of water molecules inside the BNNTs of different

diameters. For all the BNNT sizes, water inside the BNNTs is found to be more stable than water in the bulk. It is expected that in a mildly hydrophilic nanotube like BNNT, the favorable internal energy change will be responsible for such water stability inside the BNNTs. On the contrary, we find that internal energy changes have minimal contributions towards the stability of water molecules inside the BNNTs; rather it is the extremely favorable entropy changes that ensure the significant stability of the water molecules inside the BNNTs of all sizes, despite the fact that it is conventional wisdom that confinement leads to unfavorable entropic changes. Pascal *et al.*[169] had first challenged this conventional wisdom: their paper established that the favorable entropic changes led to spontaneous filling of the hydrophobic CNTs (carbon nanotubes) from 0.8 to 2.7 nm. The present study establishes the same entropic dominance in the filling of BNNTs of all the sizes considered, albeit the factors governing the entropic dominance are different for the case of BNNTs (and depend on the diameter of the BNNT) as compared to CNTs. For example, in the sub-nanometer wide BNNT (D=0.85 nm), rotational entropy change ($T\Delta S_{Rot}$) dominates the favorable entropic contribution: such favorable $T\Delta S_{Rot}$ stems from the presence of a large number of dangling water OH bonds [see Fig. 4.1(h)] that do not participate in hydrogen bond (HB) formation and enable the water molecules to undergo rotation by either rotating about the OH bond participating in hydrogen bonding or by flipping about the axis perpendicular to the plane of the water molecule. The number of dangling water-OH bonds and the corresponding contribution of $T\Delta S_{Rot}$ in dictating the favorable entropic changes decrease progressively with an increase in the BNNT diameter. Therefore, for water molecules in larger BNNT diameters (D >= 1 nm), the changes in the translational entropy ($T\Delta S_{Trans}$) dominate the favorable entropy changes leading to water stability inside the BNNTs. However, in these wider BNNTs (D >= 1 nm), $T\Delta S_{Trans}$ itself decreases with an increase in the BNNT diameter. Of course, depending on the BNNT diameter,

different physical factors lead to the dominating influence of $T\Delta S_{Trans}$. For example, for D=1.0 nm, *i.e.,* the BNNT diameter for which $T\Delta S_{Trans}$ is most favorable, the enhanced in-plane motion of the water molecules, stemming from the single-file nature of water molecules that can traverse a significant radial expanse inside the BNNT, leads to an enhanced $T\Delta S_{Trans}$. On the other hand, the favorable $T\Delta S_{Trans}$ results from the presence of chain-like regions in the water structure in 1.13-nm BNNT and from the enhanced specific water volume and a smaller number of HBs per molecule (as compared to bulk water) in 1.27-nm, 1.41-nm, 1.55-nm, and 1.69-nm BNNTs. Many previous computational works studying the behavior of water confined in BNNTs have used force field parameters that significantly overpredict the BN hydrophilicity[22, 21, 15, 20] resulting in a water-BN contact angle of ~30°. The Reax force field (ReaxFF) parameters used in this study predict a water-BN contact angle of ~70° [24] which is close to the 66° value reported in recent experiments.[23] Further, these force field parameters were shown to produce excellent agreement with the experimental findings of bulk water structure.[170] Owing to the accuracy of our ReaxFF MD simulations, we expect our results to be well representative of a real-world picture. We anticipate that our findings will enable a better utilization of systems consisting of water confined in BNNTs for a wide range of applications in the field of nanofluidics.

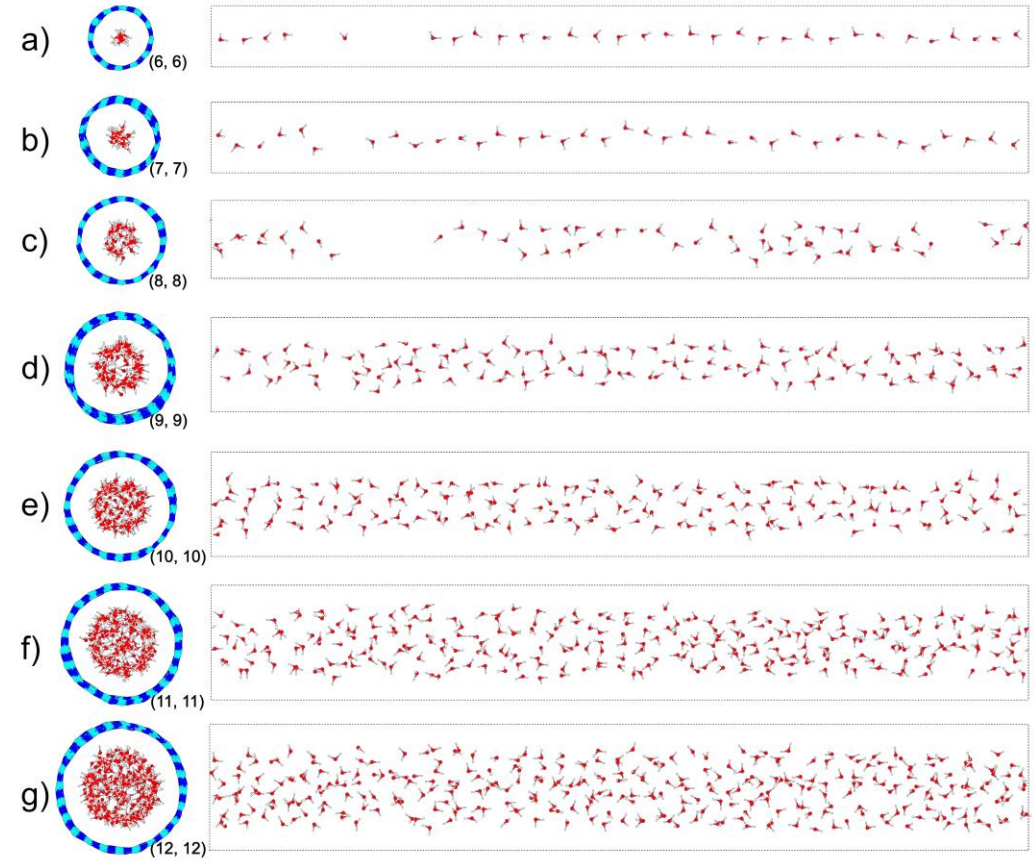
a)
(6, 6)
b)
(7, 7)
c)
(8, 8)
d)
(9, 9)
e)
(10, 10)
f)
(11, 11)
g)
(12, 12)

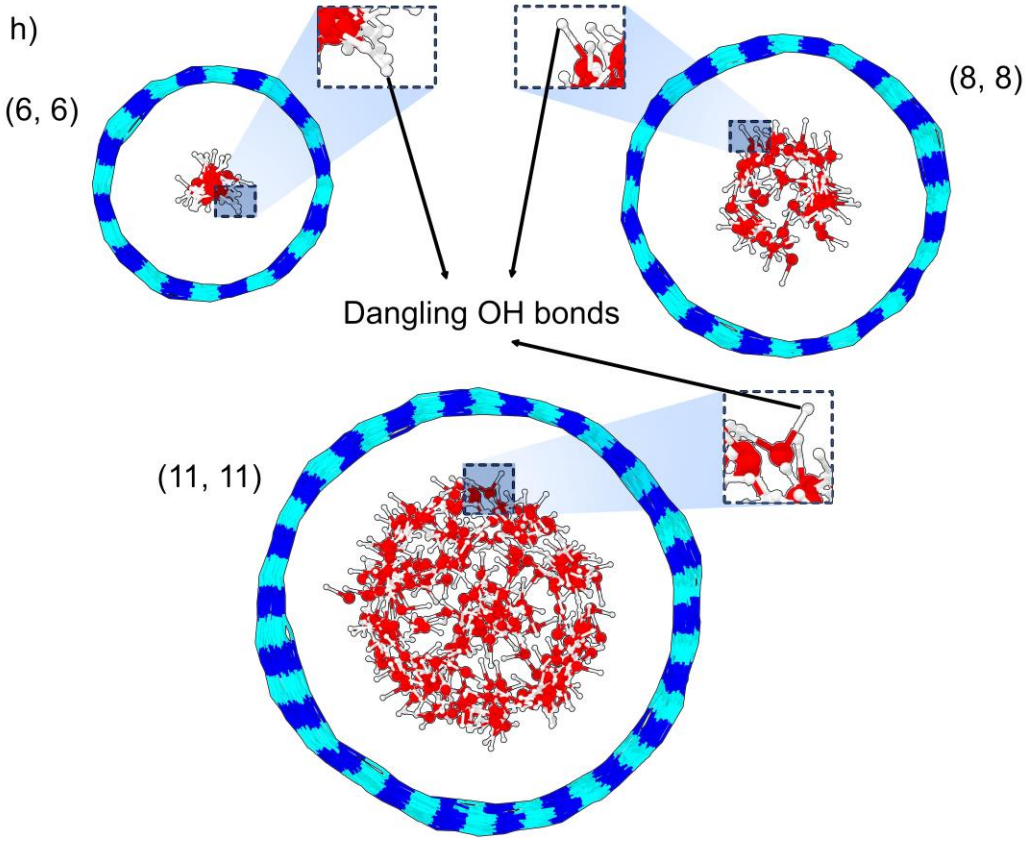
h)
(6, 6)
(8, 8)
Dangling OH bonds
(11, 11)

Figure 4.1. Simulation snapshots showing the cross-sectional and axial view of water confined in a) (6, 6) BNNT (D = 0.85 nm), b) (7, 7) BNNT (D = 1 nm), c) (8, 8) BNNT (D = 1.13 nm), d) (9, 9) BNNT (D = 1.27 nm), e) (10, 10) BNNT (D = 1.41 nm) f) (11, 11) BNNT (D = 1.55 nm), and g) (12, 12) BNNT (D = 1.69 nm). h) Magnified cross-sectional snapshots of the water molecules in (6, 6), (8, 8) and (11, 11) BNNTs highlighting the dangling water-OH bonds.

4.2 Methods

We consider BNNTs of seven different diameters with the following chiral indices: (6, 6), (7, 7), (8, 8), (9, 9), (10, 10), (11, 11) and (12, 12). First, we simulate 4-nm long open ended BNNTs soaked in bulk water made up of 3000 water molecules (see Fig. C7 in appendix C). The initial states for these simulations were obtained by pre-equilibrating the systems using the force fields reported in Won and Aluru.[20] During the pre-equilibration, all the BNNTs were completely filled with water molecules, consistent with the results from previous studies using these force field parameters. We used these configurations with completely filled BNNTs as initial states for the ReaxFF [171] MD simulations. This choice of initial states serves two main purposes. First, we can make sure that our observations from the ReaxFF simulations do not result from the water molecules being trapped in a local minimum outside the BNNTs. Second, we can speed up the equilibration of these systems by accelerating the initial filling process. These systems were simulated in the isothermal-isobaric (NPT) ensemble at a temperature of 300 K and a pressure of 1 atmosphere using Nosé Hoover[85,86] thermostat and barostat with damping constants of 100 and 1000 timesteps, respectively. In order to prevent the nanotubes from drifting away, boron and nitrogen atoms at the middle of the BNNT were tethered to their initial positions using springs with a stiffness of 20 $kcal.mol^{-1}.Å^{-2}$. Periodic boundary conditions were used in all the three directions. The average water density inside the BNNTs were obtained using the production data from these simulations. To minimize the effect of tube open ends, only the water molecules in the middle region (of length 3 nm) of the tube were considered. The total simulation length, production length and the average water count per unit tube length for each nanotube are provided in Table C1 (see appendix C). Using the water density data, we have filled 10.24 nm long periodic BNNTs with appropriate amount of water to simulate infinitely long water-filled BNNTs. The

simulation box spanned 10 nm in the *x* and *y* directions with the BNNT axis being parallel to the *z* direction (see Fig. C8 from appendix C). To prevent the BNNTs from drifting away, the BNNT atoms at the middle were tethered to their initial positions using springs. These systems were initially equilibrated in the NPzT ensemble (at a temperature of 300 K and a pressure of 1 atm) for 5 ns and the data from the last 2 ns were used to calculate the average box length along the z-axis. Next, from the equilibrated NPzT ensemble trajectory for each BNNT diameter, we picked the system configuration with the box length being closest to the ensemble average value, and continue the simulations in the NVT ensemble at a temperature of 300 K for 7 ns. From the last 6 ns of these simulations, we obtained 40 different 100 ps long trajectories that are separated from each other by 50 ps. Similarly, we have performed bulk water simulations using 1000 water molecules in the NPT ensemble for 500 ps followed by a simulation in the NVT ensemble for 1.75 ns. The last 1.5 ns of this NVT simulation resulted in 10 individual 100 ps long trajectories that are spaced 50 ps apart. For all the ReaxFF MD simulations, a time step of 0.25 fs was used. The LAMMPS parallel MD[84] engine was used to perform all the simulations. We employed the force field parameters reported in Verma *et al.*[24] along with the charge equilibration scheme (Qeq)[172, 173] for all the ReaxFF MD simulations. The position and velocity information of the atoms were saved every 0.5 fs for the above described 100 ps long trajectories and this data was used to calculate the entropy, density of states (*DoS)*, and zero-point energy corrections to the internal energy by employing the 2PT method.[174] Using this method, we found the bulk water entropy to be 62.94 $J.mol^{-1}.K^{-1}$ which is in agreement with results reported in previous studies.[169] The water internal energy inside the BNNTs were calculated using the below equation:

$$\text{Water Energy} = \text{Total System Energy} - \text{Standalone BNNT Energy}, \quad (1)$$

The stand-alone BNNT energy was obtained by employing the LAMMPS-rerun command on trajectory data containing only BNNT atoms (i.e., when all the water molecules were removed).

The hydrogen bonding statistics were obtained by adopting appropriate distance-angle (r, θ) based definitions informed by the corresponding two dimensional potentials of mean force [$W(r,\theta)$]. The parameters r and θ represent the inter-oxygen distance and the angle between the OH bond and the vector joining the oxygen atoms ($\angle HO_dO_a$). For any pair of water molecules, there exists four possible angles meeting the above criteria and only the smallest of these angles was considered for sampling. The 2D PMF is given by the following equation:

$$W(r,\theta) = -kTg(r,\theta), \quad (2)$$

Here, $g(r,\theta)$ is defined to be the ratio between the average number of water-oxygen atoms in a shell between $r+dr$ and r centered around a given water-oxygen atom, with the corresponding $\angle HO_dO_a$ angle between $\theta+d\theta$ and θ, in the presence and absence of intermolecular interactions. The latter is given by $(4\pi r^2\rho dr)(P_{random}(\theta)d\theta)$, where the $P_{random}(\theta)$ represents the random probability distribution of θ for non-interacting water molecules. For bulk water, $P_{random}(\theta)$ is obtained by considering the distribution of θ between water molecules with r > 10 Å. On the other hand, to obtain $P_{random}(\theta)$ for water confined in each BNNT, we performed two additional simulations with only a single water molecule inside the BNNT. For each BNNT, these two simulations started with dissimilar initial configurations, and the water molecule trajectories were superimposed on each other to replicate the behavior of a pair of non-interacting water molecules confined in the BNNT. The $\angle HO_dO_a$ angle sampled from these superimposed trajectories gives the random probability distribution of θ ($P_{random}(\theta)$). Further, to account for the excluded volume effects in a confined system,[175] the non-interacting particle distribution was modified as $(f_c.g_u(r).4\pi r^2\rho dr)(P_{random}(\theta)d\theta)$

for water confined in BNNTs. The uniform profile $g_u(r)$ for a cylindrical confining geometry is given by:[176]

$$g_u(r) = \frac{V_p}{(2\pi)^3} \int d^3Q P_{Cyl}(Q). \quad (3)$$

Here, V_p is the volume and $P_{Cyl}(Q)$ is the form factor[177] of a cylindrical cell with radius R_c and length L, expressed as:

$$P_{Cyl}(Q) = \int_0^1 d\mu \left[j_0\left(\frac{\mu Q L}{2}\right) \right]^2 \left[\frac{2J_1(QR_c\sqrt{1-\mu^2})}{QR_c\sqrt{1-\mu^2}} \right]^2, \quad (4)$$

where J_1 is the first order Bessel function and j_0 is the zero-order spherical Bessel function. The correction parameter f_c accounts for the surface roughness and was adjusted so that the radial distribution function (RDF) between the water oxygen atoms tends towards one for large *r*.

The 2D PMF for bulk water and water confined in (6, 6) BNNT are shown in Fig C9 (see appendix C). From the PMF data, we define a dividing surface surrounding the HB basin centered around a short inter-oxygen distance (r < 3 Å). The dividing HB boundary was chosen to be the zero-PMF equipotential contour (represented by black contour lines in Fig. C9 in appendix C) beyond which the depletion zone can be observed ($g(r,\theta)$ < 1)). For a given system, all the water molecule pairs that lie within this HB basin are considered to be hydrogen bonded.

Polarizability of water inside the BNNTs is an important consideration. The charges on atoms simulated using ReaxFF are not static. In these simulations, a charge equilibration scheme (QEq) is used to predict the environment dependent charge distribution in molecules by equating the electronic chemical potentials of atoms.[173] As a result, polarizability is accounted for by considering the fluctuations in atomic charges which capture the variations in molecular dipole moment induced by variations in molecular geometry and environment.[178,179] However, unlike

other implementations such as the Drude polarizable model,[180] the atomic polarization is not explicitly modeled in the present simulations. Of course, most recent studies attempting to accurately model the water-hBN interfacial interactions have not considered these explicit atomic polarizabilities;[181-183] despite that, these studies have been successful in capturing the wetting properties and the binding energy of water on h-BN. Thus, we expect our results to be of reasonable accuracy and the trends in the calculated thermodynamic quantities to represent reality at least qualitatively.

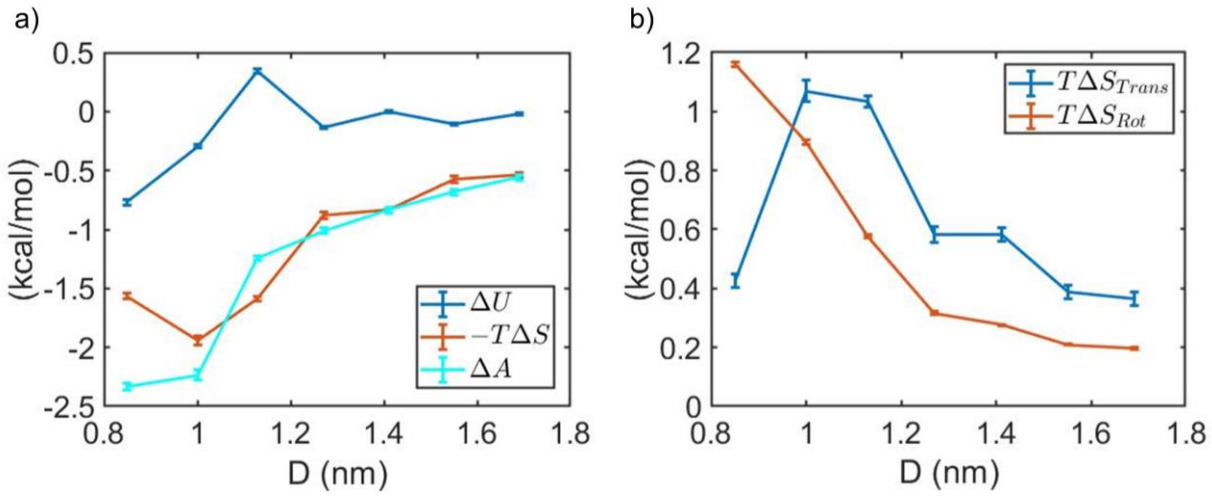

Figure 4.2. a) Changes in the internal energy (ΔU), entropy (−TΔS), and free energy (ΔA) of water confined in BNNTs (these changes are relative to the bulk water) as functions of the BNNT diameters. b) Variation in the translational ($T\Delta S_{Trans}$) and rotational ($T\Delta S_{Rot}$) components of the total entropy change plotted as functions of the BNNT diameters. The error bars represent standard errors.

4.3 Results and Discussions

Figure 4.2(a) shows the free energy change (ΔA) associated with the water confined in BNNTs (relative to the bulk water) and the corresponding entropic (−TΔS) and internal energy (ΔU) contributions to this free energy change ($\Delta A = -T\Delta S + \Delta U$). For all the tube diameters (ranging from 0.85 nm to 1.69 nm), water molecules have lower free energies (i.e., ΔA<0) inside the BNNT as compared to the water molecules present in the bulk. This confirms that the water molecules prefer to remain confined within the BNNT than to remain in the bulk. Along the same lines, we find that greater the degree of confinement (i.e., smaller the BNNT diameter), more negative is ΔA (i.e., ΔA increases monotonically with an increase in the BNNT diameter), confirming a greater preference of the water molecules to be present inside a BNNT with a smaller diameter (or a greater degree of nanoconfinement). Despite such monotonic trend in ΔA with the BNNT diameter, the entropic ($-T\Delta S$) and internal energy (ΔU) contributions to the free energy show a non-monotonic trend with the BNNT diameter. For example, the entropic component ($-T\Delta S$) decreases in magnitude (i.e., becomes less favorable) monotonically with BNNT diameter (D) for D ranging from 1 nm to 1.69 nm. However, it is largest (in magnitude) and hence most favorable for D = 1 nm or (7,7) BNNT and decreases in magnitude (denoting less favorability) for D = 0.85 nm or (6,6) BNNT. The contribution of the internal energy change (ΔU) towards a favorable ΔA, on the other hand, is negligible (tending towards zero) for BNNTs with larger diameter and is favorable for (6,6) BNNT (D=0.85 nm), mildly favorable for (7,7) BNNT (D=1.0 nm), and mildly unfavorable for (8,8) (D=1.13 nm) BNNT. This comparison establishes that the entropic contribution is the dominant factor in stabilizing the water confined in all the BNNTs considered in this study. Of course, the most favorable value of ΔA is noted for (6,6) BNNT (D=0.85 nm), although the entropic contribution is maximum for (7,7) BNNT (D=1.0 nm). This

stems from the fact that ΔU is very much favorable for (6,6) BNNT (D=0.85 nm) [in fact, in the (6,6) BNNT, ΔU is so significant that the entropic contribution ($-T\Delta S$) accounts for only 67% of the corresponding total free energy change (ΔA) relative to bulk water] ensuring the maximum favorability of ΔA for (6,6) BNNT (D=0.85 nm).

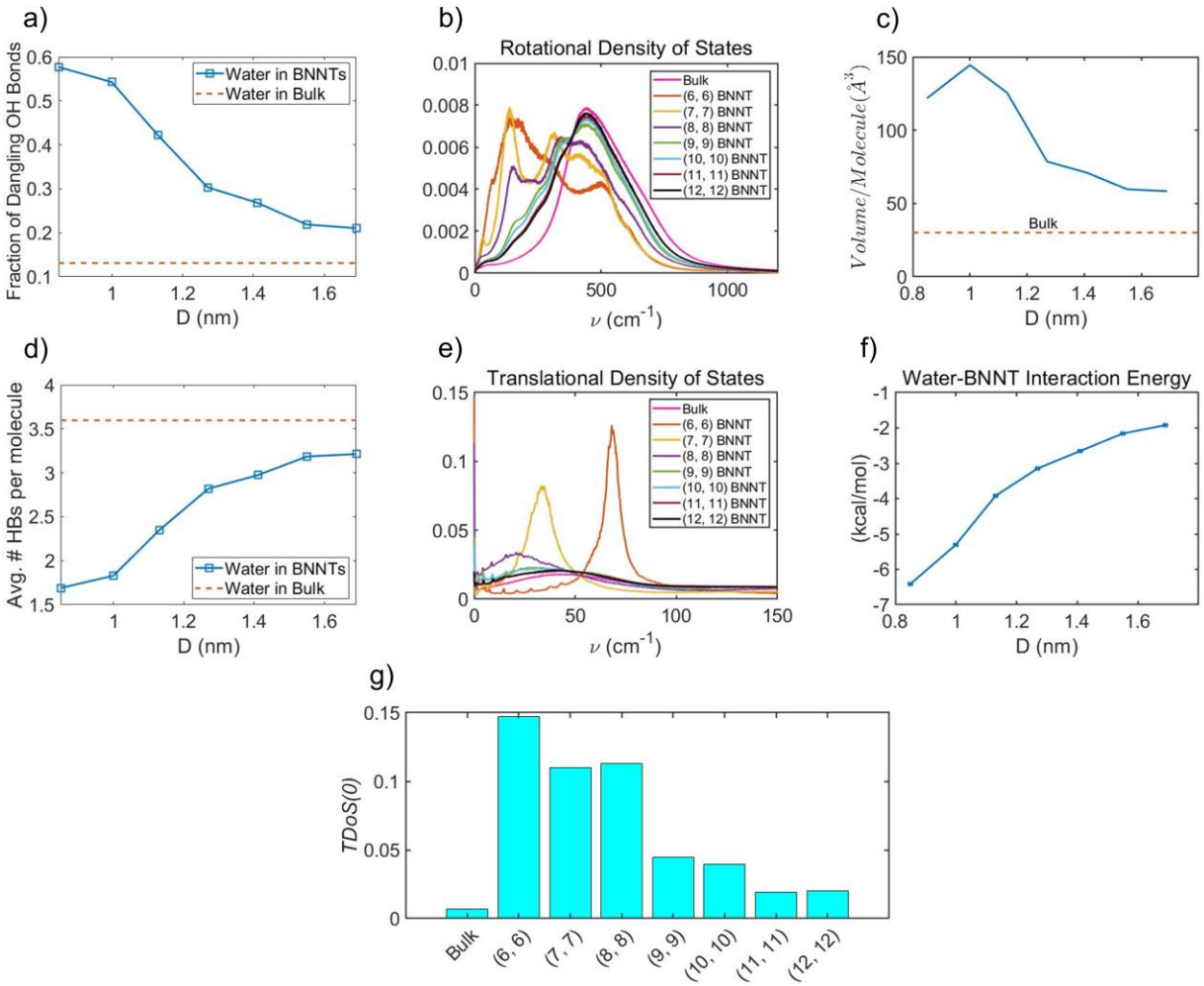

Figure 4.3. a) Variation of the fraction of dangling OH bonds for the water molecules confined in BNNTs (for different values of the BNNT diameters) and the water molecules present in the bulk. b) Variation of the rotational density of states (RDoS) for the water molecules confined in BNNTs (of different diameters) and the water molecules present in the bulk. c) Variation of the specific volume of the water molecules confined in BNNTs (for different values of the BNNT diameters) and the water molecules present in the bulk. d) Variation of the average number of HBs per water molecule for the water molecules confined in BNNTs (for different values of the BNNT diameters)

and the water molecules present in the bulk. e) Variation of the translational density of states (TDoS) for water molecules confined in BNNTs (of different diameters) and the water molecules present in the bulk. f) Variation of the normalized water-BNNT interaction energy for the water molecules confined in BNNTs (for different values of the BNNT diameters). g) Variation of the zero-frequency TDoS [or, TDoS(0)] for water molecules confined in BNNTs (of different diameters) and the water molecules present in the bulk.

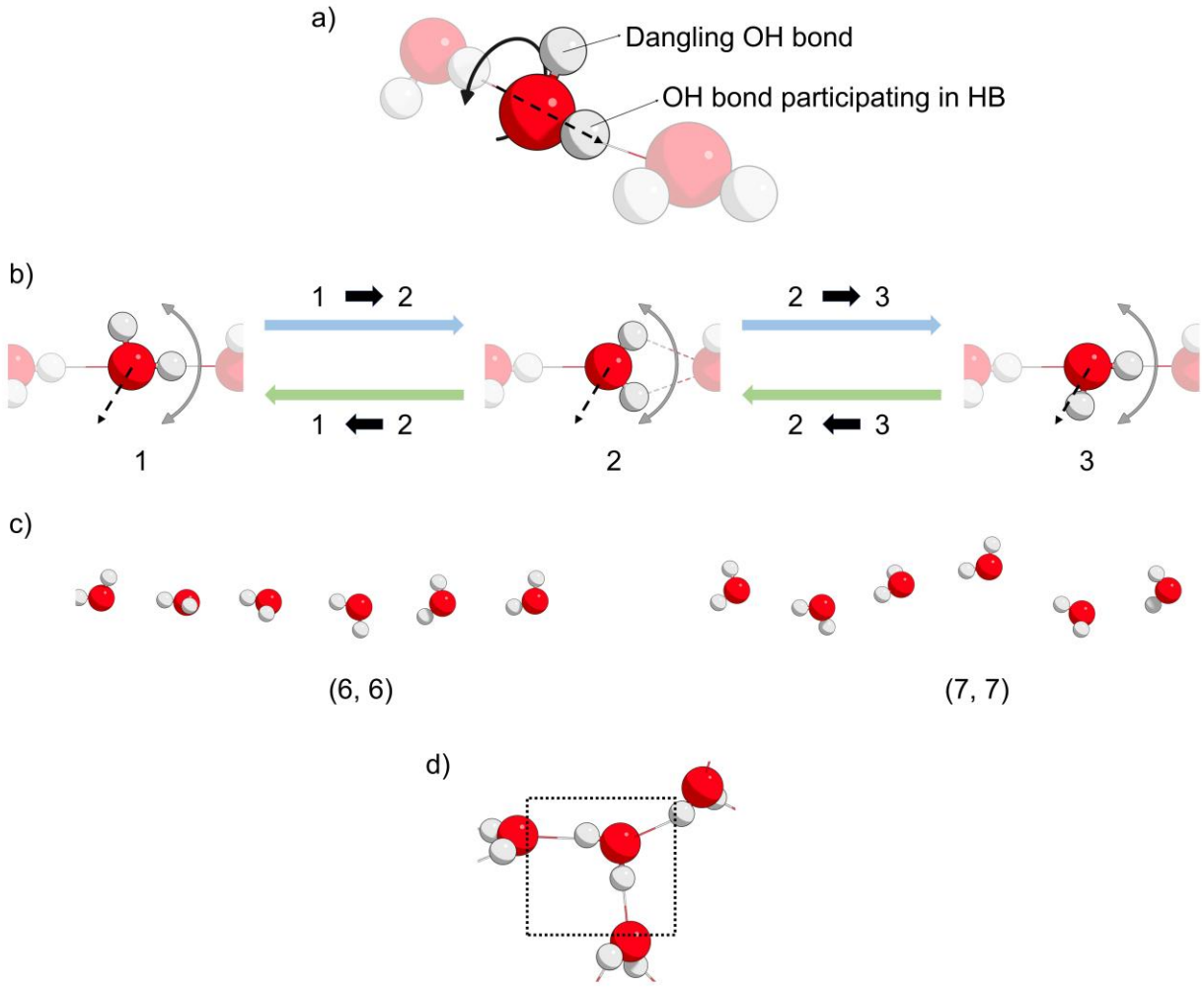

Figure 4.4. Schematics showing a) the rotation of a water molecule, with a dangling OH bond, about the axis (indicated by the straight dashed arrow) parallel to the hydrogen bonding OH bond, and b) flipping of a water molecule, with a dangling OH bond, about the axis perpendicular to the molecular plane (indicated by the straight dashed arrow). Schematic representations of c) single file arrangement of water molecules in (6, 6) and (7, 7) BNNTs and d) restraints imposed on the molecular plane of a water molecule donating both the hydrogens and simultaneously accepting at least one HB.

Given the dominant role of the entropic favorability in dictating the stable (and preferred) configuration of water molecules within the BNNT, we further decompose the total entropic contribution into rotational ($T\Delta S_{Rot}$) and translational components ($T\Delta S_{Trans}$) and study the variation of these components as functions of the BNNT diameters [see Fig. 4.2(b)]. We find that for water confined in the (6, 6) BNNT (D=0.85 nm), the rotational entropy ($T\Delta S_{Rot}$) is the dominant part with a 74% contribution to the total entropic gain. Further, the (6, 6) BNNT system exhibits the largest water rotational entropic gain ($T\Delta S_{Rot}$) among all the BNNT sizes considered in this study; in fact, $T\Delta S_{Rot}$ decreases monotonically (i.e., shows progressively less favorability) with an increase in the BNNT diameter. We attribute this enhanced rotational entropy [for the (6, 6) BNNT] to the large fraction of dangling water OH bonds present in this system [see Fig. 4.3(a)]. Fig. 4.3(a) shows that the fraction of dangling water-OH bonds inside the BNNT is always greater than that in the bulk and this number is maximum for (6,6) BNNT (i.e., BNNT with smallest diameter) and decreases monotonically with an increase in the BNNT diameter: $T\Delta S_{Rot}$ follows the same trend as the dangling OH bond fraction for all the systems considered in this study. Numerous studies[184-186] have shown that near a hBN (hexagonal boron nitride) surface, water molecules favor a one-legged orientation, which characterizes such dangling bonds. In this configuration, one of the OH bonds of an interfacial water molecule points towards the BN surface and such bonds are referred to as dangling OH bonds as they do not participate in hydrogen bonding with the surrounding water molecules [see Fig. 4.1(h) showing the MD simulation snapshot of such a dangling bond in (6,6) BNNT]. Also, in the (6, 6) BNNT (D=0.85 nm), the extreme confinement in the radial direction localizes the water oxygen atoms to the center of the tube [see Fig. 4.1(a, h) and Fig. C2(b) (see appendix C)]. As a result, the OH bonds participating in hydrogen bonding tend to align with the tube axis [see Fig. 4.1(a)] and the dangling hydrogens

remain close to the oxygen atoms of the nearby water molecules [see Fig. C1(a) in appendix C]. In this configuration, a water molecule with a dangling OH bond undergoes rotation primarily via two mechanisms: a) rotation about the OH bond participating in hydrogen bonding[187] [see Fig. 4.4(a) and Fig. C3(a) (in appendix C)] and b) flipping about the axis perpendicular to the plane of the water molecule[188] [see Fig. 4.4(b), Fig. C1(b) and Fig. C3(b)]. The former mechanism is characterized by the dangling OH bonds making rotational sweeps about the hydrogen-bonded OH bond, while the latter mechanism is driven by the two OH bonds swapping their respective positions. Such rotational motions are not prominent for the water molecules in the bulk, where the water molecules form tetrahedral hydrogen bond networks and the fraction of dangling OH bonds is less than 0.15. These findings are evident from the enhancement in the low-frequency rotational modes (in the frequency range of 120-200 cm^{-1}), as indicated by a red shift in the rotational density of states (RDOS) for water molecules in the (6, 6) BNNT as compared to the bulk [see Fig. 4.3(b)]. The presence of such amplified low-frequency rotational modes indicates that relative to the bulk, water (similar to that in vapor phase) undergoes freer rotations in the (6, 6) BNNT.[169]

On the other hand, the translational entropic gain ($T\Delta S_{Trans}$) [see Fig. 4.2(b)] for the BNNT-confined water depends on the density [depicted in Fig. 4.3(c)] and the average number of HBs formed by each water molecule [depicted in Fig. 4.3(d)]. Given the significant radial confinement experienced by the water molecules in the (6, 6) BNNT (D=0.85 nm), low-frequency in-plane oscillations are suppressed and high-frequency rattling motions are enhanced compared to the bulk water: this is evident from a blue shift in the translation density of states (TDoS) [see Fig. 4.3(e)]. As a result, we can infer that for water inside the (6, 6) BNNT, the translational entropic gain is primarily caused by axial diffusion. Figure 4.3(g) shows the zero-frequency TDoS [denoted as

TDoS(0)] for water in all the systems (i.e., BNNTs of all the different diameters) considered in this study. *TDoS(0)* accounts for the contribution from the diffusional motions to the translational entropic component [174] of the water molecules, and is found to be highest for the water molecules in the (6, 6) BNNT. In this (6,6) BNNT, on average, water molecules form less than 1.7 HBs per molecule [see Fig. 4.3(d)] and exist in a straight single file configuration [see Fig. 4.1(a)].

Also, the favorability associated with the internal energy change (ΔU) is the highest for water in the (6, 6) BNNT (D=0.85 nm) [see Fig. 4.2(a)]. This enhanced energetic favorability is due to the fact that in the 0.85 nm wide BNNT the water molecules remain localized at the center of the tube and are in close proximity to all the BN atoms at a given axial location. As a result, these water molecules experience optimal interaction with a larger portion of the BNNT surface, as compared to the water molecules confined in BNNTs with larger diameters: this is established by the fact that the water-BNNT interaction energy is highest for water confined in (6,6) BNNT [see Fig. 4.3(f)]. Also, these results indicate that the large water-BNNT interaction energy triumphs over the energy penalty due to loss of HBs, thereby ensuring a significantly favorable ΔU for water confined in (6,6) BNNT.

In the (7, 7) BNNT (D=1 nm), where water molecules experience the largest entropic gain contributing 87% to the total free energy change [see Fig. 4.2(a)], we see that the translational entropic gain ($T\Delta S_{Trans}$) is larger than the rotational counterpart ($T\Delta S_{Rot}$) [see Fig. 4.2(b)]. Water molecules in the (7, 7) BNNT possess the highest specific volume (lowest density) [see Fig. 4.3(c)] and exist in a single-file chain structure that spans a much wider radial expanse at the nanotube center as compared to the single file chain structure in (6, 6) BBNT [see Figs. 4.1(a,b), Fig. 4.4(c) and Fig. C2(a,b)]. While both the (6, 6) and (7, 7) BNNTs contain single file water, the radial confinement in the (7, 7) BNNT (D=1.0 nm) is weaker in comparison to the (6,6) BNNT (D=0.85

nm) and as a result, the low-frequency in-plane oscillations are more prominent. Therefore, compared to the water molecules in the bulk and the (6, 6) BNNT, we see an enhancement in the low-frequency translational modes for water molecules in (7, 7) BNNT indicated by the redshift in TDoS [see Fig. 4.3(e)]. In addition, the *TDoS(0)* for water in this system is significantly higher as compared to the bulk water [see Fig. 4.3(g)] and this behavior can be attributed to the single-file nature of water causing improved axial diffusion. The high specific volume for water in (7, 7) BNNT is a result of the entropic gain and the aligning tendency of water near the BN surface. In a densely packed configuration, water tends to form well connected HB networks resulting in a smaller dangling OH bond fraction. The sparse packing of water in the (7, 7) BNNT is accompanied by a loss in HBs per molecule. The unfavourability in ΔU (i.e., ΔU becoming positive) ensued by such a loss in HBs is compensated by a significant entropic gain [$-T\Delta S$ has the highest negative value for (7,7) BNNT, see Fig. 4.2(a)] as well as a reduction in internal energy (ΔU) due to the one-legged orientation caused by the favorable interaction between water molecules and the BNNT surface. In this BNNT, while the dangling OH bond fraction is close to that in the (6, 6) BNNT [see Fig. 4.3(a)], we see a noticeable drop in the rotational entropic gain ($T\Delta S_{Rot}$) as compared to the (6, 6) BNNT system [see Fig. 4.2(b)]. As the restriction on the in-plane translational motion of the confined water molecules is less severe in the (7, 7) BNNT (D=1 nm) as compared to the water molecules confined in (6, 6) BNNT (D=0.85 nm), the hydrogen bonding OH bonds do not align with the tube axis [see Fig. 4.1(b) and Fig. 4.4(c)]. At the same time, the dangling hydrogens tend to stay further away from the oxygen atoms of the nearby water molecules in the (7, 7) BNNT [see Fig. 4.4(c) and Fig. C1(a) (in appendix C)]: this is established by the O-H RDF plot [see Fig. C1(a)], as discussed below. The third peak in the O-H RDF plot corresponds to the distance between the oxygen atom of a water molecule and the dangling

hydrogen atom of a neighboring water molecule. We clearly see that the location of this third peak is shifted by 0.17 Å towards the right for water in (7,7) BNNT, when compared to the water confined in (6,6) BNNT. Consequently, the flipping tendency of a water molecule, about the axis perpendicular to the plane of the molecule, is weakened in the (7, 7) BNNT [see Fig. C1(b) (in appendix C)] resulting in a visible drop in the rotational entropic gain ($T\Delta S_{Rot}$) as compared to the water molecules confined in the (6, 6) BNNT. This scenario is confirmed from the suppressed rotational modes in the ν =160-270 cm^{-1} range [see Fig. 4.3(b)] for water in (7, 7) BNNT, as compared to the water molecules confined in the (6,6) BNNT. Also, despite the average number of HBs per molecule being similar in the (6, 6) and (7, 7) BNNT systems [see Fig. 4.3(d)], we see a notable rise in the penalty associated with the internal energy (i.e., ΔU becomes more positive) for the water molecules confined in (7,7) BNNT as compared to the water molecules confined in the (6,6) BNNT [see Fig. 4.2(a)] owing to the weakening of the water-BNNT interaction energy with an increase in the tube diameter [see Fig. 4.3(f)].

In the (8, 8) BNNT (D= 1.13 nm), water forms local high-density cluster-like regions that are bridged by low-density chain-like structures of varying lengths [see Fig. 4.1(c) and Fig. C4 (in appendix C)]. The cluster-like regions are characterized by dense hydrogen bond networks, while the chain-like regions show HB connectivity similar to that of single file (chain-like) water (see Fig. C4 and Fig. C5 in appendix C). In Fig. C5, 0.59 fraction of water molecules form two or less HBs (this is characteristic of single-file or chain-like water), while 0.41 fraction of water molecules form three or more HBs (this is characteristic of water molecules in cluster-like regions forming dense HB networks). As such, the distinct rise in the average number of HBs per molecule in this (8,8) BNNT system, as compared to the (6, 6) and (7, 7) BNNTs [see Fig. 4.3(d)], can be attributed to these local water clusters. The cluster formation is also accompanied by a noticeable drop in the

fraction of the dangling OH bonds [see Fig. 4.3(a)] resulting in a lower rotational entropic gain ($T\Delta S_{Rot}$) [see Fig. 4.2(b)], as compared to the (6, 6) and (7, 7) BNNT systems. Also, as evident from Fig. 4.3(b), the presence of such clusters enhances the high-frequency rotational modes, while the decline in fraction of the dangling OH bonds [see Fig. 4.3(a)] suppresses the low-frequency rotational modes that were found to be dominant in the (6, 6) and (7, 7) BNNTs. On the other hand, the translational entropic gain ($T\Delta S_{Trans}$) for water in the (8, 8) BNNT system is similar to that in the (7, 7) system and accounts for 65% of the total entropic gain [see Fig. 4.2(b)]. Fig. 4.3(e) shows a red shift in the TDoS for water in (8, 8) BNNT, relative to the (7, 7) BNNT system, due to the presence of chain-like regions that experience enhanced in-plane oscillations in the wider (8, 8) BNNT. However, for water molecules confined in the (8,8) BNNT, the presence of the water clusters ensures that the intensities of modes with a frequency larger than 50 cm^{-1} tend towards values similar to that of bulk water. Interestingly, the presence of clusters does not affect the entropic contribution from the diffusional motions with a *TDoS(0)* value similar to the water confined in the (7, 7) BNNT system [see Fig. 4.3(e)]. Finally, among all the BNNTs considered in this study, water has the most unfavorable internal energy in the (8, 8) BNNT: this is corroborated by a positive ΔU associated with the presence of water inside the (8,8) BNNT [see Fig. 4.2(a)]. This distinct rise in the internal energy penalty is due to the combined effect of increased tube diameter which results in a lower water-BNNT interaction energy per molecule [see Fig. 4.3(f)] [as compared to the (7, 7) system, while we do notice an increase in the average number of HBs per molecule from 1.8 to 2.3, see Fig. 4.3(d), the water-BNNT interaction energy drops steeply from -5.3 to -3.9 kcal/mol, see Fig. 4.3(f)] and the presence of chain like regions where the HB network is less dense (see Fig. C4 in appendix C). However, these two aspects also lead to a reduced water density for the water confined in (8,8) BNNT [see Fig. 4.3(c)], which is conducive

to the translational entropic gain in the system [see Fig. 4.2(b)] resulting in a net favorable free energy change [see Fig. 4.2(a)].

In (9, 9) (D =1.27 nm) and (10, 10) (D = 1.41 nm) BNNTs, water molecules exhibit a cage-like structure [see Fig. C2(a) in appendix C] with majority of them forming three or more HBs with the surrounding water molecules. These structures are characterized by a scarce water population near the center of the tube [see Figs. C2(a, b) in appendix C]. Previous studies have shown that water confined in CNTs of similar diameters exhibit ice-like structures with the average number of HBs per molecule exceeding the bulk value.[169] However, we do not observe such structures in BNNTs as evidenced by Fig. 4.3(d), which shows the average number of HBs per molecule is lower in all BNNTs of all diameters, as compared to the bulk. We attribute this behavior to the presence of a significant fraction of dangling OH bonds in all the BNNT systems [see Fig. 4.3(a)]. Specifically, in (9, 9) and (10, 10) BNNTs with cage-like water structures, the energetic penalty due to the loss of HBs, otherwise present in ice-like water, is compensated by the gain in entropy [see Fig. 4.2(a)] and the favorable interaction energy between the BNNT surface and the interfacial water molecules in the one-legged configuration [see Fig. 4.3(f)]. Unlike the hBN-water interface, such a one-legged orientation for water molecules was not found to be favorable at the graphene-water interface.[189] Consequently, the dangling OH bonds can be labelled as *structure breakers* of water confined within the BNNTs.

For water confined in (9, 9) (D =1.27 nm), (10, 10) (D = 1.41 nm), (11, 11) (D = 1.55 nm), and (12, 12) (D = 1.69 nm) BNNTs, the translational entropic change ($T\Delta S_{Trans}$) is the major contributor to the total entropic change, which is favorable for water confined in all these BNNTs [see Figs. 4.2(a,b)]. Such favorable translational entropic contributions can be attributed to the high specific volume [see Fig. 4.3(c)] and lower average number of HBs per molecule [see Fig.

4.3(d)] compared to the bulk water. The translation entropic gain is identical for water in (9, 9) and (10, 10) BNNTs due to the structural similarities of water in these systems [see Figs. 4.1(d, e) and Fig. C2(a, b) in appendix C]. Similar reasoning can be applied to explain the comparable $T\Delta S_{Trans}$ values for water confined in (11, 11) and (12, 12) BNNTs [see Figs. 4.1(f, g) and Fig. C2(a, b) in appendix C].

Further, the variation of the rotational entropic gain ($T\Delta S_{Rot}$) with the BNNT diameters follows the same trend as the fraction of dangling OH bonds for water confined in these BNNTs [compare Figs. 4.2(b) and Fig. 4.3(a)]. This correlation follows from the fact that as the fraction of dangling bonds decrease and falls below 0.5 (for cases of water confined in BNNTs with larger diameters), we see an increase in the proportion of water molecules donating both the hydrogens and simultaneously accepting at least one HB (see Fig. C6 in appendix C). The resulting restrictions on the plane of a water molecule [see Fig. 4.4(d)] tend to prevent free rotations, and the high-frequency rattling motions become dominant, which is evident from the RDoS showing bulk water like behavior for these systems [see Fig. 4.3(b)]. Nevertheless, for all the BNNT sizes considered in this study, we do see a considerably higher dangling OH bond fractions (> 0.2) compared to bulk water (0.13) and as a result the rotational entropic gain ($T\Delta S_{Rot}$) is favorable for water confined in all these BNNTs [see Fig. 4.2(b)].

Finally, the contribution from relative internal energy (ΔU) to the total free energy change (ΔA) is significantly weak (ranging from 15% to 0%) for water confined in these BNNTs. The energetic penalty due to the loss in HBs and the energetic favorability caused by water-BNNT interaction tend to balance each other in these systems and result in the relative internal energy contributions to remain small.

4.4 Conclusion

In summary, we employ ReaxFF based MD simulations to unravel that highly favorable entropic effects drive the filling of mildly hydrophilic BNNTs having diameters ranging from 0.85 nm to 1.69 nm and water is more stable inside BNNTs of all these diameters as compared to water in the bulk. Such a non-intuitive favorable role of entropy, given the conventional wisdom that confinement leads to entropic unfavourability, has been earlier demonstrated during the water filling of CNTs.[169] However, we show that the factors that drive the favorable entropy-driven water filling of BNNTs are significantly different from that of the CNTs. These factors range from the predominance of dangling water-OH bonds leading to a dominance of the rotational entropic effects for the BNNTs with extreme confinement (D = 0.85 nm) to the dominance of the translational entropic effects associated with the presence of single-file water structures or chain-like water regions and/or high specific water-volume for larger BNNTs. We anticipate that our findings will lay the groundwork for developing applications such as filtration, desalination, and energy storage and conversion using interactions of water with nanomaterials such as BNNTs.

Chapter 5: Hydrogen Bond Strength and Kinetics of Nanoconfined Water in Boron Nitride Nanotubes

5.1 Introduction

Water structure in presence of strong (few nanometers or sub-nanometers) confinement has been extensively studied,[190-197] owing to some of the most fascinating effects demonstrated by water in such confinements, including ultra-fast transport,[155-158] spontaneous filling of hydrophobic nanotubes,[168] phase transition under most unexpected conditions,[198] hybrid materials,[167] significant changes in properties such as melting point, boiling point, density, and surface tension,[199] etc. Non-bonded water-water interactions, such as water-water hydrogen bonding, is an important factor governing water behavior in such extreme confinements.[200-202] For example, hydrogen bonding has been known to dictate the nature of water diffusion inside CNTs of varying diameter,[203-205] graphene nanochannels of different nanochannel heights,[206, 207] and self-assembled ionic liquid crystal[208] unidirectional proton transport in fluorinated CNTs,[209] etc. Water-water HBs trigger water clusters inside a confinement: such clusters get broken in contact with certain types of nanoconfinement material (e.g., nanomaterial composed of fluorous compounds) resulting in very fast water transport in such nanoconfinement.[150] In our recent study, we established that such disruption of the hydrogen bond (HB) formation associated with the presence of dangling -OH bonds lead to the spontaneous filling of boron nitride nanotubes (BNNTs) of sub-nanometric diameters.[210]

While the importance of water-water hydrogen bonding inside strong confinements has been thoroughly established, there remains several gaps in understanding the very nature of such HBs inside confinement. For example, the manner in which the progressive increase in the extent of confinement leads to the alterations of the conditions that define the formation of water-water

HBs and the corresponding energetics of such hydrogen bonding, the confinement-driven changes of the *kinetics* of hydrogen bonding (e.g., how stable is a hydrogen bond or once a HB is broken how quickly it re-forms), etc. have not been extensively explored. In this chapter, we address these issues considering water confined inside BNNTs of varying diameters. In our previous study, we have delineated in great details the manner in which BNNTs of different diameters lead to entropy-driven water filling of BNNTs, with the factors dictating the favorable entropy changes and the corresponding water structure, being strongly dictated by the BNNT diameters.[210] In this chapter, we shall study the properties of the HBs inside such BNNTs of various diameters with these properties being entirely governed by the corresponding BNNT-diameter-specific water structures. Specifically, our results demonstrate that depending on the confinement, the characteristics of the PMFs (potential of mean forces) dictating the water-water HBs significantly changes. These PMFs are plotted as functions of r and θ, where r denotes the inter-oxygen distance or the distance between the oxygen atoms of the two water molecules participating in the hydrogen bonding and θ denotes the angle between the OH bond and the line joining the oxygen atoms. We observe completely isolated HB basins in BNNTs with strong confinement, which is in stark contrast to the HBs in bulk or larger diameter BNNTs where there is a second nearby PMF well to which the HB basin is connected *via* a saddle point. At the same time, we obtain most remarkable BNNT-diameter-dependent kinetics of the HBs. The specific single-file water structure inside sub-nanometer-diameter BNNT ensures that the hydrogen bonds formed inside such BNNTs are stable over a much longer time period, as confirmed by the corresponding auto-correlation function, dictating the lifetime of the HBs, decaying to a large non-zero constant value at long times. Similarly, the same water structure ensures that such HBs, once broken, show a strong tendency to re-form. These are highly generic and unprecedented information on the behavior of the HBs as

functions of the nano and sub-nanoconfinement, which motivate the need for a deeper investigation on the *nature and properties* of HBs inside nanomaterial-based confinements.

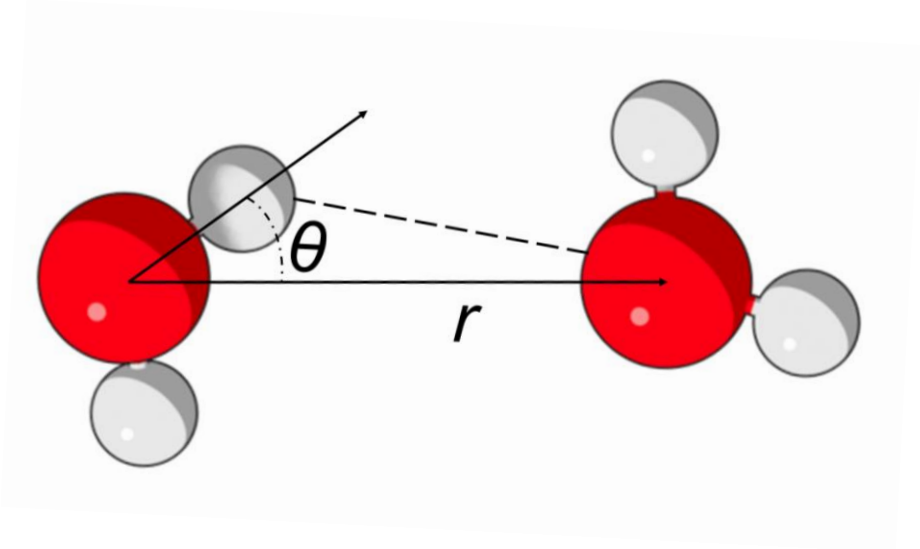

Figure 5.1. Graphical representation of r and θ coordinates used to describe the hydrogen bonding configuration between a pair of water molecules.

5.2 Results and Discussions

To study the hydrogen bonding thermodynamics for water confined in boron nitride nanotubes (BNNTs), we performed the ReaxFF MD simulations of water confined in five different BNNTs with chiral indices (6, 6), (7, 7), (8, 8), (10, 10), and (12, 12) respectively. The diameters of these BNNTs range from 0.85 nm to 1.69 nm with the (6, 6) BNNT having the smallest diameter and the (12, 12) BNNT having the largest. In addition, we also carried out bulk water simulations so as to highlight the effect of BNNT-based confinement on water hydrogen bonding relative to bulk water. First, in order to identify hydrogen bonding configurations between pairs of water molecules, we need to device appropriate HB definitions for the various systems considered in this study. The generic geometry-based HB definition for water involves cutoff values for the inter-

oxygen distance (r), and the angle (θ) between the OH bond and the line joining the oxygen atoms[211-213] (figure. 5.1). The most widely used criterion for bulk water is $r < 3.5$ Å and $\theta < 30°$.[212-214] However, these specific cutoff values and the resulting rectangular boundary, located on the 2D PMF ($W(r,\theta)$) mapped using (r, θ) coordinates, may not be appropriate for identifying HB configurations among water molecules present in non-bulk-like environments. In particular, for water inside the sub-nanometer and nanometer wide nanotubes, the shape and size of the PMF basin corresponding to the HB configurations can differ significantly from that of the bulk water. Figure. 5.2 shows the 2D PMFs ($W(r,\theta)$) corresponding to water-water HB basins for all the systems considered in this study. From these results, we can easily identify the above-discussed differences between bulk water, and water confined in BNNTs of various diameters. To be specific, we see a striking contrast between the PMFs of bulk water and water confined in (6, 6) and (7, 7) BNNTs (with diameters of 0.85 nm and 1 nm, respectively). For water present in these extreme confinements, we see completely isolated HB basins unlike in bulk water, where the HB basin is connected to a nearby PMF well, which is centered around larger r and θ values and correspond to the second hydration shell, via a saddle point. In our previous study,[210] we identified that water takes an axially ordered single-file structure in (6, 6) and (7, 7) BNNTs. As a result, in these extreme confinements, a given water molecule is well separated from other water molecules that are not its nearest neighbors (i.e., not part of its first solvation shell) and the inter-oxygen distances corresponding to the second solvation shell in bulk water are not accessible to pairs of water molecules in these single-file structures (see figure. 5.3). In the (8, 8) BNNT, as the nanotube diameter increases, the ordered single-file structure disappears and we start to see high-density clusters of water molecules joined by low-density chain-like regions. This water structure results in the appearance of the second hydration PMF-well situated close to the HB basin (see figure.

5.2). Similarly, with further weakening of confinement in (10, 10) and (12, 12) BNNTs, the PMF maps approach the behavior similar to the water molecules in the bulk and accordingly, the HB basin gets separated from the nearby well by a saddle region (see figure. 5.2).

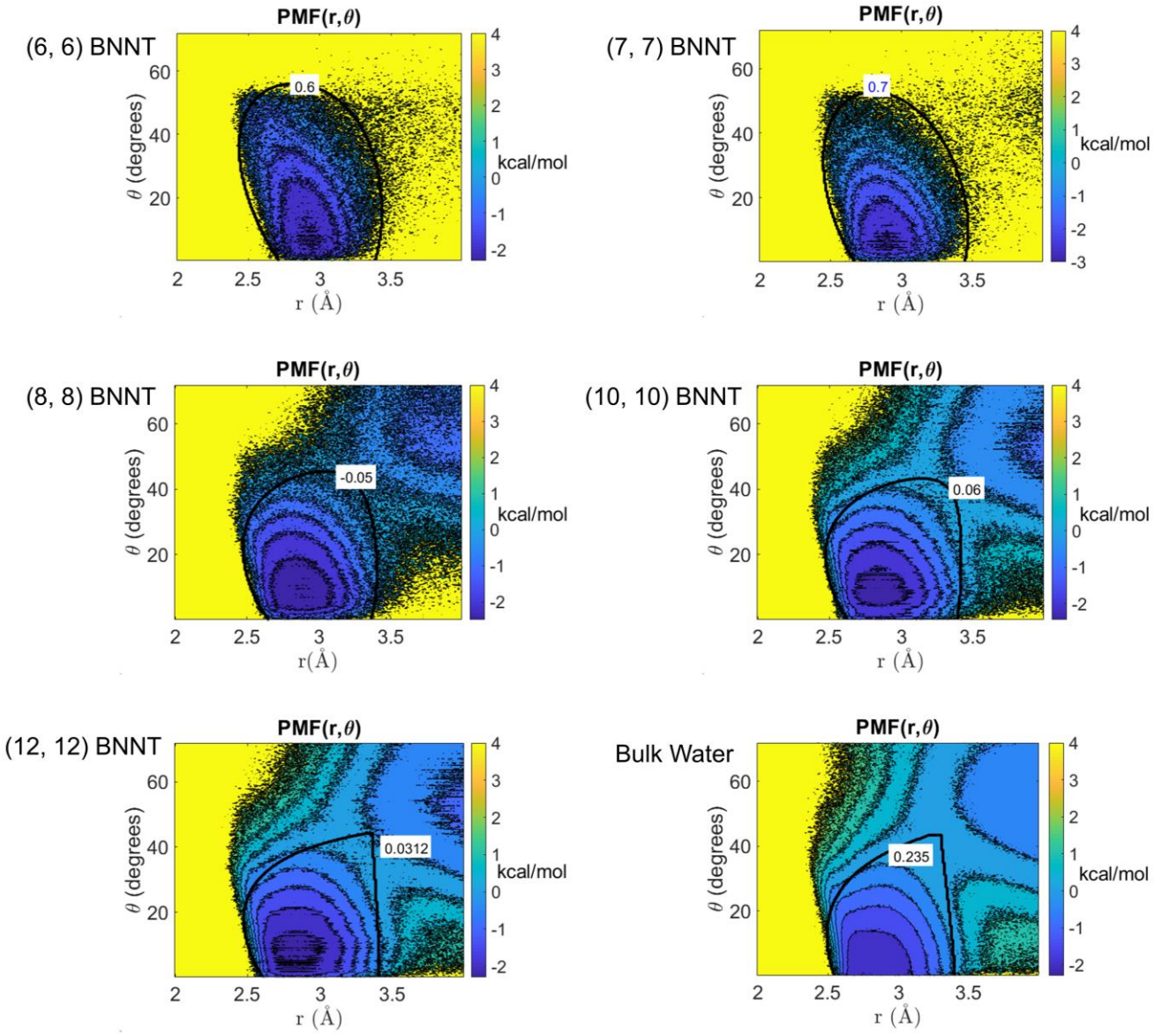

Figure 5.2. Two dimensional potentials of mean force (2D PMF) as functions of r and θ for water molecules in BNNTs with chiral indices (6, 6), (7, 7), (8, 8), (10, 10) and (12, 12) as well as for water molecules in the bulk. Bhargav: The continuous black contour line and the adjacent label in each figure indicate the boundary separating the hydrogen bond basin and the corresponding PMF value at this boundary line respectively.

From the 2D PMF data shown in figure. 5.2, we have determined the appropriate water HB definitions for all the systems considered in this study by choosing a continuous iso-surface with a PMF value beyond which the volume enclosed by the iso-surface increases discontinuously (please refer to the methods section for details). The iso-surface corresponding to the HB definition for each system can be found in figure. 5.2. Using these definitions, we have computed the average number of HBs formed by a water molecule (N_{HB}) in each system (see Table. 5.1). For bulk water, our findings show the N_{HB} to be 3.62, which is close to the values reported in previous studies following similar approaches to develop HB definitions. Inside the BNNT, N_{HB} decreases significantly: smaller the BNNT diameter more prominent is this decrease. For single file water [in (6, 6) and (7, 7) BNNTs], we see N_{HB} values lower than 2 indicating that each water molecule is connected to less than or equal to two adjacent water molecules in the single file structure. Such a behavior stems from the water molecules taking an axially ordered single-file structure in (6, 6) and (7, 7) BNNTs causing the water molecules to be well separated from other water molecules that are not their nearest neighbors (see figure. 5.3). On the other hand, for water confined in wider BNNTs [i.e., in (10, 10) and (12, 12) BNNTs], we see N_{HB} values greater than 3 as a significant fraction of water molecules form three or more HBs with surrounding water molecules in these systems.

System	N_{HB}
Bulk water	3.62
(6, 6)	1.74
(7, 7)	1.88
(8, 8)	2.35
(10, 10)	3.04
(12, 12)	3.29

Table 5.1. Average number of hydrogen bonds formed by each molecule in all the systems considered in this study.

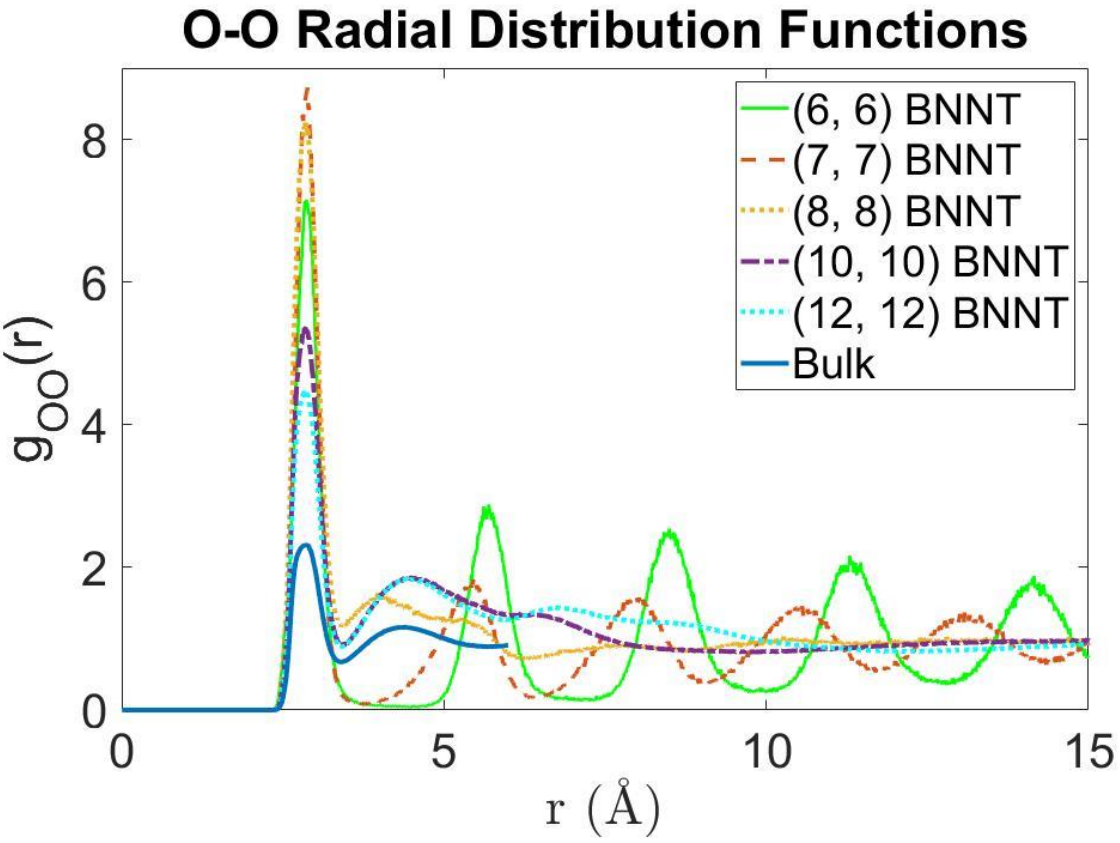

Figure 5.3. Radial distribution functions between oxygen atoms for water molecules in the bulk and in BNNTs with chiral indices (6, 6), (7, 7), (8, 8), (10, 10) and (12, 12).

Further, we have explored the HB kinetics for confined and bulk water modeled in this study using a chemical dynamics-based analysis.[212] In this process, we first compute the HB autocorrelation function (*C(t)*) using a HB population operator *h(t)* which equals 1 if a HB is present between a given pair of water molecules and 0 otherwise. As such, the HB autocorrelation function is given by

$$C(t) = \frac{\langle h(t)h(0)\rangle}{\langle h(0)\rangle}. \quad (1)$$

This function gives the conditional probability that a pair of water molecules are hydrogen bonded at time *t*, given that there exists a HB between this pair at time zero.[212] As shown in figure. 5.4(a), C(t) decays the fastest towards zero for bulk water and the rate of decay generally decreases with an increase in the degree of confinement (i.e., as the BNNT diameter decreases) except for (6, 6) BNNT. However, unlike other systems, C(t) for the water molecules confined in (6, 6) and (7, 7) BNNTs tend to decay towards a finite value below 0.5. In these extreme confinements, where water takes a single-file structure with N_{HB} close to 2, a given water molecule is restricted to forming HBs with the same two neighboring water molecules for the entire duration of the simulations. As a result, if a pair of water molecules are found to form a HB through one of the four hydrogen atoms at *t*=0, the probability of finding the same HB at t=∞ would be approximately 0.25 (one of four possible HBs).

Figure 5.4(b) shows the time dependent conditional probability $[n(t)]$ that an initially hydrogen bonded pair of water molecules stay within the HB vicinity with the initial bond broken. $n(t)$ can be expressed as:

$$n(t) = \frac{\langle H(t)[1-h(t)]h(0)\rangle}{\langle h(0)\rangle}. \quad (2)$$

Here, H(t) equals 1 if the tagged pair of molecules are separated by a distance within the HB vicinity and 0 otherwise. In a given system, a pair of water molecules are considered to be in HB vicinity if their inter-oxygen distance is less than the maximum value of *r* that lies on the HB boundary.

For single file water, in (6, 6) and (7, 7) BNNTs, n(t) relaxes toward a value larger than 0.5 following the same reasoning as described in the above paragraph. Whereas in other systems, n(t) increases at shorter times and then relaxes towards zero at longer times. This behavior indicates that, in these systems, once a HB breaks between a pair of molecules, the water molecules either relax back toward forming the same HB or diffuse away from each other.[212] Here, the latter seems to be the case as evident from figure 5.4(c) which shows the time dependence of C(t)+n(t). Here, C(t)+n(t) gives the time dependent conditional probability that a pair of initially hydrogen bonded water molecules stay within the HB vicinity. For systems where water molecules *do not* form a single-file structure [i.e., in bulk and in (8, 8), (10, 10) and (12, 12) BNNTs], C(t)+n(t) rapidly decays towards zero indicating that as time progresses, pairs of water molecules diffuse away from each other after a HB is broken. In contrast, for single file water, i.e., for water confined in (6, 6) and (7, 7) BNNTs, C(t)+n(t) decays toward values near 0.9 due to the fact that nearly every pair of adjacent water molecules stay within the HB vicinity forming one of four possible HBs.

Further, in order to obtain the forward rate constant (*k*) of HB breaking and the backward rate constant (*k'*) of HB formation, we computed the reactive flux HB correlation function *K(t)* given by

$$K(t) = \frac{-dC(t)}{dt} \tag{3}$$

K(t) can be related to C(t) and n(t) via the following relation

$$K(t) = kC(t) - k'n(t) \quad (4)$$

Here, we used the C(t), n(t) and *K(t)* data for 1ps < t <20ps to compute *k* and *k'*.

From the above relations, the HB lifetime can be obtained using

$$\tau_{HB} = \frac{1}{k} \quad (5)$$

Assuming that hydrogen bond breakage can be described as an Eyring process,[215] we can relate the Gibbs free energy of HB breaking to τ_{HB} using the following equation

$$\tau_{HB} = \frac{h}{k_B T} \exp\left(\frac{\Delta G}{k_B T}\right) \quad (6)$$

Here, h is the planks constant, k_B is the Boltzmann constant and T is the temperature.

Table 5.2 shows the HB lifetimes (τ_{HB}) and ΔG for water in all the systems modeled in this work. We see that bulk water has the smallest ΔG followed by water confined in (6, 6) BNNT. For other confined systems, ΔG is inversely proportional to the nanotube diameter with water in the (7, 7) BNNT exhibiting the largest ΔG.

Our previous study[210] shows that, in the (6, 6) BNNT, water molecules have low translational entropy due to extreme radial confinement restricting in-plane translational motions. However, in the (6, 6) BNNT, water molecules possess high rotational entropy, which is due to the flipping rotations of water molecules in this system and such water flipping involves regular HB breakage. Thus, the small ΔG for water in the (6, 6) BNNTs is favored by rotational entropic gain.

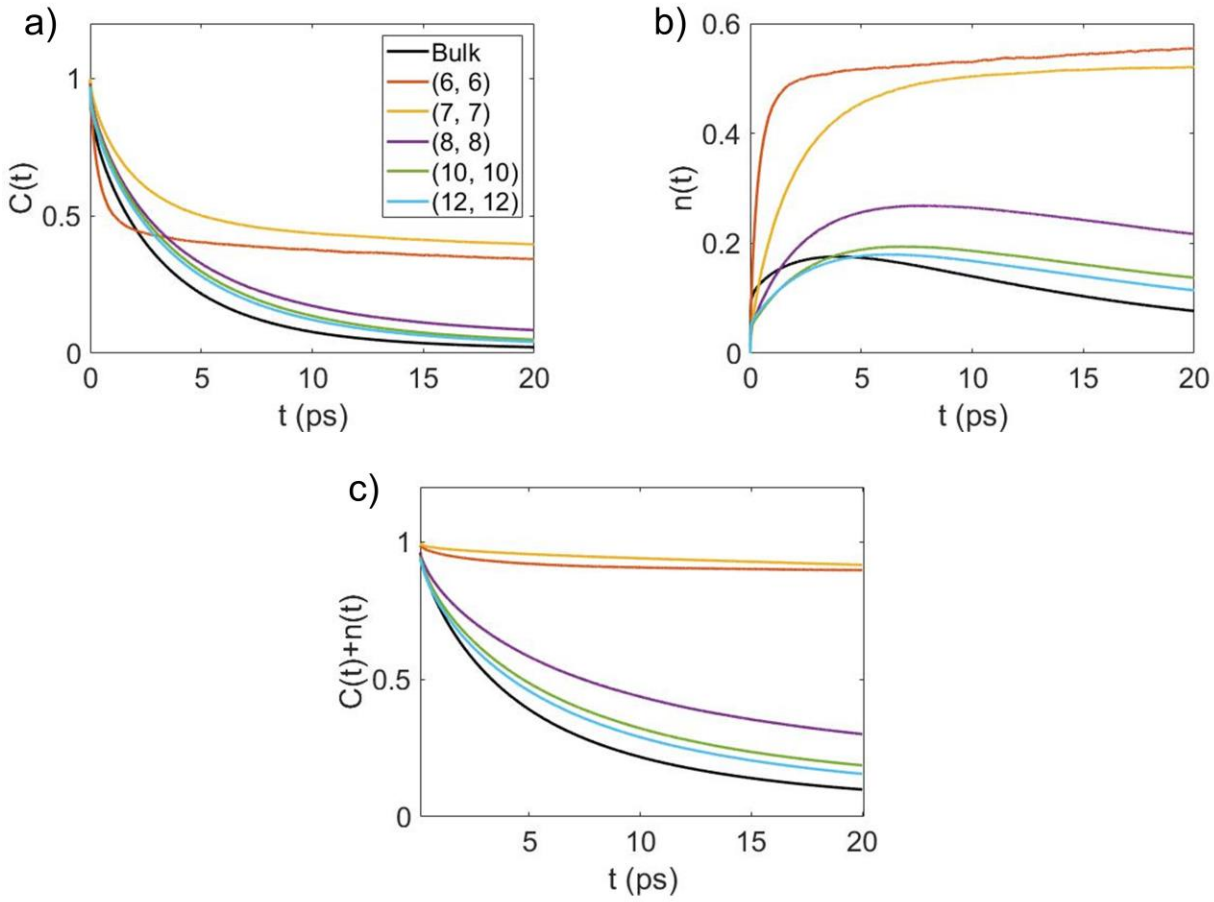

Figure 5.4. a) HB autocorrelation function (C(t)), b) time dependent conditional probability for a pair of initially hydrogen bonded water molecules to be within the HB vicinity but with the initial bond broken (n(t)), and c) the sum of C(t) and n(t) for water molecules in the bulk and in the confined systems considered in this study.

System	ΔG (kcal/mol)	τ_{HB} (ps)
Bulk water	1.8142	3.3550
(6, 6)	1.8999	3.8735
(7, 7)	2.0129	4.6815
(8, 8)	1.9629	4.3051
(10, 10)	1.9483	4.2011
(12, 12)	1.9277	4.0587

Table 5.2. HB lifetimes (τ_{HB}) and Gibbs free energy of HB breaking (ΔG) for water in all the systems considered in this work.

5.3 Conclusion

In summary, we use ReaxFF MD simulations to study the effect of BNNT induced confinement on water hydrogen bond kinetics and strength by obtaining appropriate HB definitions from the 2D PMF maps for each system. We see that in very narrow BNNTs (with sub-nanometric diameter), we observe completely isolated HB basins unlike in bulk water, where the HB basin is connected to a nearby PMF-well via a saddle point. Also, subtle changes in water structure between (6, 6) and (7, 7) BNNTs result in significant differences in water HB strengths with the water confined in a (6, 6) and (7, 7) BNNTs showing the weakest and strongest HBs respectively, among confined systems.

5.4 Methods

All the simulations are performed using the ReaxFF[170] package implemented in LAMMPS MD engine.[84, 171] The ReaxFF force field parameters were obtained from.[24] The production data was obtained from simulating bulk water and confined water (in approximately 10nm long BNNTs) in the canonical ensemble (NVT). The temperature was maintained at 300 K using Nosé Hoover thermostat[85, 86] with a damping constant of 100 time-steps and a time step of 0.25 fs was used for all the simulations. More details regarding the simulation procedure such as the equilibration process, bulk water simulations and obtaining appropriate confined water densities can be found in our previous study.[210]

We obtained the hydrogen bonding definitions based on the distance-angle (r, θ) coordinates using the corresponding two dimensional potentials of mean force [$W(r,\theta)$]. Here, r and θ represent the inter-oxygen distance and the angle between the OH bond and the vector joining the oxygen atoms ($\angle HO_dO_a$) (figure 5.1). Only the smallest θ among the four possible values, for a given pair of water molecules, was considered for sampling. $W(r,\theta)$ is given by the following equation:

$$W(r,\theta) = -k_B T g(r,\theta)\,, \tag{7}$$

Here, $g(r,\theta)$ is given by the ratio between the average number of water-oxygen atoms in a shell between $r+dr$ and r centered around a given water-oxygen atom, with the corresponding $\angle HO_dO_a$ angle between $\theta+d\theta$ and θ, in the presence and absence of intermolecular interactions. The latter can be obtained using $(4\pi r^2 \rho dr)(P_{random}(\theta)d\theta)$, where the $P_{random}(\theta)$ represents the random probability distribution of θ for non-interacting water molecules. $P_{random}(\theta)$ for the bulk water is calculated using the distribution of θ between water molecules with $r > 10$ Å. Whereas, $P_{random}(\theta)$ for confined water (in each BNNT), was obtained by performing two additional simulations with

only a single water molecule inside the BNNT. We started these two simulations with different initial configurations, and the θ distribution for a pair of non-interacting confined water molecules was obtained by superimposing these water molecule trajectories on each other.[210] The random probability distribution of θ ($P_{random(\theta)}$) was given by the $\angle HO_dO_a$ values sampled from these superimposed trajectories. In addition, the non-interacting particle distribution was modified as $(f_c.g_u(r).4\pi r^2\rho dr)(P_{random(\theta)}d\theta)$, for confined water in BNNTs, to take the excluded volume effects into consideration in a confined system.[174] Here, $g_u(r)$ the uniform profile for a cylindrical confining geometry is given by:[175]

$$g_u(r) = \frac{V_p}{(2\pi)^3}\int d^3Q P_{Cyl}(Q), \tag{8}$$

where, V_p is the volume and $P_{Cyl}(Q)$ is the form factor[176] of a cylindrical cell with radius R_c and length L, which is given by:

$$P_{Cyl}(Q) = \int_0^1 d\mu \left[j_0\left(\frac{\mu QL}{2}\right)\right]^2 \left[\frac{2J_1(QR_c\sqrt{1-\mu^2})}{QR_c\sqrt{1-\mu^2}}\right]^2. \tag{9}$$

Here, J_1 is the first order Bessel function and j_0 is the zero-order spherical Bessel function. The correction parameter f_c accounts for the surface roughness and was adjusted so that the radial distribution function (RDF) between the water oxygen atoms tends towards one for large r.

In figure. 5.2, we show the 2D PMF for water in all the systems considered in this study. The HB diving boundary was obtained by considering the iso-surface with a PMF valued beyond which the volume enclosed by such surface increases discontinuously. The HB boundary for each system is shown using a continuous black contour line in figure. 5.2.

Chapter 6: Conclusions and Future Scope

6.1 Conclusions

This thesis employs all-atom MD simulations to probe the structure, properties, and thermodynamics of water and ions confined within a hydrophilic nanotube (BNNT) of nanometric and sub-nanometric radii. The results, elucidated in four separate chapters, bring out the effect that extremely strong confinement can have on ion/water structure and mobility, and water thermodynamics and hydrogen bonding characteristics.

First (in chapter 2), we unravel the unique endohedral and non-covalent nanotube-water-electrolyte hybrid structure that develops when an electrolyte solution containing a large concentration of salt with a large anion (e.g., LiTFSI salt) is forced into a BNNT of 1 nm diameter. This hybrid structure is characterized by the presence of the repeating and axially separated non-overlapping blocks of the TFSI anion and the Li-ion-solvated water molecules. We confirm the highly stable nature of this hybrid by separate free energy calculations; this stable nature leads to (a) the TFSI anions being present in a highly trapped immobile state, (b) water molecules being present in a zero-dimensional liquid state, and (c) the hybrid showing very little structural changes even after being subjected large temperature changes or changes in the salt concentration of the surrounding medium.

Second (in chapter 3), we study the response of this hybrid when subjected to an electrostatic potential difference. The presence of the non-overlapping and immobile blocks of water molecules (solvating the highly mobile Li-ion) and TFSI anion, coupled with the TFSI anion's greater tendency to enter an empty 1-nm-wide BNNT before hydrated Li^+ ion, eventually leads to the fascinating situation where there is the water-free localization of the TFSI anion near

the negative electrode. WISE systems, with a very large concentration of the electrolyte salt (e.g., LiTFSI), has been specifically designed to ensure such water-free localization of the anion at the negative electrode. In this work, we show that the periodic and immobile structuring of the Li-ion-solvating water molecules and TFSI anions ensures that such localization is possible at a much smaller concertation of the LiTFSI salt.

Third (in chapter 4), we study the thermodynamics of water filling BNNTs of different diameters. We find that the favorable entropy changes promote the filling of the BNNTs. This is highly counter-intuitive, stemming from the fact that encapsulation of water molecules in confinement is expected to lead to loss in the degrees of freedom of the water molecules making the process entropically unfavorable. However, in the present case, entropy becomes the driving factor: of course, the type of the favorable entropy depends on the exact diameter of the BNNT. For BNNTs of very small diameters (< 1nm), the favorable rotational entropic component, stemming from the presence of the dangling water OH bonds that do not participate in hydrogen bonding, promotes the filling process. On the other hand, for 1-nm BNNT, the translational entropic component dominates driven by the enhanced in-plane motion of the water molecules present in a single-file structure and spanning a significant radial expanse inside the BNNT. Finally, for BNNTs with larger diameters, the favorable translational entropic component associated with either the presence of chain-like water regions inside the BNNT or the presence of a high specific water volume and reduced number of HBs per molecule ensure the preferable water filling of the BNNTs.

Fourth (in chapter 5), we study the hydrogen bonding between water molecules confined in such BNNTs and explain the effect of the specifics of the water structures, as a function of the BNNT diameter, in deciding the energetics and kinetics of such water-water HBs. For example, in very

narrow BNNT (with sub-nanometric diameter), we observe completely isolated HB basins unlike in bulk water, where the HB basin is connected to a nearby PMF well via a saddle point. Also, subtle changes in water structure between (6, 6) and (7, 7) BNNTs result in significant differences in water HB strengths with the water confined in a (6, 6) and (7, 7) BNNTs showing the weakest and strongest HBs respectively, among confined systems.

6.2 Future Scope

This dissertation attempts to shed light on the behavior and properties of water molecules and ions inside a well-known nanomaterial, namely BNNT. Such understanding is critical for promoting the usage of non-carbon-based nanomaterial.

As immediate future problems, the computational framework established in different chapters of this dissertation can be leveraged for studying (1) the BNNT filling thermodynamics and the resulting water structure and hydrogen bonding for electrolyte solutions containing salts of ions of different valences and sizes; (2) electrohydrodynamic liquid transport inside BNNTs of different diameters; (3) formation of different types of nano-hybrids for cases where water is mixed with salts of different charges and sizes of cations and anions; (4) effect of electric fields, temperature gradients, and other perturbations on such nano-hybrids and the mechanisms in which such perturbations can be utilized for various applications.

As long-term future problems, the framework proposed in this dissertation can be extended to analyze the behavior of water and ions inside other non-carbon-based materials. For example, the analysis proposed in chapters 4 and 5 can be utilized to understand the filling, structure, and properties of water inside MXene nanochannels and nano-membranes.[216-220] Recent studies have

focused on interesting behavior and properties of water inside MXene nanochannels;[216-219] however, analysis focusing on the thermodynamics and kinetics of water behavior inside such nanochannels remain less studied. Water behavior inside other kinds of nanomaterial-based nanoconfinements that will be benefitted by such analysis include nanochannels and nanopores composed of MoS_2,[221, 222] WS_2,[223] etc. Like the properties and structures of the water molecules in such nanoconfinements, equally interesting will be elucidating the effect of large-concentration of salts of ions of different sizes and valences in water behavior (e.g., in the formation of water-salt-nanomaterial-based nanohybrid and the stability of such nano-hybrids) in strong nanoconfinements fabricated with such novel nanomaterials. Finally, our analysis method will be useful for understanding the interactions of hydrated and charged biomaterials (e.g., charged and counterion-screened DNA molecules in water solution) with such nanomaterials: for example, our simulations will provide the framework for developing simulations towards understanding the dynamics of a DNA molecules through a nanopore of such nanomaterials for sensing and sequencing,[224-227] developing nanomaterial based nano-carrier for the delivery of therapeutic proteins,[228] fabricating MXene/Protein based nanocomposites for biomedical applications,[229] developing biological cell-laden MXene nanocomposite based bio-inks,[230] etc.

The application space of water-non-carbon-based-nanomaterial interactions is ever expanding; from energy solutions, water treatment, and healthcare to flexible electronics and sensors, water-nanomaterial interactions are becoming ubiquitous. Under such circumstances, this dissertation provides an important foundation for advancing our understanding of interactions of ions and water with very well-known, but much less studied nanomaterial, namely BNNT, and in the process, promises to develop strategies for understanding water and ion interactions with other nanomaterials, such as MXene, MoS_2, WS_2, and many more.

Appendix A

Supporting information for chapter 2 is presented here.

A1. Nonbonded Potentials and Corresponding Parameters

The 12-6 Lennard-Jones interaction energy is expressed as:

$$U_{LJ} = 4\varepsilon_{ij}\left[\left(\frac{\sigma_{ij}}{r_{ij}}\right)^{12} - \left(\frac{\sigma_{ij}}{r_{ij}}\right)^{6}\right], \text{(A1)}$$

and the Coulombic interaction energy is given by:

$$U_{Coulombic} = \frac{q_i q_j}{4\pi\varepsilon_0 r_{ij}}. \text{(A2)}$$

In equations A1 and A2, ε_{ij} is the depth of the LJ potential, σ_{ij} is the interatomic distance at which the LJ interaction energy between atoms i and j is zero, q_i and q_j are the charges of atoms i and j, r_{ij} is the interatomic distance between atoms i and j, and ε_0 is the permittivity of vacuum. The values of the nonbonded interaction parameters for all the atom types are provided in Table A1.

Atom	σ (Å)	ε (Kcal/mol)	Charge (e)
Li	2.12645	0.01828	1.0000
N_{TFSI}	3.25000	0.17000	-0.6600
S_{TFSI}	3.55000	0.25000	1.0200
O_{TFSI}	2.96000	0.21000	-0.5300
C_{TFSI}	3.50000	0.06600	0.3500
F_{TFSI}	2.95000	0.05300	-0.1600
O_{Water}	3.16600	0.15530	-0.8476
H_{Water}	0.00000	0.00000	0.4238
B_{BNNT}	3.45300	0.09490	0.76000
N_{BNNT}	3.36500	0.14500	-0.76000

Table A1. LJ parameters and charges for all the atom types considered in the present study.

Interacting groups	LJ interaction energy (kcal/mol)	Electrostatic interaction energy (kcal/mol)
$TFSI^-$ - BNNT	-45.51	-2.29
Li^+ - BNNT	-0.36	-3.25
Water - BNNT	-3.55	-0.14

Table A2. Decomposition of the interaction energy between the BNNT and the salt ions and water molecules confined inside the BNNT. The interaction energies between $TFSI^-$ - BNNT, Li^+ - BNNT, and water-BNNT are normalized by the respective number of $TFSI^-$ ions, Li^+ ions, and water molecules inside the BNNT.

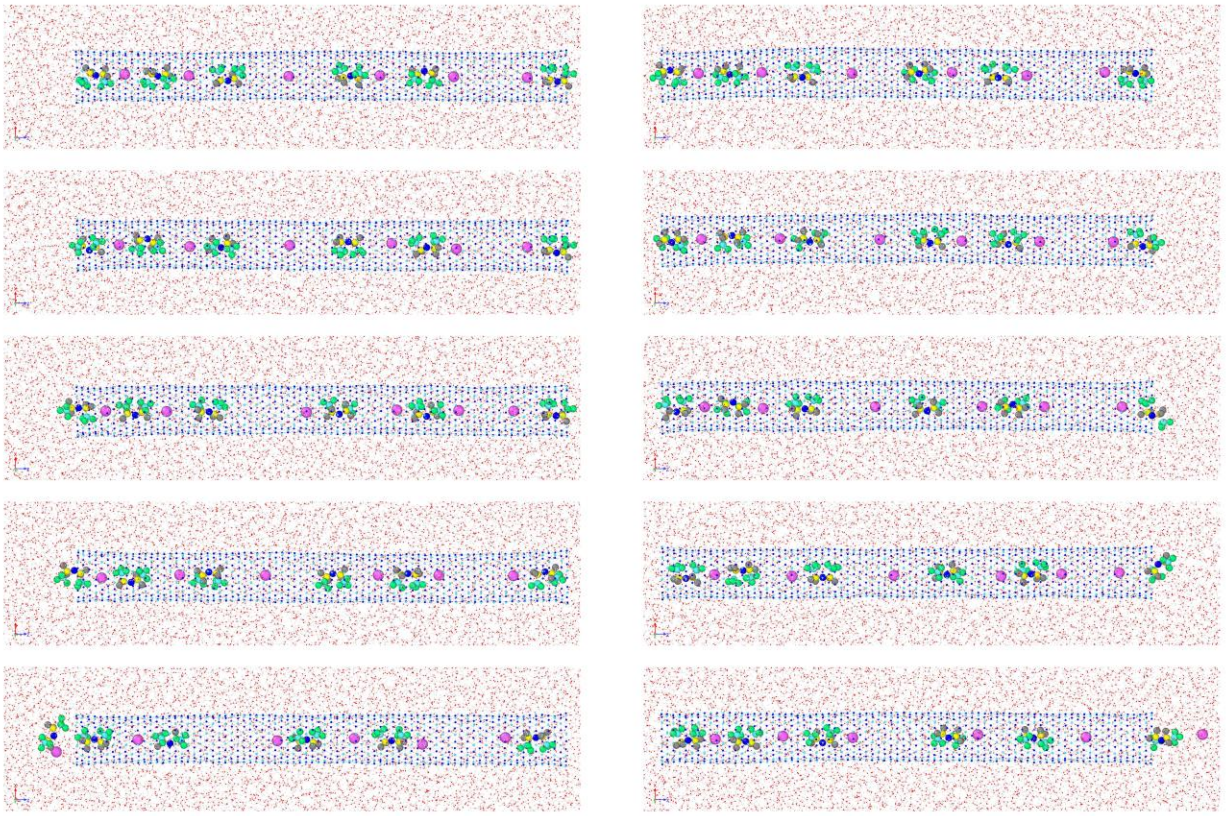

Figure A1. Simulation snapshots of the nanotube hybrid during umbrella sampling simulations to obtain free energy curves for LiTFSI pair at a) the lower end (near z = 0 Å) and b) the upper end (near z = 100 Å) of the nanotube. The snapshots are generated using OVITO.[100]

Appendix B

Supporting information for chapter 3 is presented here.

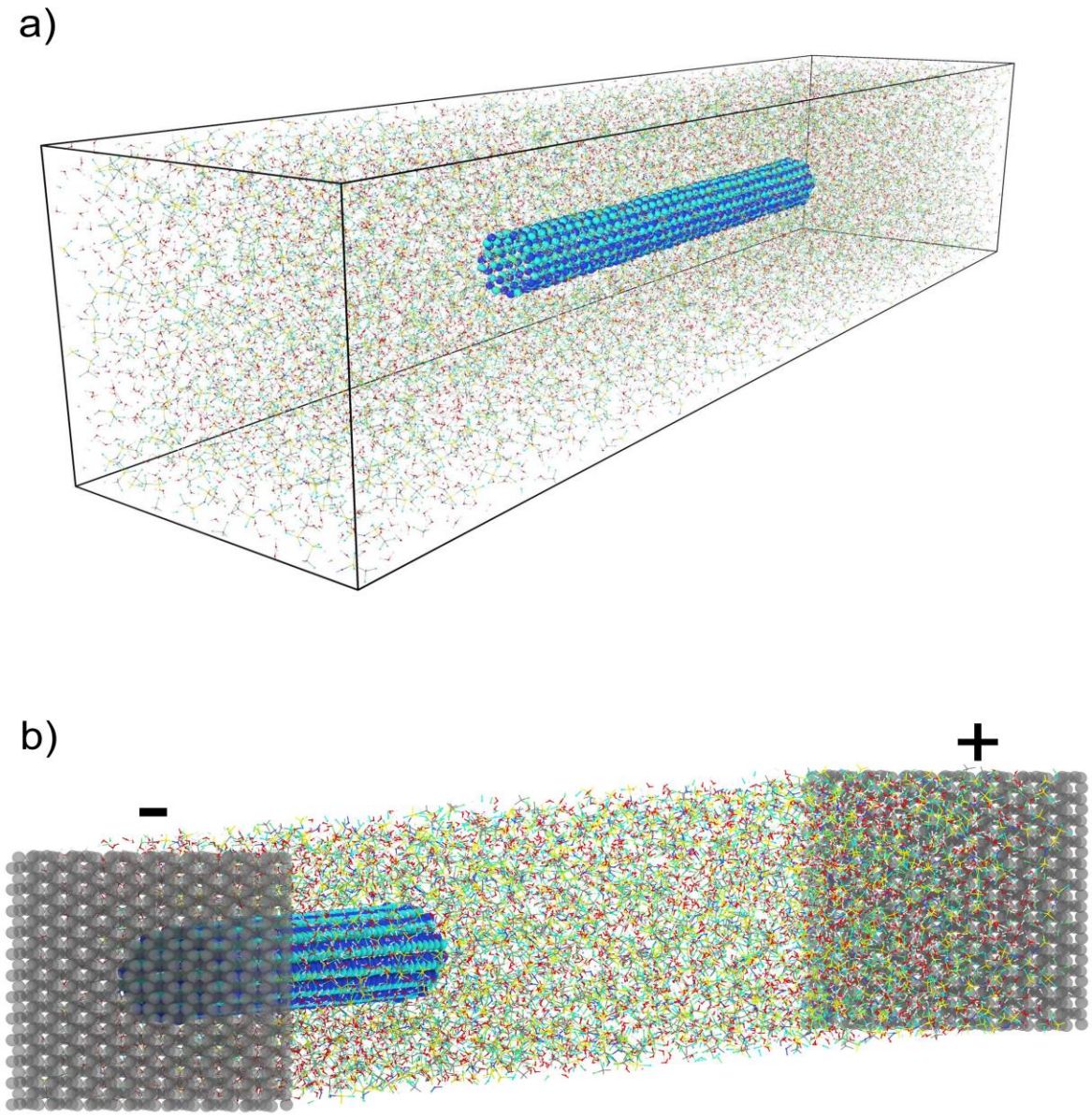

Figure B1. Simulation Set-up. Simulation snapshot of 10 m LiTFSI aqueous solution filling in 1-nm-diameter BNNT a) in the absence of applied electric potential difference and b) in the presence of an applied electric potential difference of 5 V [negative (-2.5 V) and positive (2.5 V) electrodes are labeled accordingly]. All the simulation snapshots are generated using OVITO.[100]

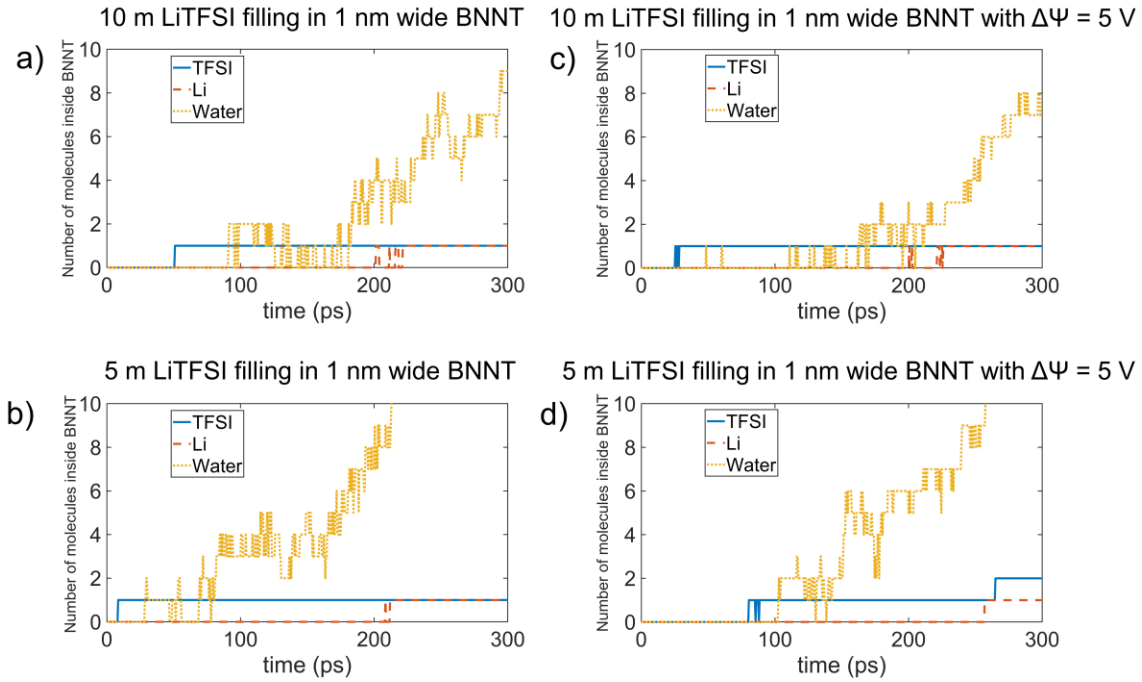

Figure B2. Filling profiles of LiTFSI filling in 1 nm-wide BNNT. Dynamics (quantified by the variation of the corresponding number of $TFSI^-$ ion, Li^+ ion, and water molecules) of the first 300 ps filling of the 1-nm-diameter BNNT with (a) 10 m LiTFSI WISE, (b) 5 m LiTFSI WISE, (c) 10 m LiTFSI WISE in the presence of an applied electric potential difference of 5 V [for the set-up shown in Fig. B1(b)], and (d) 5 m LiTFSI WISE in the presence of an applied electric potential difference of 5 V [similar set-up as Fig. B1(b)]. We see that for all the cases, $TFSI^-$ ion enters the tube first followed by the water molecules, and the Li^+ ion.

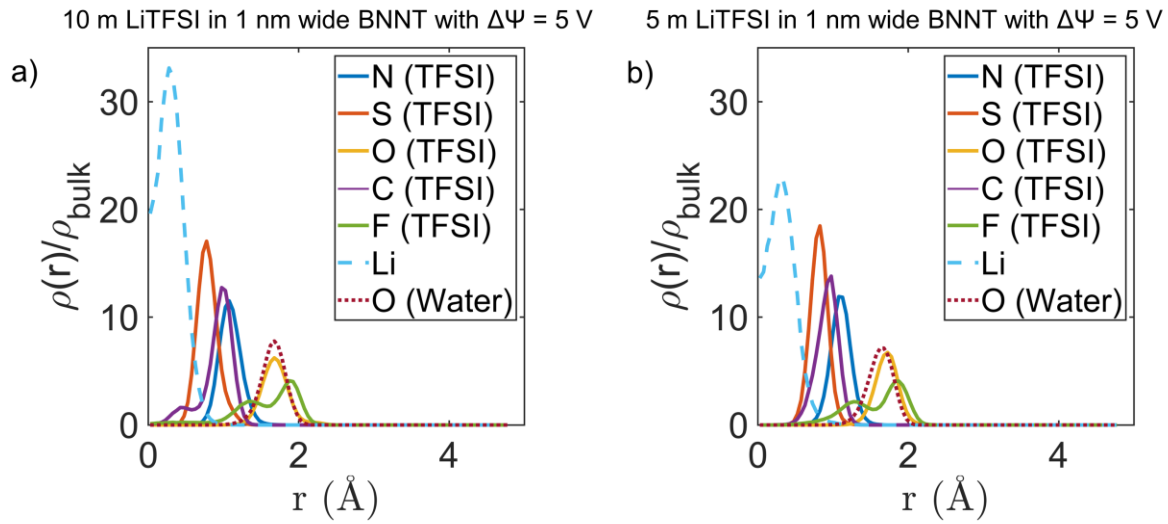

Figure B3. Radial Distribution of the Ions and Water Molecules Confined in 1 nm-diameter BNNT in the Presence of an Applied Electric Potential Difference of 5 V. Radial distribution of the different atoms of the $TFSI^-$ ion, Li^+ ion, and the oxygen atom of the water molecule for (a) 10 m LiTFSI confined in 1-nm-diameter BNNT and (b) 5 m LiTFSI confined in 1-nm-diameter BNNT. For these cases, an electric potential difference of 5 V has been applied between the electrodes with -2.5V applied at the negative electrode which is present at one end of the BNNT with the other end open to bulk electrolyte [see Fig. B1(b) for the MD simulation snapshot confirming the set-up].

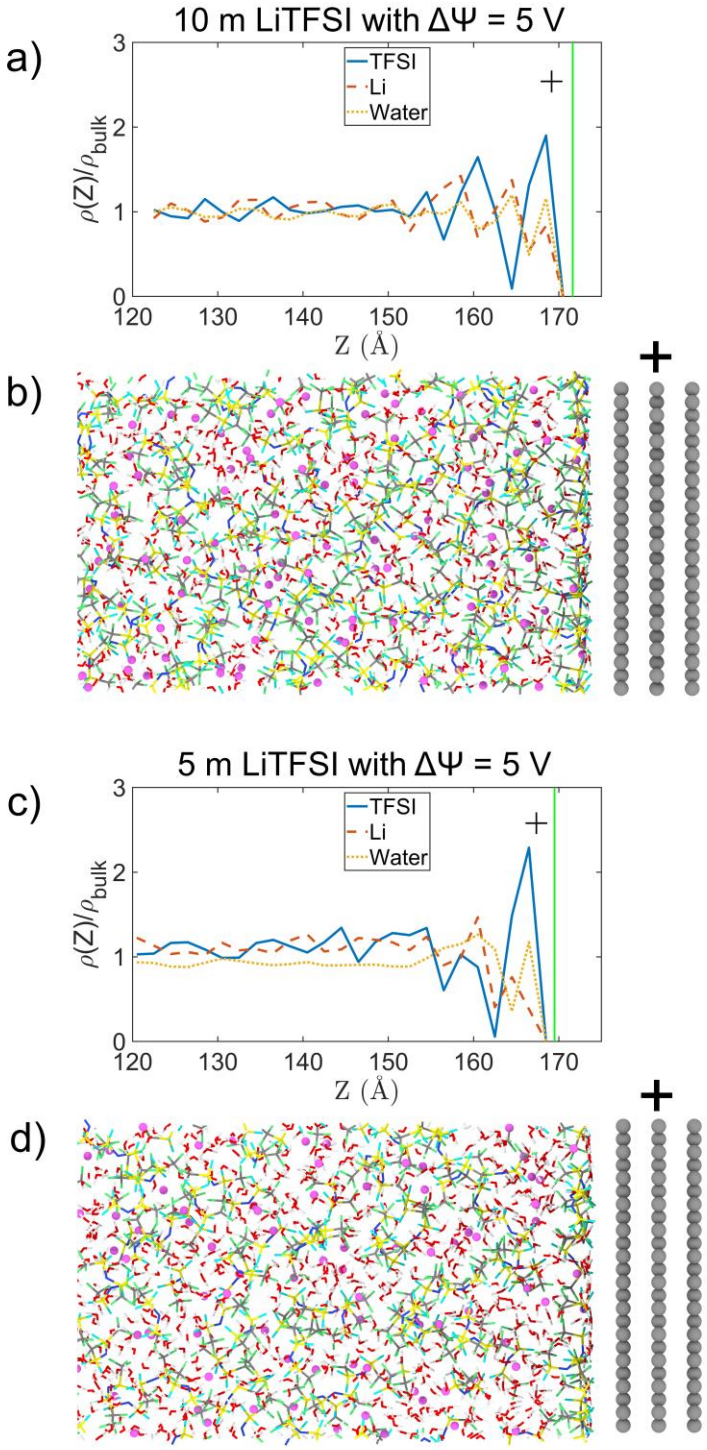

Figure B4. Distribution of the Ions and Water Molecules at the Positive Electrode. Distribution of nitrogen atoms (representing the $TFSI^-$ ion), Li^+ ion, and water oxygen atoms for (a) 10 m LiTFSI near the positive electrode (2.5V) and (c) 5 m LiTFSI near the positive electrode (2.5V). Subfigures (b) and (d) show the corresponding MD simulations snapshots, generated using OVITO,[100] of the electrolyte distribution near the positive electrode.

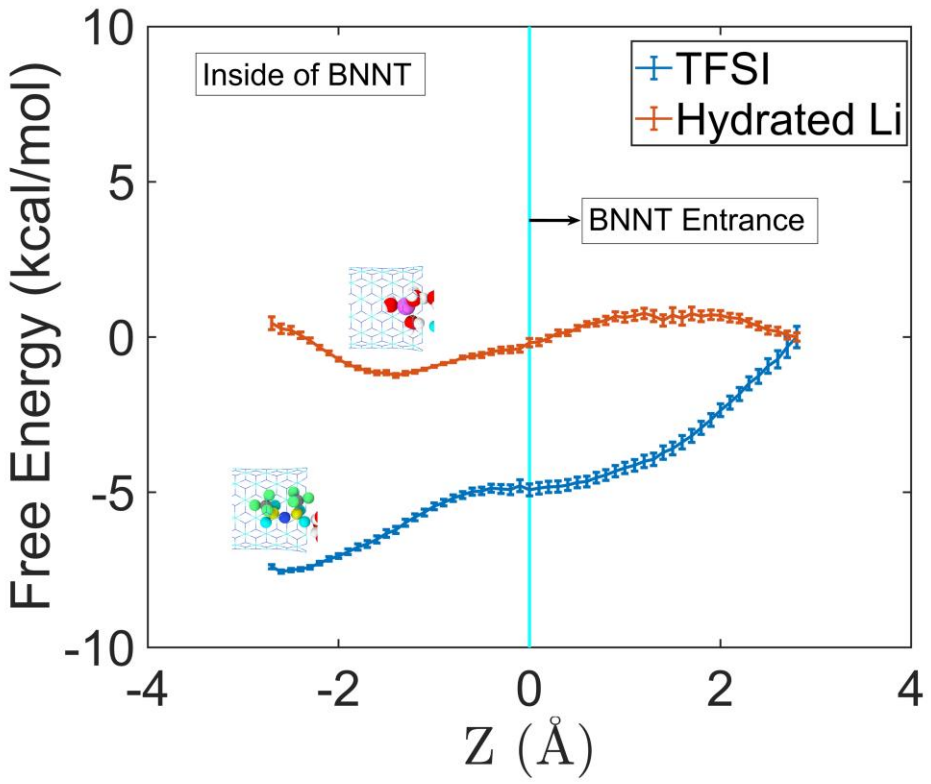

Figure B5. Free energy curves. Free energy curves, as a function of axial position with respect to the BNNT entrance, corresponding to the entry of $TFSI^-$ ion and Hydrated Li (Li^+ along with its primary hydration shell) from bulk 5 m aqueous LiTFSI solution into the 1 nm wide empty BNNT in the presence of an applied electric potential difference of 5 V (with an electric potential of -2.5 V at the negative electrode). The set-up is identical to that elucidated in Fig. 3.6D. The cyan line indicates the BNNT entrance. The snapshots, generated using OVITO,[100] above each curve show the axial position of $TFSI^-$ ion and hydrated Li associated with their free energy minima inside the 1 nm wide BNNT. The error bars were estimated using the Monte Carlo bootstrap algorithm.[94]

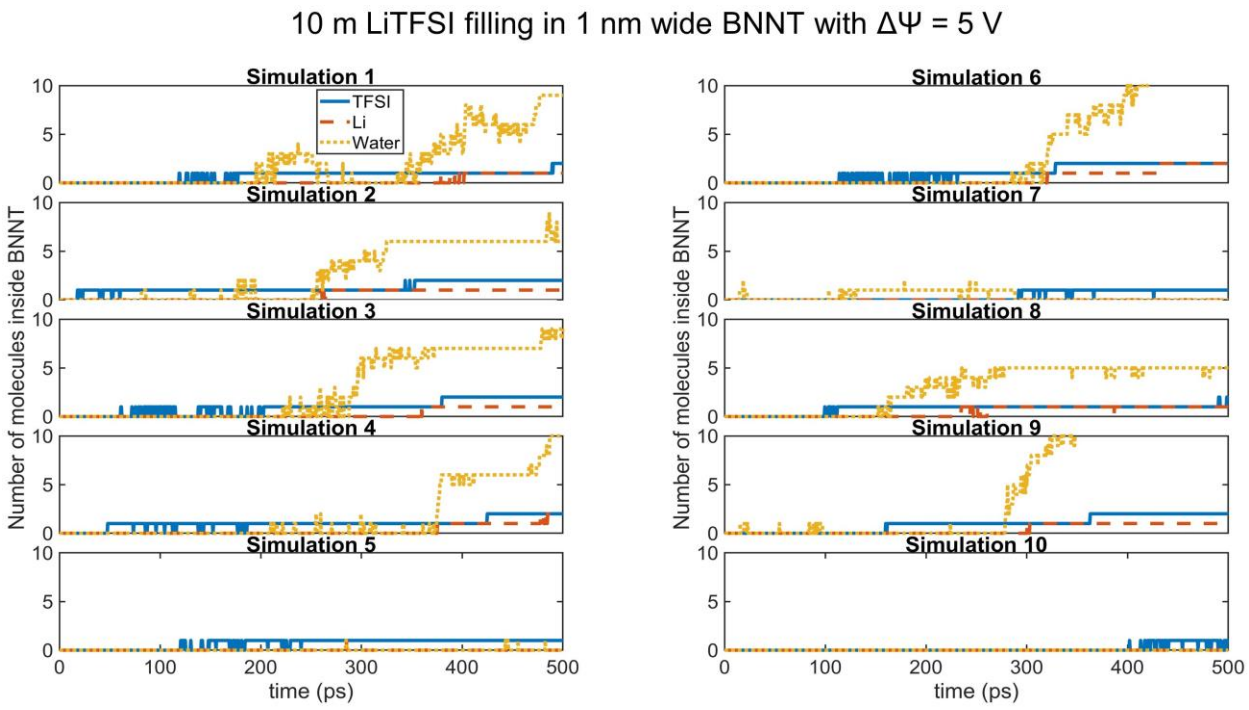

Figure B6. Multiple Filling Profiles of 10 m LiTFSI filling in 1 nm-wide BNNT. Ten different filling profiles (for the first 500 ps) of 10 m LiTFSI into 1 nm wide BNNT in the presence of an applied electric potential difference of 5 V. These profiles are obtained from ten different filling simulations performed with various initial system configurations.

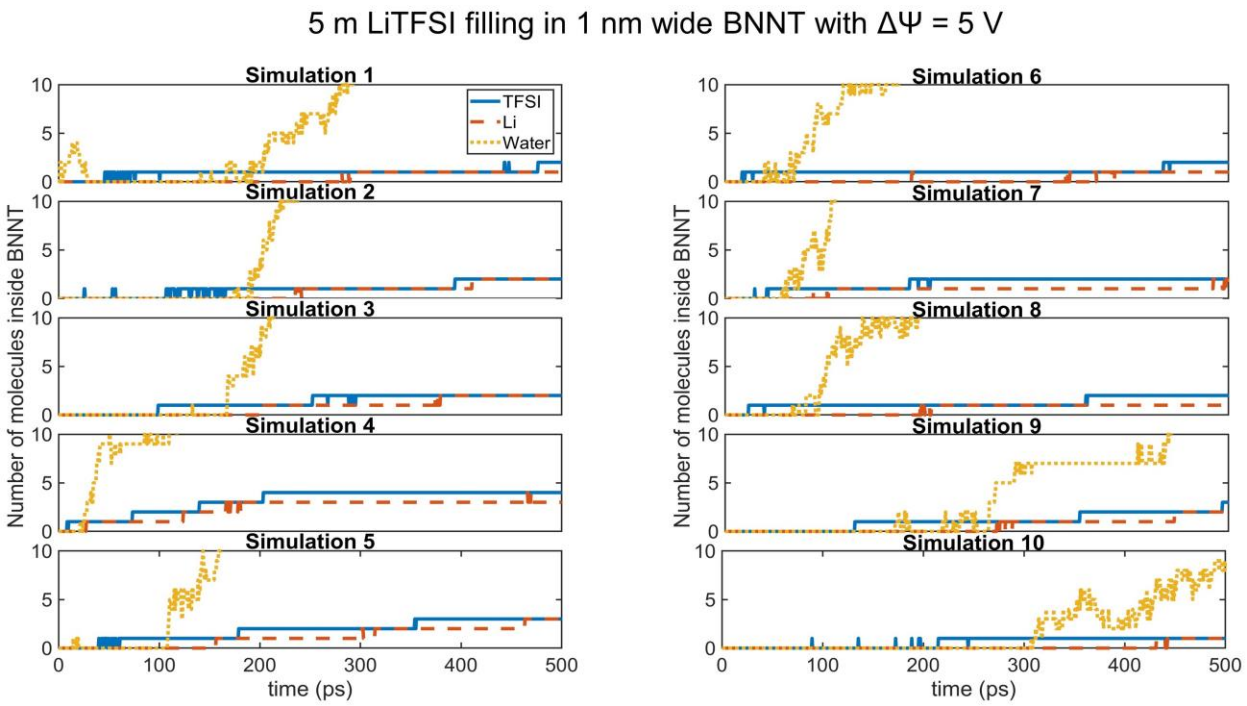

Figure B7. Multiple Filling Profiles of 5 m LiTFSI filling in 1 nm-wide BNNT. Ten different filling profiles (for the first 500 ps) of 5 m LiTFSI into 1 nm wide BNNT in the presence of an applied electric potential difference of 5 V. These profiles are obtained from ten different filling simulations performed with various initial system configurations.

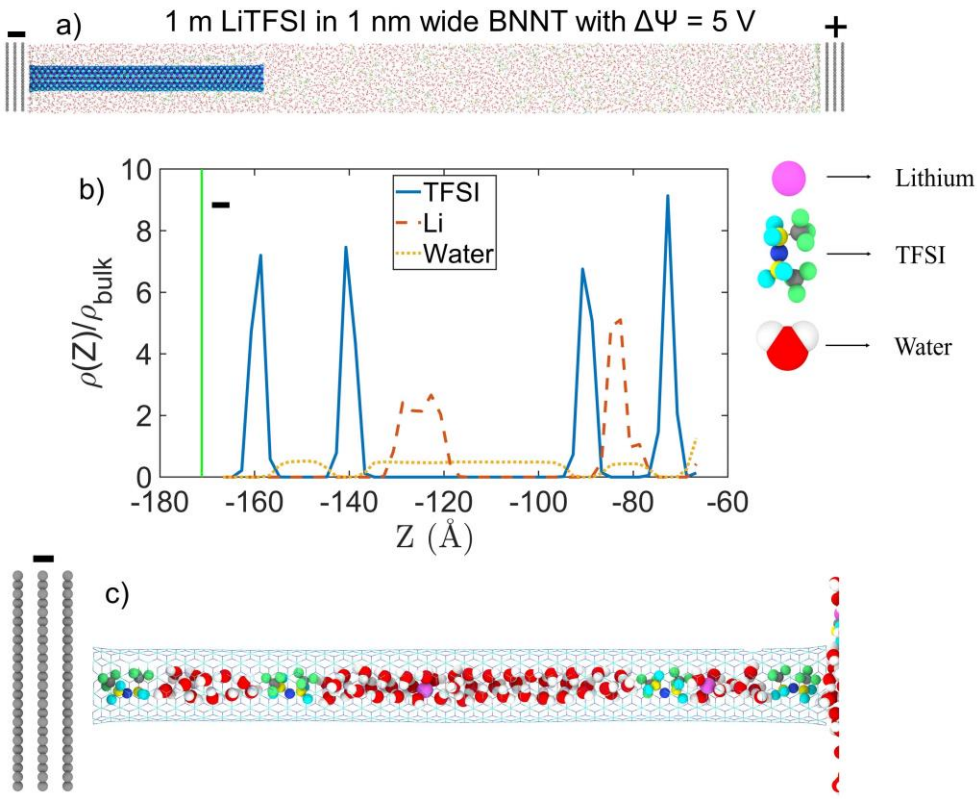

Figure B8. Axial Distribution of the Ions and Water Molecules of 1 m LiTFSI Confined in 1 nm-diameter BNNT in the Presence of an Applied Electric Potential Difference of 5 V (a) MD simulation snapshots showing the entire system for the case of 1 m LiTFSI WISE confined in 1-nm-diameter BNNT. For this case an electric potential difference of 5 V is applied across these systems. The negative and positive electrodes are labeled accordingly and the electric potentials associated with those electrodes are -2.5 V and 2.5 V respectively. One end of the BNNT is placed near the negative electrode, while the other end is open to the bulk. (b) Axial distribution of the nitrogen atoms (representing the $TFSI^-$ ion), Li^+ ions, and water oxygen atoms (representing the water molecules) inside the 1-nm-diameter BNNT. The green lines indicate the presence of a negative electrode with a potential of -2.5 V. (c) MD simulation snapshots showcasing the distribution of the different species including the local arrangement of salt ions and water molecules inside the 1-nm-diameter BNNT. In (c) atoms surrounding the BNNT were removed, to provide a clearer picture of electrolyte distribution inside the BNNT. All the simulation snapshots are generated using OVITO.[100] The axial distribution profiles confirm that while the localization of the $TFSI^-$ ion, inside the 1-nm-diameter BNNT, still persists near the negative electrode, the Li^+ ion concentration peak is more deviated away from the negative electrode and there is a lack of lithium near the negative electrode at this weaker value of the LiTFSI salt concentration.

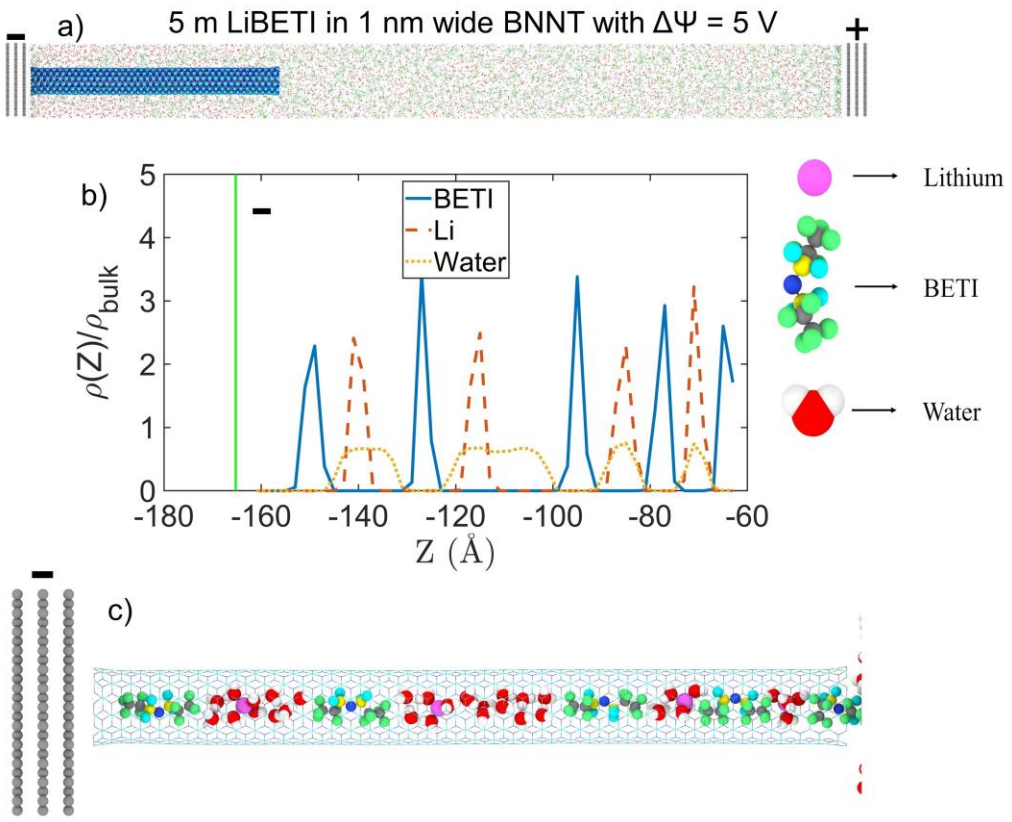

Figure B9. Axial Distribution of the Ions and Water Molecules of 5 m LiBETI Confined in 1 nm-diameter BNNT in the Presence of an Applied Electric Potential Difference of 5 V (a) MD simulation snapshots showing the entire system for the case of 5 m LiBETI WISE confined in 1-nm-diameter BNNT. For this case an electric potential difference of 5 V is applied across these systems. The negative and positive electrodes are labeled accordingly and the electric potentials associated with those electrodes are -2.5 V and 2.5 V respectively. One end of the BNNT is placed near the negative electrode, while the other end is open to the bulk. (b) Axial distribution of the nitrogen atoms (representing the $TFSI^-$ ion), Li^+ ions, and water oxygen atoms (representing the water molecules) inside the 1-nm-diameter BNNT. The green lines indicate the presence of a negative electrode with a potential of -2.5 V. (c) MD simulation snapshots showcasing the distribution of the different species including the local arrangement of salt ions and water molecules inside the 1-nm-diameter BNNT. In (c) atoms surrounding the BNNT were removed, to provide a clearer picture of electrolyte distribution inside the BNNT. All the simulation snapshots are generated using OVITO.[100] A careful study of these distributions reveals that there is the water-free localization of the $BETI^-$ ion at the negative electrode inside the 1-nm-diameter-BNNT.

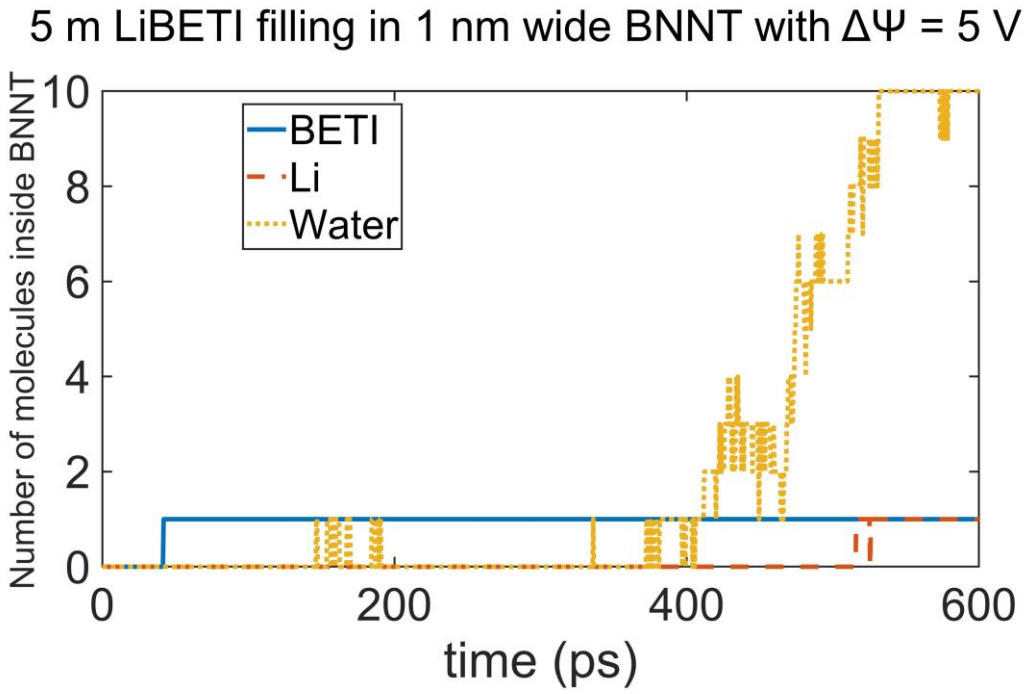

Figure B10. 5 m LiBETI Filling in 1 nm-wide BNNT in the Presence of External Electric Potential Difference. Dynamics (quantified by the variation of the corresponding number of $BETI^-$ ion, Li^+ ion, and water molecules) of the first 600 ps filling of the 1-nm-diameter BNNT with 5 m LiBETI WISE in the presence of an applied electric potential difference of 5 V [set-up as shown in Fig. B9(a)]. We see that, $BETI^-$ ion enters the tube first followed by the water molecules, and the Li^+ ion.

Electrolyte concentration	TFSI block thickness in axial direction	TFSI block thickness in radial direction	Water block thickness in axial direction	Water block thickness in radial direction
10 m	9.1 Å	5.2 Å	6 Å	4.8 Å
5 m	9.1 Å	5.2 Å	13.6 Å	4.8 Å

Table B1. Block Thickness. Average thickness of "blocks" of water molecules and $TFSI^-$ ion confined in a 1-nm-diameter BNNT in presence of an applied potential difference of 5 V

Note B1. Properties of Axial Non-overlapping Blocks of Water Molecules And $TFSI^-$ Ion in 1-nm-diameter BNNT in Presence of an Applied Voltage Difference

Inside the 1-nm-diameter BNNT, we observe distinct, non-overlapping axial blocks of $TFSI^-$ ion and the water molecules (see Fig. 3.1 in the chapter 3 for a schematic illustration). We define a block as the region inside the 1-nm-diameter BNNT, where the axial density of $TFSI^-$ ion (water molecules) is non-zero while the axial density of water molecules ($TFSI^-$ ion) is zero. Using this definition of "block", we can clearly differentiate between the $TFSI^-$ blocks and water blocks inside the 1-nm-diameter BNNT based on the axial distribution profiles.

Under such circumstances, we provide (see Table B1) the average block thicknesses of the 1-nm-diameter BNNT-confined blocks of $TFSI^-$ ion and water molecules in presence of an applied potential difference of 5 V [i.e., the system configuration shown in Fig. B1(b)]. Please note that here we only provide results for the case of a 1-nm BNNT in presence of an applied voltage. However, such block formation equally occurs for the case of a 1-nm BNNT in absence of an applied voltage (see Fig. 3.2 in the main paper).

As can be seen from the thickness values for different blocks provided in Table B1, the thickness of different blocks in 1-nm-diameter BNNT is not always similar. The axial thickness of the

TFSI blocks is similar, for both 5m and 10m LiTFSI confined in 1-nm-diameter BNNT, since each TFSI block is comprised of one $TFSI^-$ ion and the length of the $TFSI^-$ ion along its longest dimension is independent of concentration. However, the axial thickness of the water block is different for both the two cases. This is due to the fact that each water block for 5m-case contains more water molecules on an average as compared to the 10m-case. The radial thickness of the blocks of $TFSI^-$ ions and water molecules are similar for both 5m and 10m LiTFSI in 1-nm-diameter BNNT due to their similar radial distribution profiles, as shown in Fig. B3.

The procedure that we have employed to calculate the thicknesses of the water and $TFSI^-$ ion blocks is described as follows. First, we calculated the approximate average $TFSI^-$ ion block axial thickness in the following manner. The farthest distance, in the axial direction, between the atoms of a $TFSI^-$ ion was averaged over all the $TFSI^-$ ions inside the tube for the last 5 ns of the simulation run. To calculate the axial thickness of the $TFSI^-$ ion block, we summed the above-obtained distance with the van der Waals diameter of TFSI fluorine atoms (since fluorine atoms are the farthest apart in the axial direction). This thickness approximately equals to the length of $TFSI^-$ ion along its longest dimension[99] as this dimension is aligned parallel to the axis of the 1-nm-diameter BNNT.

Using this TFSI block axial thickness, we calculated the average water block axial thickness using the following expression:

$$\text{Water block axial thickness} = \frac{length\ of\ BNNT - (number\ of\ TFSI\ blocks\ \times\ TFSI\ block\ axial\ thickness)}{number\ of\ water\ blocks}.$$

Finally, we calculated the radial thickness of both the water and $TFSI^-$ ion blocks using the radial density profiles given in Fig. B3. We considered the radial distance, from the BNNT axis, beyond which the radial density of TFSI atoms (or water oxygen atoms for the case of water block) vanished, and the block thickness in the radial direction is twice this radial distance.

Appendix C

Supporting information for chapter 4 is presented here.

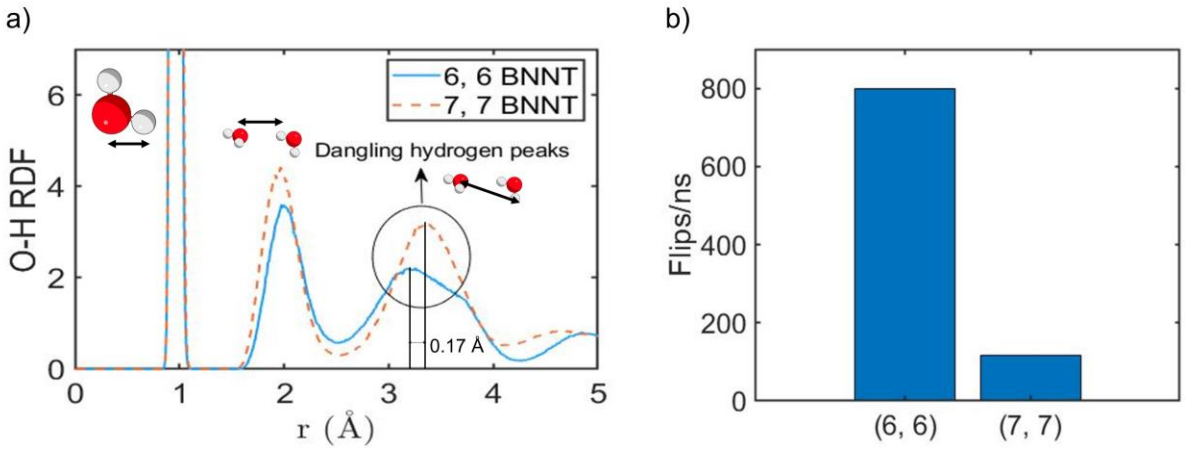

Figure C1. a) Oxygen-hydrogen radial distribution functions for water confined in (6, 6) and (7, 7) BNNTs. Here, the first and second peaks correspond to the O-H covalent bonds and O-H hydrogen bonds respectively, while the third peak represents the distance between the oxygen atom of a water molecule and the dangling hydrogen atom of a neighboring water molecule. b) Normalized rate of water molecule flipping about the axis perpendicular to the molecular plane in (6, 6) and (7, 7) BNNTs.

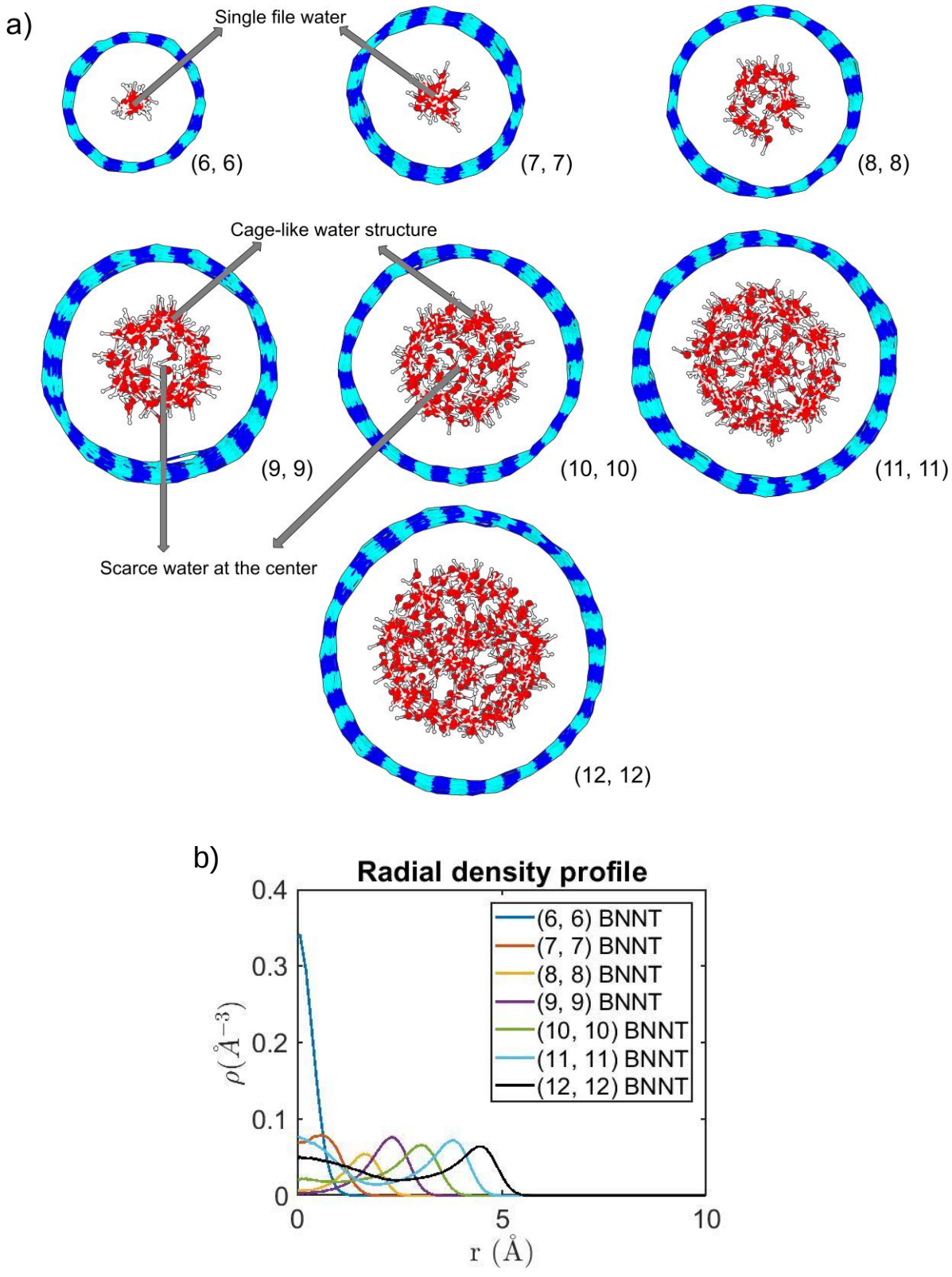

Figure C2. a) Cross-sectional snapshots and b) water-oxygen radial density profiles for water molecules confined in BNNTs of various diameters.

a)

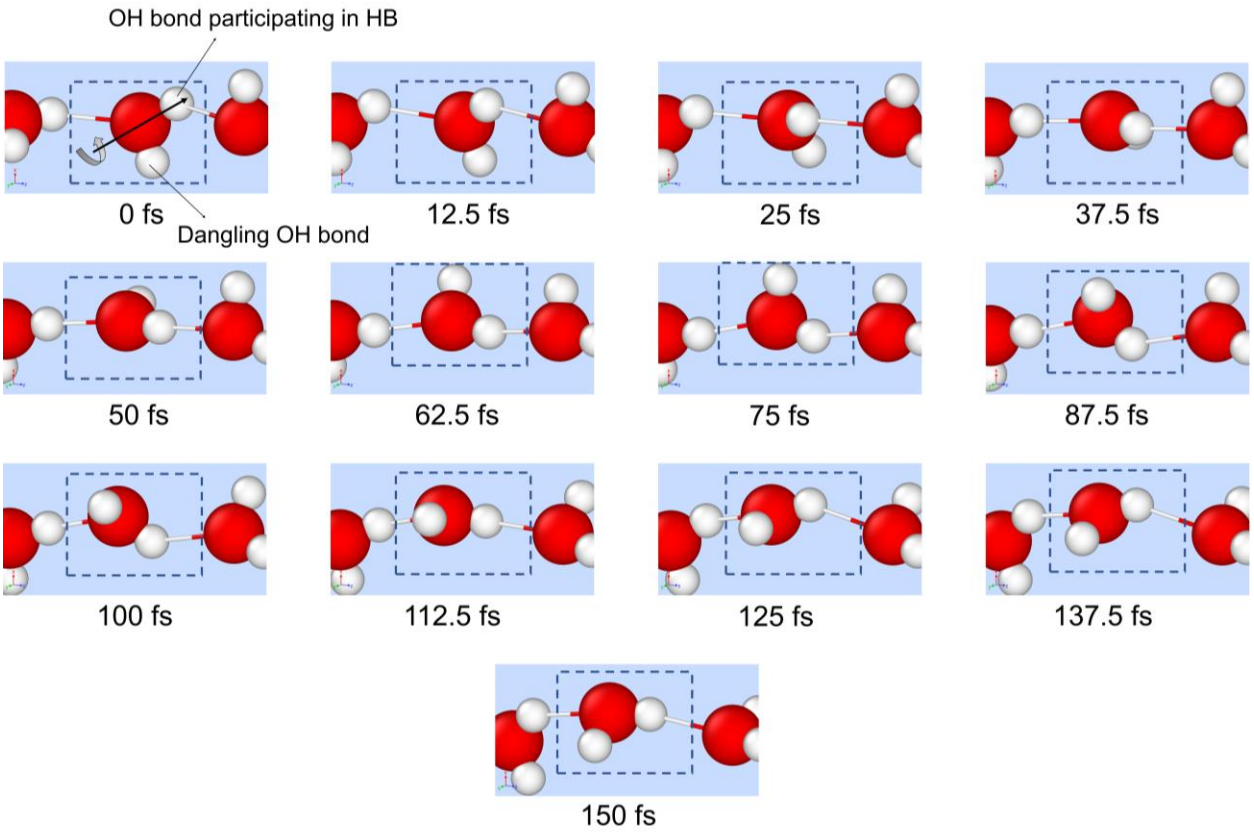
OH bond participating in HB
0 fs
Dangling OH bond
12.5 fs
25 fs
37.5 fs
50 fs
62.5 fs
75 fs
87.5 fs
100 fs
112.5 fs
125 fs
137.5 fs
150 fs

b)

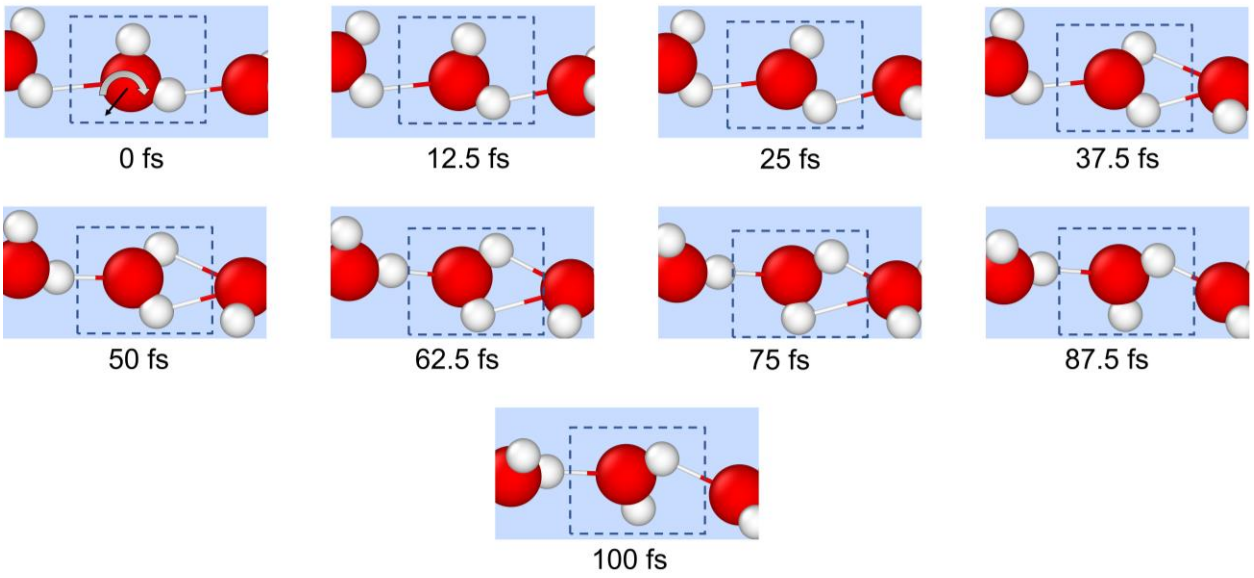
0 fs
12.5 fs
25 fs
37.5 fs
50 fs
62.5 fs
75 fs
87.5 fs
100 fs

Figure C3. Time series of simulation snapshots highlighting (a) the rotation of a water molecule about the axis parallel to the hydrogen bonding OH bond and b) the flipping of a water molecule about the axis perpendicular to the molecular plane, in the (6, 6) BNNT.

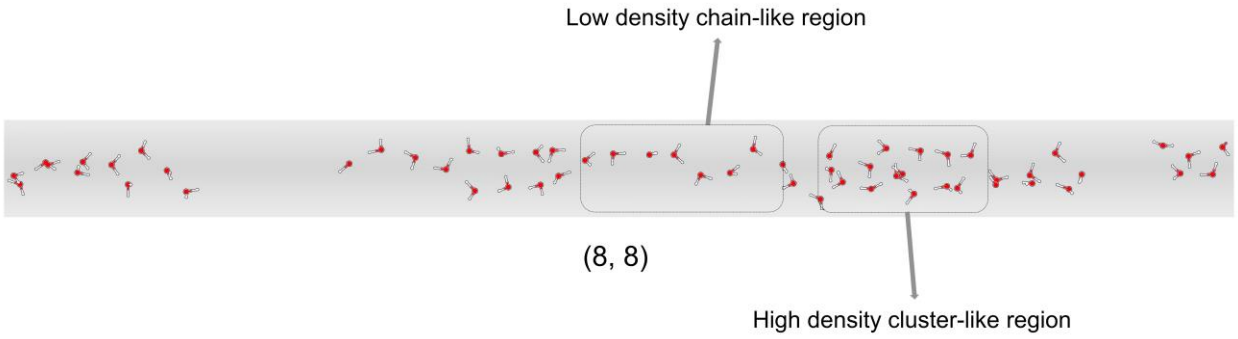

Figure C4. Simulation snapshot highlighting the low-density chain-like regions and the high-density cluster-like regions in the water structure inside a (8, 8) BNNT.

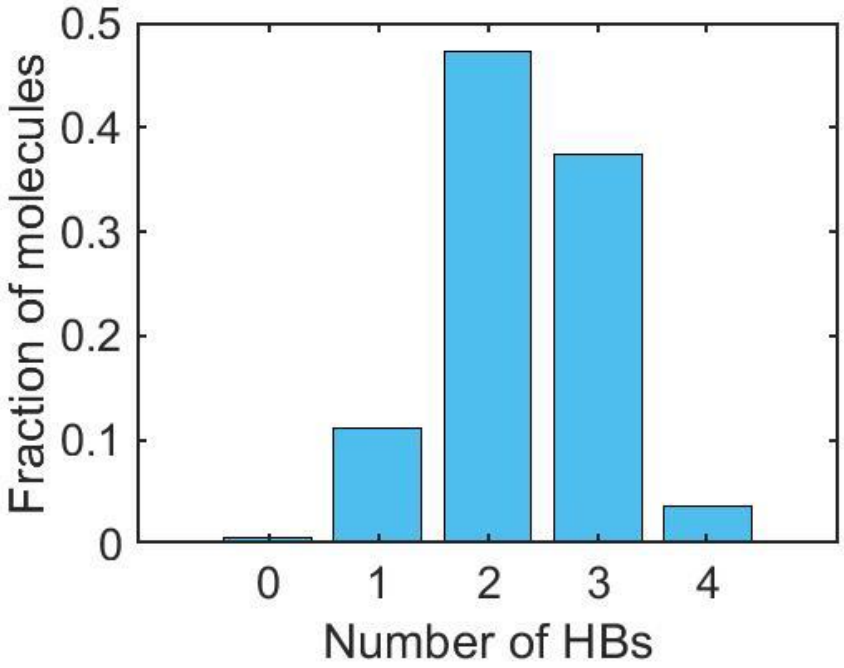

Figure C5. Average fraction of water molecules forming 0, 1, 2, 3 and 4 hydrogen bonds inside a (8, 8) BNNT.

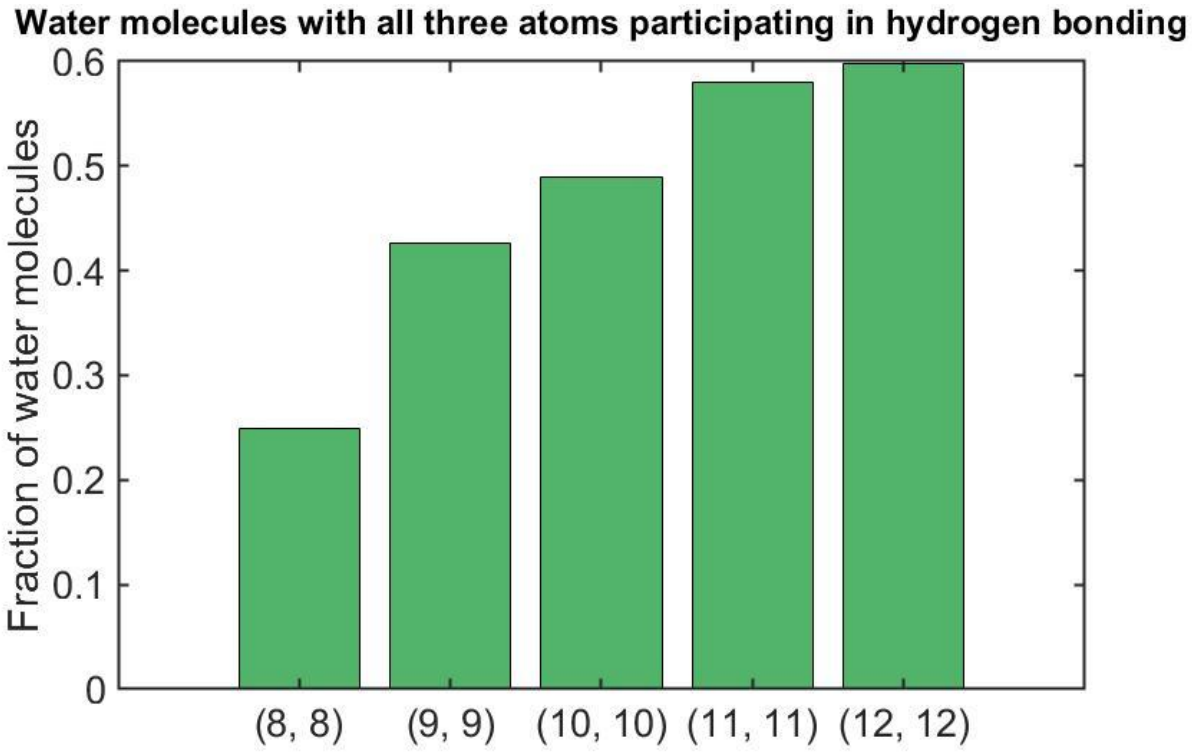

Figure C6. Average fraction of water molecules donating both hydrogens and accepting at least one HB for water confined in (8, 8), (9, 9), (10, 10), (11, 11) and (12, 12) BNNTs.

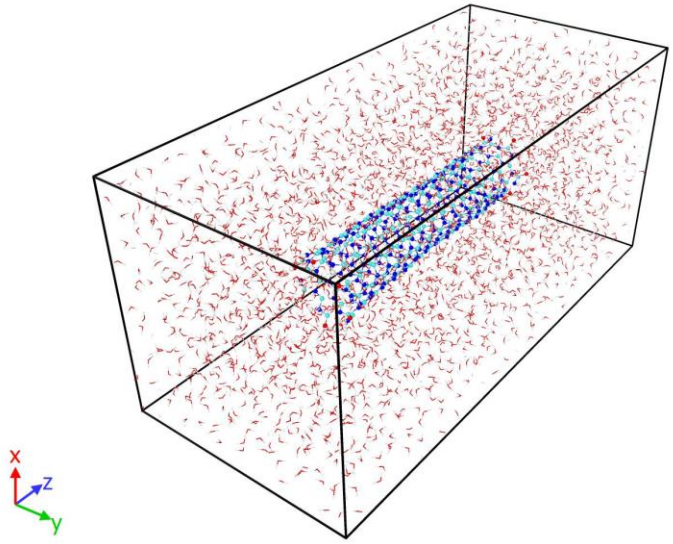

Figure C7. Simulation setup showing a 4-nm long open-ended (6, 6) BNNT soaked in bulk water comprised of 3000 water molecules. The boron and nitrogen atoms at the open ends were functionalized using hydroxide (OH) and hydrogen (H) groups respectively.

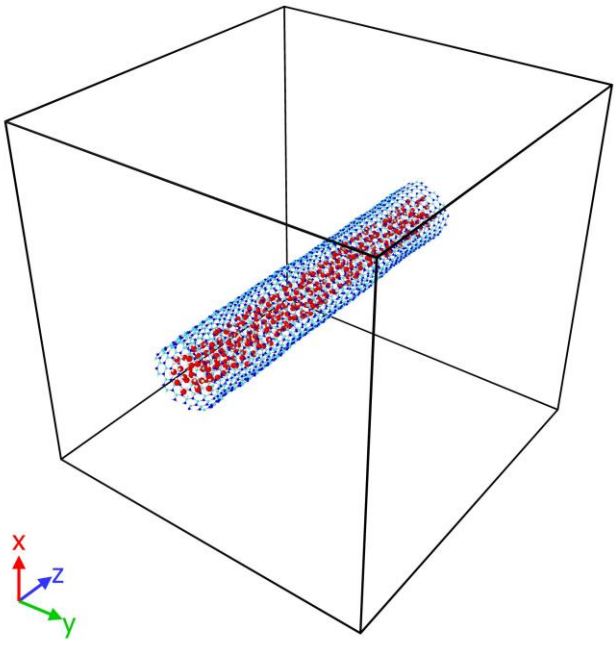

Figure C8. Simulation setup showing an infinitely long (12, 12) BNNT filled with water.

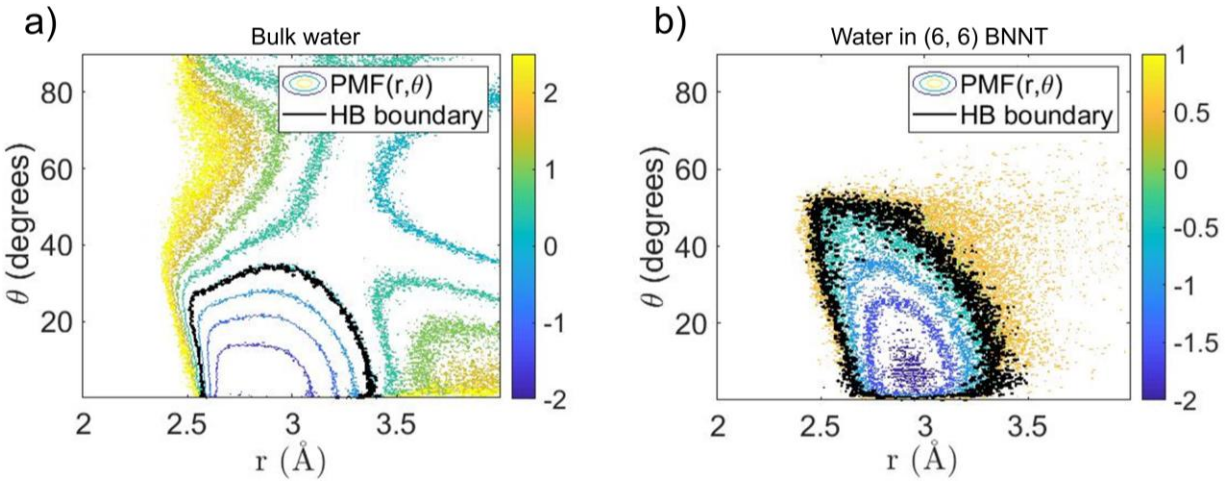

Figure C9. The two-dimensional potentials of mean force for a) bulk water and b) water confined in (6, 6) BNNT. The black contour lines represent the boundary separating the HB basin. The colorbars have the units of kcal/mol.

BNNT chiral index	Simulation length	Production length	Water count per nm
(6, 6)	1.5 ns	1 ns	3.003
(7, 7)	1.5 ns	1 ns	3.614
(8, 8)	2.5 ns	1.5 ns	5.712
(9, 9)	1.5 ns	1 ns	12.26
(10, 10)	1.5 ns	1 ns	17.258
(11, 11)	1.5 ns	1 ns	25.38
(12, 12)	1.5 ns	1 ns	31.442

Table C1. Total simulation lengths, production lengths and the resulting BNNT-confined-water number densities obtained from the NPT simulations of open-ended BNNTs, of various diameters, soaked in bulk water.

Bibliography

1. Sun, C., Zhou, R., Zhao, Z., & Bai, B. (2020). Nanoconfined fluids: What can we expect from them?. The Journal of Physical Chemistry Letters, 11(12), 4678-4692.
2. Chen, C.; Kuang, Y.; Hu, L. (2019) Challenges and Opportunities for Solar Evaporation. Joule, 3, 683−718.
3. Huang, L.; Zhang, M.; Li, C.; Shi, G. (2015) Graphene-Based Membranes for Molecular Separation. J. Phys. Chem. Lett., 6, 2806−2815.
4. Luan, B.; Zhou, R. Single-File Protein Translocations through Graphene−MoS2 Heterostructure Nanopores. J. Phys. Chem. Lett. 2018, 9, 3409−3415.
5. He, Z.; Zhou, J.; Lu, X.; Corry, B. (2013) Ice-like Water Structure in Carbon Nanotube (8,8) Induces Cationic Hydration Enhancement. J. Phys. Chem. C, 117, 11412−11420.\
6. Pham, T. A.; Mortuza, S. G.; Wood, B. C.; Lau, E. Y.; Ogitsu, T.; Buchsbaum, S. F.; Siwy, Z. S.; Fornasiero, F.; Schwegler, E. (2016) Salt solutions in carbon nanotubes: The role of cation- π interactions. J. Phys. Chem. C, 120, 7332−7338.
7. Perez Sirkin, Y. A.; Hassanali, A.; Scherlis, D. A. (2018) One Dimensional Confinement Inhibits Water Dissociation in Carbon Nanotubes. J. Phys. Chem. Lett., 9, 5029−5033.
8. Cao, Z.; Peng, Y. X.; Yan, T. Y.; Li, S.; Li, A. L.; Voth, G. A. (2010) Mechanism of Fast Proton Transport Along One-Dimensional Water Chains Confined in Carbon Nanotubes. J. Am. Chem. Soc., 132, 11395−11397.
9. Bankura, A.; Chandra, A. (2012) Hydroxide ion can move faster than an excess proton through one-dimensional water chains in hydrophobic narrow pores. J. Phys. Chem. B, 116, 9744−9757.

10. Pial, T.H.; Wang, Y.; Das, S. (2019) Non-monotonic dependence of fluid dissipation on fluid density in fluid-coupled nanoresonators. Appl. Phys. Lett., 115(25), p.251601.
11. De, S.; Aluru, N. R. (2018) Energy dissipation in fluid coupled nanoresonators: The effect of phonon-fluid coupling. ACS nano, 12(1), pp.368-377.
12. De, S.; Aluru, N. R. (2019) Anomalous scaling of flexural phonon damping in nanoresonators with confined fluid. Microsyst. Nanoeng., 5(1), pp.1-13.
13. Hong, Y.; Zhang, J.; Zhu, C.; Zeng, X. C.; Francisco, J. S. (2019) Water Desalination through Rim Functionalized Carbon Nanotubes. J. Mater. Chem. A, 7, 3583−3591.
14. Wang, X.; Shi, G.; Liang, S.; Liu, J.; Li, D.; Fang, G.; Liu, R.; Yan, L.; Fang, H. (2018) Unexpectedly high salt accumulation inside carbon nanotubes soaked in dilute salt solutions. Phys. Rev. Lett., 121(22), p.226102.
15. Hilder, T. A.; Gordon, D.; Chung, S. H. (2009) Salt Rejection and Water Transport through Boron Nitride Nanotubes. Small, 5, 2183−2190.
16. Kim, J. H., Pham, T. V., Hwang, J. H., Kim, C. S., & Kim, M. J. (2018). Boron nitride nanotubes: synthesis and applications. Nano convergence, 5(1), 1-13.
17. Suo, L.; Borodin, O.; Gao, T.; Olguin, M.; Ho, J.; Fan, X.; Luo, C.; Wang, C.; Xu, K. (2015) "Water-in-Salt" Electrolyte Enables High-Voltage Aqueous Lithium-Ion Chemistries Science, 350, 938– 943.
18. Kamath, G., & Baker, G. A. (2013). Are ionic liquids suitable media for boron nitride exfoliation and dispersion? Insight via molecular dynamics. RSC advances, 3(22), 8197-8202.

19. Li, Y., Zhang, L., Sun, Z., Gao, G., Lu, S., Zhu, M., ... & Ding, S. (2020). Hexagonal boron nitride induces anion trapping in a polyethylene oxide based solid polymer electrolyte for lithium dendrite inhibition. Journal of Materials Chemistry A, 8(19), 9579-9589.
20. Won, C. Y., & Aluru, N. R. (2008). Structure and dynamics of water confined in a boron nitride nanotube. The Journal of Physical Chemistry C, 112(6), 1812-1818.
21. Zhang, L., Li, J., Peng, G., Liang, L., Kong, Z., Shen, J. W., ... & Zhang, W. (2018). Charge-tunable water transport through boron nitride nanotubes. Journal of Molecular Liquids, 258, 98-105.
22. Azamat, J., Ghasemi, F., Sardroodi, J. J., & Jahanshahi, D. (2021). Molecular dynamics simulation of separation of water/methanol and water/ethanol mixture using boron nitride nanotubes. Journal of Molecular Liquids, 331, 115774.
23. Li, X., Qiu, H., Liu, X., Yin, J., & Guo, W. (2017). Wettability of supported monolayer hexagonal boron nitride in air. Advanced Functional Materials, 27(19), 1603181.
24. Verma, A., Zhang, W., & Van Duin, A. C. (2021). ReaxFF reactive molecular dynamics simulations to study the interfacial dynamics between defective h-BN nanosheets and water nanodroplets. Physical Chemistry Chemical Physics, 23(18), 10822-10834.
25. Rao, R.; Pint, C. L.; Islam, A. E.; Weatherup, R. S.; Hofmann, S.; Meshot, E. R.; Wu, F.; Zhou, C.; Dee, N.; Amama, P. B.; CarpenaNuñez, J.; Shi, W.; Plata, D. L.; Penev, E. S.; Yakobson, B. I.; Balbuena, P. B.; Bichara, C.; Futaba, D. N.; Noda, S.; et al. Carbon Nanotubes and Related Nanomaterials: Critical Advances and Challenges for Synthesis toward Mainstream Commercial Applications. *ACS Nano* **2018**, 12, 11756−11784.

26. Anzar, N.; Hasan, R.; Tyagi, M.; Yadav, N.; Narang, J. Carbon Nanotube - A Review on Synthesis, Properties and Plethora of Applications in the Field of Biomedical Science. *Sens. Int.* **2020**, 1, 100003.
27. Trojanowicz, M. Analytical Applications of Carbon Nanotubes: A Review. TrAC, Trends Anal. Chem. 2006, 25, 480−489.
28. Park, S.; Vosguerichian, M.; Bao, Z. A Review of Fabrication and Applications of Carbon Nanotube Film-Based Flexible Electronics. *Nanoscale* **2013**, 5, 1727−1752.
29. He, H.; Pham-Huy, L. A.; Dramou, P.; Xiao, D.; Zuo, P.; PhamHuy, C. Carbon Nanotubes: Applications in Pharmacy and Medicine. BioMed Res. Int. **2013**, 2013 (2013), e578290.
30. Schnorr, J. M.; Swager, T. M. Emerging Applications of Carbon Nanotubes. *Chem. Mater.* **2011**, 23, 646−657.
31. Kurwadkar, S.; Hoang, T. V.; Malwade, K.; Kanel, S. R.; Harper, W. F.; Struckhoff, G. Application of carbon nanotubes for removal of emerging contaminants of concern in engineered water and wastewater treatment systems. *Nanotechnol. environ. eng.* **2019**, *4*(1), 12.
32. Cho, H.; Kim, J. H.; Hwang, J. H.; Kim, C. S.; Jang, S. G.; Park, C.; Lee, H.; Kim, M. J. Single- and Double-Walled Boron Nitride Nanotubes: Controlled Synthesis and Application for Water Purification. *Sci. Rep.* **2020**, 10 (1), 1-10.
33. Kalay, S.; Yilmaz, Z.; Sen, O.; Emanet, M.; Kazanc, E.; C-ulha, M. Synthesis of Boron Nitride Nanotubes and Their Applications. *Beilstein J. Nanotechnol*. **2015**, 6, 84–102.
34. Wang, J.; Lee, C. H.; Yap, Y. K. Recent advancements in boron nitride nanotubes. *Nanoscale* **2010**, 2 (10), 2028−2034

35. Lee, C. H.; Bhandari, S.; Tiwari, B.; Yapici, N.; Zhang, D.; Yap, Y. K. Boron Nitride Nanotubes: Recent Advances in Their Synthesis, Functionalization, and Applications. *Molecules* **2016**, 21, 922.
36. Iqbal, A.; Saeed, A.; Ul-Hamid, A. A Review Featuring the Fundamentals and Advancements of Polymer/CNT Nanocomposite Application in Aerospace Industry. *Polymer Bulletin* **2020**, 78 (1), 539–557.
37. Jung, H.; Choi, H. K.; Oh, Y.; Hong, H.; Yu, J. Enhancement of Thermo-Mechanical Stability for Nanocomposites Containing Plasma Treated Carbon Nanotubes with an Experimental Study and Molecular Dynamics Simulations. *Sci. Rep.* 2020, 10 (1), 1-10.
38. Hwang, J. Y.; Kim, H. S.; Kim, J. H.; Shin, U. S.; Lee, S. H. Carbon Nanotube Nanocomposites with Highly Enhanced Strength and Conductivity for Flexible Electric Circuits. *Langmuir* **2015**, 31, 7844−7851.
39. Marconnett, A. M.; Yamamoto, N.; Panzer, M. A.; Wardle, B. L.; Goodson, K. E. Thermal Conduction in Aligned Carbon NanotubePolymer Nanocomposites with High Packing Density. *ACS Nano* **2011**, 5, 4818−4825.
40. Zhao, B.; Sivasankar, V. S.; Dasgupta, A.; Das, S. Ultrathin and Ultrasensitive Printed Carbon Nanotube-Based Temperature Sensors Capable of Repeated Uses on Surfaces of Widely Varying Curvatures and Wettabilities. *ACS Appl. Mater. Interfaces* **2021**, *13*(8), 10257-10270.
41. Zhao, B.; Wang, Y.; Sinha, S.; Chen, C.; Liu, D.; Dasgupta, A.; Hu, L.; Das, S. Shape-Driven Arrest of Coffee Stain Effect Drives the Fabrication of Carbon-Nanotube-Graphene-Oxide Inks for Printing Embedded Structures and Temperature Sensors. *Nanoscale* **2019**, 11, 23402−23415.

42. Al-Jumaili, A.; Alancherry, S.; Bazaka, K.; Jacob, M. V. Review on the antimicrobial properties of carbon nanostructures. *Materials* **2017**, 10 (9), 1066.
43. Teixeira-Santos, R.; Gomes, M.; Gomes, L. C.; Mergulhão, F. J. Antimicrobial and anti-adhesive properties of carbon nanotube-based surfaces for medical applications: a systematic review. *Iscience*, **2020** 102001.
44. Li, Y.; Li, Z.; Aydin, F.; Quan, J.; Chen, X.; Yao, Y. C.; Zhan, C.; Chen, Y.; Pham, T. A.; Noy, A. Water-Ion Permselectivity of Narrow-Diameter Carbon Nanotubes. *Sci. Adv.* **2020**, 6, No. eaba9966.
45. Tunuguntla, R. H.; Henley, R. Y.; Yao, Y.-C.; Pham, T. A.; Wanunu, M.; Noy, A. Enhanced Water Permeability and Tunable Ion Selectivity in Subnanometer Carbon Nanotube Porins. *Science* **2017**, *357*, 792−796.
46. Urita, K.; Fujimori, T.; Notohara, H.; Moriguchi, I. Direct Observation of Electrochemical Lithium-Sulfur Reaction inside Carbon Nanotubes. *ACS Appl. Energy Mater*. **2018**, *1*, 807−813.
47. Chakraborty, S.; Kumar, H.; Dasgupta, C.; Maiti, P. K. Confined Water: Structure, Dynamics, and Thermodynamics. *Acc. Chem. Res*. **2017**, *50*, 2139−2146.
48. Alexiadis, A.; Kassinos, S. Molecular Simulation of Water in Carbon Nanotubes. *Chem. Rev.* **2008**, *108*, 5014−5034.
49. Thomas, J. A.; Mcgaughey, A. J. H. Water Flow in Carbon Nanotubes: Transition to Subcontinuum Transport. *Phys. Rev. Lett.* **2009**, *102*, 184502−184505.
50. Joseph, S.; Aluru, N. R. Why Are Carbon Nanotubes Fast Transporters of Water? *Nano Lett*. **2008**, **8**, 452−458.

51. Mann, D. J.; Halls, M. D. Water alignment and proton conduction inside carbon nanotubes. *Phys. Rev. Lett*. **2003**, *90*, 195503.

52. Feng, J. W.; Ding, H. M.; Ma, Y. Q. Water desalination by electrical resonance inside carbon nanotubes. *Phys. Chem. Chem. Phys.* **2016**, *18*(40), 28290-28296.

53. Ohba, T.; Chaban, V. V. A Highly Viscous Imidazolium Ionic Liquid inside Carbon Nanotubes. *J. Phys. Chem. B* **2014**, *118*, 6234− 6240.

54. Sam, A.; Prasad K, V.; Sathian, S. P. Water flow in carbon nanotubes: the role of tube chirality. *Phys. Chem. Chem. Phys*. **2019**, *21*, 6566−6573.

55. Aydin, F.; Moradzadeh, A.; Bilodeau, C. L.; Lau, E. Y.; Schwegler, E.; Aluru, N. R.; Pham, T. A. Ion Solvation and Transport in Narrow Carbon Nanotubes: Effects of Polarizability, Cation− π Interaction, and Confinement. *J. Chem. Theory Comput.* **2021**, *17*, 1596−1605.

56. Oya, Y.; Hata, K.; Ohba, T. Interruption of Hydrogen Bonding Networks of Water in Carbon Nanotubes Due to Strong Hydration Shell Formation. *Langmuir* **2017**, *33*, 11120−11125.

57. Liang, L.; Li, J.-C.; Zhang, L.; Zhang, Z.; Shen, J.-W.; Li, L.; Wu, J. Computer simulation of water desalination through boron nitride nanotubes. *Phys. Chem. Chem. Phys*. **2017**, *19*, 30031.

58. Allard, C.; Schué, L.; Fossard, F.; Recher, G.; Nascimento, R.; Flahaut, E.; Loiseau, A.; Desjardins, P.; Martel, R.; Gaufrès, E. Confinement of Dyes inside Boron Nitride Nanotubes: Photostable and Shifted Fluorescence down to the Near Infrared. *Adv. Mater*. **2020**, *32*(29), p.2001429.

59. Velioğlu, S.; Karahan, H. E.; Goh, K.; Bae, T. H.; Chen, Y.; Chew, J. W. Metallicity-Dependent Ultrafast Water Transport in Carbon Nanotubes. *Small* **2020**, *16*, 1907575.

60. Sahu, P.; Ali, S. M.; Shenoy, K.; Mohan, S. Nanoscopic insights of saline water in carbon nanotube appended filters using molecular dynamics simulations. *Phys. Chem. Chem. Phys.* **2019**, *21*, 8529−8542.

61. Chava, B. S.; Wang, Y.; Sivasankar, V. S.; Das, S. Water-free Localization of Anion at Anode for Small-Concentration Water-in-Salt Electrolytes Confined in Boron-Nitride Nanotube. *Cell Rep. Phys. Sci.* **2020**, *1*, 100246.

62. Chen, Y.; Marty, L.; Bendiab, N. New Light on Molecule–Nanotube Hybrids. *Adv. Mater.* **2019**, *31*, 1902917.

63. Roquelet, C.; Garrot, D.; Lauret, J. S.; Voisin, C.; Roussignol, P.; Delaire, J. A.; Deleporte, E. Quantum Efficiency of Energy Transfer in Noncovalent Carbon Nanotube/porphyrin Compounds. *Appl. Phys. Lett.* **2010**, *97*, 141918.

64. Ernst, F.; Heek, T.; Setaro, A.; Haag, R.; Reich, S. Energy Transfer in Nanotube-Perylene Complexes. *Adv. Funct. Mater.* **2012**, *22*, 3921-3926.

65. Setaro, A.; Adeli, M.; Glaeske, M.; Przyrembel, D.; Bisswanger, T.; Gordeev, G.; Maschietto, F.; Faghani, A.; Paulus, B.; Weinelt, M.; Arenal, R.; Haag, R.; Reich, S. Preserving π-conjugation in Covalently Functionalized Carbon Nanotubes for Optoelectronic Applications. *Nature Commun.* **2017**, *8*, 14281.

66. Krainov, I. V.; Klier, J.; Dimitriev, A. P.; Klyatskaya, S.; Ruben. M.; Wernsdorfer, W.; Gornyi, I. V. Giant Magnetoresistance in Carbon Nanotubes with Single-Molecule Magnets $TbPc_2$. *ACS Nano* **2017**, *11*, 6868-6880.

67. Bogany, L.; Danieli, C.; Biavardi, E.; Bendiab, N.; Barra, A-L.; Dalcanale, E.; Wernsdorfer, W.; Cornia, A. Single-Molecule-Magnet Carbon-Nanotube Hybrids. *Angew. Chem. Int. Ed.* **2009**, *48*, 746-750.

68. Freeley, M.; Attanzio, A.; Cecconello, A.; Amorso, G.; Clement, P.; Fernandez, G.; Gesuele, F.; Palma, M. Tuning the Coupling in Single-Molecule Heterostructures: DNA-Programmed and Reconfigurable Carbon Nanotube-Based Nanohybrids. *Adv. Sci.* **2018**, *5*, 1800596.

69. Ghosh, S.; Patel, N.; Chakrabarti, R. Probing the Salt Concentration Dependent Nucleobase Distribution in a Single-Stranded DNA–Single-Walled Carbon Nanotube Hybrid with Molecular Dynamics. *J. Phys. Chem. B* **2016**, *120*, 455-466.

70. Wang, H.; Zhang, S.; Li, Y.; Wang, W.; Wang, H.; Fu, Z. Defect-induced Formation Mechanism for Boron Nitride Nanosheets-nanotubes Hybrid Structures. *Scripta Material.* **2019**, *171*, 16-20.

71. Mukhopadhyay, S.; Gowtham, S.; Scheicher, R. H.; Pandey, R.; Karna, S. P. Theoretical Study of Physisorption of Nucleobases on Boron Nitride Nanotubes: A New Class of Hybrid Nano-biomaterials. *Nanotechnology* **2010**, *21*, 165703.

72. Yoosefian, M.; Mirhaji, E.; Afshar, M.; Juan, A. Molecular Dynamics Simulations on Interaction of ssDNA-causing DM1 with Carbon and Boron Nitride Nanotubes to Inhibit the Formation of CTG Repeat Secondary Structures. *Appl. Surf. Sci.* **2020**, *524*, 146572.

73. Saleh, D. A.; Niskanen, J.; Xue, Y.; Golberg, D.; Winnik, F. M.; Sosnik, A. Boron Nitride Nanotube-based Amphiphilic Hybrid Nanomaterials for Superior Encapsulation of Hydrophobic Cargos. *Mater. Today Chem.* **2017**, *6*, 45-60.

74. Nakanishi, R.; Satoh, J.; Katoh, K.; Zhang, H.; Breedlove, B. K.; Nishijima, M.; Nakanishi, Y.; Omachi, H.; Shinohara, H.; Yamashita, M. $DySc_2N@C_{80}$ Single-Molecule Magnetic Metallofullerene Encapsulated in a Single-Walled Carbon Nanotube. *J. Am. Chem. Soc.* **2018**, *140*, 10955-10959.

75. Giménez-López, M. C.; Moro, F.; Torre, A. L.; Gómez-García, C. J.; Brown, P. D.; van Slageren, J.; Khlobystov, A. N. Encapsulation of Single-molecule Magnets in Carbon Nanotubes. *Nature Comm.* **2011**, *2*, 407.

76. Cambre, S.; Campo, J.; Beirnaert, C.; Verlackt, C.; Cool, P.; Wenseleers, W. Asymmetric Dyes Align inside Carbon Nanotubes to Yield a Large Nonlinear Optical Response. *Nature Nanotechnol.* **2015**, *10*, 248-252.

77. Liu, S.; Yao, M.; Ma, F.; Liu, B.; Yao, Z.; Liu, R.; Cui, T.; Liu, B. High Energetic Polymeric Nitrogen Stabilized in the Confinement of Boron Nitride Nanotube at Ambient Conditions *J. Phys. Chem. C* **2016**, *120*, 16412-16417.

78. Gracia-Espino, E.; Barzegar, H. R.; Zettl, A. Coronene-Based Graphene Nanoribbons Insulated by Boron Nitride Nanotubes: Electronic Properties of the Hybrid Structure. *ACS Omega* **2018**, *3*, 12930-12935.

79. Liu, Y.; Wang, Q.; Zhang, L.; Wu, T. Dynamics and Density Profile of Water in Nanotubes as One-Dimensional Fluid. *Langmuir* **2005**, *21*, 12025-12030.

80. Takaiwa, D.; Hatanu, I; Koga, K.; Tanaka, H. Phase Diagram of Water in Carbon Nanotubes. *Proc. Natl. Acad. Sci. USA* **2008**, *105*, 39-43.

81. Alexiadis, A.; Kassinos, S.; The Density of Water in Carbon Nanotubes. *Chem. Eng. Sci.* **2008**, *63*, 2047-2056.

82. Abe, H.; Takekiyo, T.; Yoshimura, Y.; Shimizu, A. Static and Dynamic Properties of Nano-confined Water in Room-temperature Ionic Liquids. *J. Molecular Liquid.* **2019**, *290*, 111216.

83. Mochizuki, K.; Koga, K. Solid-Liquid Critical Behavior of Water in Nanopores. *Proc. Natl. Acad. Sci. USA* **2015**, 112, 8221-8226.

84. Plimpton, S. Fast Parallel Algorithms for Short-Range Molecular Dynamics. *J. Comput. Phys*. **1995**, *117*, 1-19.

85. Hoover, W. G. Canonical Dynamics: Equilibrium Phase-Space Distributions. *Phys. Rev. A* **1985**, *31*, 1695-1697.

86. Nose´, S. A Unified Formulation of the Constant Temperature Molecular Dynamics Methods. *J. Chem. Phys.* **1984**, *81*, 511-519.

87. Lopes, J. N. C.; Pádua, A. A. CL&P: A Generic and Systematic Force Field for Ionic Liquids Modeling. *Theor. Chemistry Accounts* **2012**, *131*, 1129.

88. Berendsen, H. J. C.; Grigera, J. R.; Straatsma, T. P. The Missing Term in Effective Pair Potentials. *J. Phys. Chem.* **1987**, *91*, 6269-6271.

89. Tersoff, J. New Empirical Approach for the Structure and Energy of Covalent Systems. *Phys. Rev. B* **1988**, *37*, 6991-7000.

90. Kınacı, A.; Haskins, J. B.; Sevik, C.; Çağın, T. Thermal Conductivity of BN-C Nanostructures. *Phys. Rev. B* **2012**, *86*, 115410.

91. Won, C. Y.; Aluru, N. R. Water Permeation through a Subnanometer Boron Nitride Nanotube. *J. Am. Chem. Soc.* **2007**, *129*, 2748-2749.

92. R. W. Hockney and J. W. Eastwood, Computer Simulations Using Particles. New York: McGraw-Hill International Book Co **1981.**

93. Humphrey, W.; Dalke, A.; Schulten, K. VMD - Visual Molecular Dynamics. *J. Mol. Graphics* **1996**, *14*, 33-38.

94. A. Grossfield, *WHAM: The Weighted Histogram Analysis Method*, http://membrane.urmc.rochester.edu/content/wham, version 2.0.9.

95. Kumar, S.; Bouzida, D.; Swendsen, R. H.; Kollman, P. A.; Rosenberg, J. M. The Weighted Histogram Analysis Method for FreeEnergy Calculations on Biomolecules 0.1. *The Method. J. Comput. Chem*. **1992**, 13, 1011−1021.

96. Dubouis, N.; Park, C.; Deschamps, M.; Abdelghani-Idrissi, S.; Kanduc, M.; Colin, A.; Salanne, M.; Dzubiella, J.; Grimaud, A.;ˇRotenberg, B. Chasing aqueous biphasic systems from simple salts by exploring the LiTFSI/LiCl/H2O phase diagram. ACS Cent. Sci. 2019, 5, 640−643.

97. McEldrew, M.; Goodwin, Z. A. H.; Kornyshev, A. A.; Bazant, M. Z. Theory of the Double Layer in Water-in-Salt Electrolytes. J. Phys. Chem. Lett. 2018, 9, 5840−5846.

98. Han, S. Anionic effects on the structure and dynamics of water in superconcentrated aqueous electrolytes. RSC Adv. 2019, 9, 609− 619.

99. Largeot, C.; Portet, C.; Chmiola, J.; Taberna, P.; Gogotsi, Y.; Simon, P. Relation between the Ion Size and Pore Size for an Electric Double-Layer Capacitor. J. Am. Chem. Soc. 2008, 130, 2730−2731.

100. Stukowski, A. Visualization and Analysis of Atomistic Simulation Data with OVITO - the Open Visualization Tool. *Modelling Simul. Mater. Sci. Eng.* **2010**, *18*, 015012.

101. Bazant, M. Z.; Storey, B. D.; Kornyshev, A. A. Double Layer in Ionic Liquids: Overscreening versus Crowding. *Phys. Rev. Lett*. **2011**, *106*, 046102.

102. Mezger, M.; Schroder, H.; Reichert, H.; Schramm, S.; Okasinski, J. S.; Schoder, S.; Honkimaki, V.; Deutsch, M.; Ocko, B. M.; Ralston, J.; Rohwerder, M.; Stratmann, M.; Dosch, H. Molecular Layering of Fluorinated Ionic Liquids at a Charged Sapphire(0001) Surface. *Science* **2008**, *322*, 424−428.

103. Coles, S. W.; Park, C.; Nikam, R.; Kanduc, M.; Dzubiella, J.; Rotenberg, B. Correlation Length in Concentrated Electrolytes: Insights from All-Atom Molecular Dynamics Simulations. *J. Phys. Chem. B* **2020**, *124*, 1778−1786.

104. Smith, A. M.; Lee, A. A.; Perkin, S. The Electrostatic Screening Length in Concentrated Electrolytes Increases with Concentration. *J. Phys. Chem. Lett*. **2016**, *7*, 2157−2163.

105. Suo, L.; Borodin, O.; Sun, W.; Fan, X.; Yang, C.; Wang, F.; Gao, T.; Ma, Z.; Schroeder, M.; von Cresce, A.; et al. (2016) Advanced HighVoltage Aqueous Lithium-Ion Battery Enabled by ″Water-in-Bisalt″ Electrolyte. *Angew. Chem., Int. Ed., 55*, 7136−7141.

106. Yamada, Y.; Usui, K.; Sodeyama, K.; Ko, S.; Tateyama, Y.; Yamada, A. (2016) Hydrate-Melt Electrolytes for High-Energy-Density Aqueous Batteries. *Nature Energy*, *1*, 16129.

107. Suo, L.; Borodin, O.; Wang, Y.; Rong, X.; Sun, W.; Fan, X.; Xu, S.; Schroeder, M. A.; Cresce, A. V.; Wang, F.; Yang, C.; Hu, Y.-S.; Xu, K.; Wang, C. (2017) Water-in-Salt" Electrolyte Makes Aqueous Sodium-Ion Battery Safe, Green, and Long-Lasting. *Adv. Energy Mater*., 1701189.

108. Reber, D.; Figi, R.; Kühnel, R. S.; Battaglia, C. (2019) Stability of Aqueous Electrolytes Based on LiFSI and NaFSI. *Electrochim. Acta*, *321*, 134644.

109. Kühnel, R.-S.; Reber, D.; Battaglia, C. (2017) A High-Voltage Aqueous Electrolyte for Sodium-Ion Batteries. *ACS Energy Lett.*, *2*, 2005− 2006.

110. Bu, X.; Su, L.; Dou, Q.; Lei, S.; Yan, X. (2019) A Low-Cost "Water-in-Salt" Electrolyte for a 2.3 V High-Rate Carbon-Based Supercapacitor. *J. Mater. Chem. A*, *7*, 7541−7547.

111. Zheng, J.; Tan, G.; Shan, P.; Liu, T.; Hu, J.; Feng, Y.; Yang, L.; Zhang, M.; Chen, Z.; Lin, Y.; Lu, J.; Neuefeind, Joerg C.; Ren, Y.; Amine, K.; Wang, L.-W.; Xu, K.; Pan, F. (2018**)** Understanding Thermodynamic and Kinetic Contributions in Expanding the Stability Window of Aqueous Electrolytes. *Chem*, *4*, 2872−2882.

112. Guo, J.; Ma, Y.; Zhao, K.; Wang, Y.; Yang, B.; Cui, J.; Yan, X. (2019) High-Performance and Ultra-Stable Aqueous Supercapacitors Based on a Green and Low-Cost Water-In-Salt Electrolyte. *ChemElectroChem, 6* (21), 5433–5438.

113. Han, J.; Zhang, H.; Varzi, A.; Passerini, S. (2018) Fluorine-Free Water-in-Salt Electrolyte for Green and Low-Cost Aqueous Sodium-Ion Batteries. *ChemSusChem, 11* (21), 3704–3707.

114. Lukatskaya, M. R.; Feldblyum, J. I.; Mackanic, D. G.; Lissel, F.; Michels, D. L.; Cui, Y.; Bao, Z. (2018) Concentrated Mixed Cation Acetate "Water-in-Salt" Solutions as Green and Low Cost High Voltage Electrolytes for Aqueous Batteries. *Energy Environ. Sci*., *3*, 373− 374.

115. Zhang, C.; Holoubek, J. J.; Wu, X.; Daniyar, A.; Zhu, L.; Chen, C.; Leonard, D. P.; Rodríguez-Perez, I. A.; Jiang, J.-X.; Fang, C.; Ji, X. (2018) A $ZnCl_2$ Water-in-Salt Electrolyte for Reversible Zn Metal Anode. *Chem. Commun*., *54*, 14097−14099.

116. Azov, V. A.; Egorova, K. S.; Seitkalieva, M. M.; Kashin, A. S.; Ananikov, V. P. (2018) "Solvent-in-salt" Systems for Design of New Materials in Chemistry, Biology and Energy Research. *Chem. Soc. Rev*., *47*, 1250−1284.

117. Suo, L.; Hu, Y.-S.; Li, H.; Armand, M.; Chen, L. (2013**)** A New Class of Solvent-in-Salt Electrolyte for High-Energy Rechargeable Metallic Lithium Batteries. *Nat. Commun.*, *4*, 1481.

118. Taggougui, M.; Diaw, M.; Carre, B.; Willmann, P.; Lemordant, D. (2008) Solvents in Salt Electrolyte: Benefits and Possible Use as Electrolyte for Lithium-Ion Battery. Electrochim. Acta, 53, 5496−5502.

119. Angell, C. A. (1965**)** Electrical Conductance of Concentrated Aqueous Solutions and Molten Salts: Correlation through Free Volume Transport Model. J. Phys. Chem., 69, 2137.

120. Angell, C. A. (1965) A New Class of Molten Salt Mixtures The Hydrated Dipositive Ion as an Independent Cation Species. J. Electrochem. Soc., 112 (12), 1224−1227.

121. Marcus, Y. (2016) Ionic liquid properties from molten salts to RTILs; Springer Nature: Cham, Switzerland.

122. Yamada, Y.; Wang, J.; Ko, S.; Watanabe, E.; Yamada, A. (2019) Advances and Issues in Developing Salt-Concentrated Battery Electrolytes. Nat. Energy, 4, 269−280.

123. Jiang, L.; Liu, L.; Yue, J.; Zhang, Q.; Zhou, A.; Borodin, O.; Suo, L.; Li, H.; Chen, L.; Xu, K.; et al. (2020) High-Voltage Aqueous Na-Ion Battery Enabled by Inert-Cation-Assisted Water-in-Salt Electrolyte. *Adv. Mater.*, *32* (2), 1–10.

124. Zhang, H.; Jeong, S.; Qin, B.; Carvalho, D. V.; Buchholz, D.; Passerini, S. (2018) Towards High-performance Aqueous Sodium-Ion Batteries: Stabilizing the Solid/Liquid Interface for NASICON-Type Na2VTi(PO4)3 Using Concentrated Electrolytes. *ChemSusChem*, *11*, 1382−1389.

125. Nakamoto, K.; Sakamoto, R.; Sawada, Y.; Ito, M.; Okada, S. (2018) Over 2 V Aqueous Sodium-Ion Battery with Prussian Blue-Type Electrodes. *Small Methods*, No. 1800220.

126. Yang, C.; Chen, J.; Qing, T.; Fan, X.; Sun, W.; von Cresce, A.; Ding, M. S.; Borodin, O.; Vatamanu, J.; Schroeder, M. A.; Eidson, N.; Wang, C.; Xu, K. (2017) 4.0 V Aqueous Li-Ion Batteries. *Joule*, *1*, 122− 132.

127. Wang, F.; Borodin, O.; Ding, M. S.; Gobet, M.; Vatamanu, J.; Fan, X.; Gao, T.; Edison, N.; Liang, Y.; Sun, W.; et al. (2018) Hybrid Aqueous/Non-aqueous Electrolyte for Safe and High-Energy Li-Ion Batteries. *Joule, 2*, 927−937.

128. Zhi, C. Y.; Bando, Y.; Terao, T.; Tang, C. C.; Kuwahara, H.; Golberg, D. (2009) Towards Thermoconductive, Electrically Insulating Polymeric Composites with Boron Nitride Nanotubes as Fillers. *Adv. Funct. Mater*., *19*, 1857−1862.

129. Chopra, N. G.; Luyken, R. J.; Cherrey, K.; Crespi, V. H.; Cohen, M. L.; Louie, S. G.; Zettl, A. (1995) Boron nitride nanotubes. *Science*, *269*, 966−967.

130. Jarvis, C. R.; Lain, M. J.; Yakovleva, M. V.; Gao, Y. (2006) A Prelithiated Carbon Anode for Lithium-Ion Battery Applications. *J. Power Sources*, *162*, 800−802.

131. Watanabe, T.; Tsuda, T.; Ando, N.; Nakamura, S.; Hayashi, N.; Soma, N.; Gunji, T.; Ohsaka, T.; Matsumoto, F. (2019) An improved pre-lithiation of graphite anodes using through-holed cathode and anode electrodes in a laminated lithium ion battery. *Electrochimica Acta*, *324*, 134848.

132. Holtstiege, F.; Koc, T.; Hundehege, T.; Siozios, V.; Winter, M.; ¸Placke, T. (2018) Toward High Power Batteries: Pre-lithiated Carbon Nanospheres as High Rate Anode Material for Lithium Ion Batteries. *ACS Appl. Energy Mater*., *1*, 4321−4331.

133. Liu, N. A.; Hu, L. B.; McDowell, M. T.; Jackson, A.; Cui, Y. (2011) Prelithiated Silicon Nanowires as an Anode for Lithium Ion Batteries. *ACS Nano*, *5*, 6487 −6493.

134. Yan, Y.; Yin, Y.-X.; Xin, S.; Su, J.; Guo, Y.-G.; Wan, L.-J. (2013) High-Safety Lithium-Sulfur Battery with Prelithiated Si/C Anode and Ionic Liquid Electrolyte. *Electrochim. Acta*, *91*, 58−61

135. Vatamanu, J.; Borodin, O. (2017) Ramifications of Water-in-Salt Interfacial Structure at Charged Electrodes for Electrolyte Electrochemical Stability. *J. Phys. Chem. Lett.*, *8*, 4362−4367.

136. Li, Z.; Jeanmairet, G.; Mendez-Morales, T.; Rotenberg, B.; Salanne, M. (2018) Capacitive Performance of Water-in-Salt Electrolyte in Supercapacitors: A Simulation Study. *J. Phys. Chem. C*, *122*, 23917.

137. Reed, S. K.; Lanning, O. J.; Madden, P. A. (2007) Electrochemical interface between an ionic liquid and a model metallic electrode. *J. Chem. Phys.*, *126*, 084704.

138. Gingrich, T. R.; Wilson, M. (2010) On the Ewald Summation of Gaussian Charges for the Simulation of Metallic Surfaces. *Chem. Phys. Lett.*, *500*, 178−183.

139. Wang, Z.; Yang, Y.; Olmsted, D.; Asta, M.; Laird, B. (2014) Evaluation of the constant potential method in simulating electric double-layer capacitors. *J. Chem. Phys.*, *141*, 184102.

140. Jorgensen, W. L.; Maxwell, D. S.; Tirado-Rives, J. (1996**)** Development and Testing of the OPLS All-Atom Force Field on Conformational Energetics and Properties of Organic Liquids. *J. Am. Chem. Soc.*, *118*, 11225.

141. Sparreboom, W.; van den Berg, A.; Eijkel, J. C. T. Principles and Applications of Nanofluidic Transport. *Nature Nanotech.* **2009**, *4*, 713-720.

142. Haywood, D. G.; Saha-Shah, A.; Baker, L. A.; Jacobson, S. C. Fundamental Studies of Nanofluidics: Nanopores, Nanochannels, and Nanopipets. *Anal. Chem.* **2015**, *87*, 172-187.

143. Xu, Y. Nanofluidics: A New Arena for Materials Science. *Adv. Mater.* **2018**, *30*, 1702419.

144. Schoch, R. B.; Han, J.; Renaud, P. Transport Phenomena in Nanofluidics. *Rev. Mod. Phys.* **2008**, *80*, 839.

145. Sparreboom, W.; van den Berg, A.; Eijkel, J. C. T. Transport in Nanofluidic Systems: A Review of Theory and Applications. *New J. Phys.* **2010**, *12*, 015004.

146. Zhang, D.; Zhang, X. Bioinspired Solid-State Nanochannel Sensors: From Ionic Current Signals, Current, and Fluorescence Dual Signals to Faraday Current Signals. *Small* **2021**, *17*, 2100495.

147. Huang, Y.; Zhang, W.; Xia, F.; Jiang, L. Solid-State Nanochannel-Based Sensing Systems: Development, Challenges, and Opportunities. *Langmuir* **2022**, *38*, 2415-2422.

148. Wu, Y.; Fu, C. F.; Huang, Q.; Zhang, P.; Cui, P.; Ran, J.; Yang, J.; Xu, T. 2D Heterostructured Nanofluidic Channels for Enhanced Desalination Performance of Graphene Oxide Membranes. *ACS Nano* **2021**, *15*, 7586-7595.

149. Gong, D.; Yin, Y.; Chen, H.; Guo, B.; Wu, P.; Wang, Y.; Yang, Y.; Li, Z.; He, Y.; Zeng, G. Interfacial Ions Sieving for Ultrafast and Complete Desalination through 2D Nanochannel Defined Graphene Composite Membranes. ACS Nano **2021**, *15*, 9871-9881.

150. Itoh, Y.; Chen, S.; Hirahara, R.; Konda, T.; Aoki, T.; Ueda, T.; Shimada, I.; Cannon, J. J.; Shao, C.;Shiomi, J.; Tabata, K. V.; Noji, H.; Sato, K.; Aida, T. Ultrafast

Water Permeation Through Nanochannels with a Densely Fluorous Interior surface. *Science* **2022**, *376*, 738-743.

151. Chen, F.; Gong, A. S.; Zhu, M.; Chen, G.; Lacey, S. D.; Jiang, F.; Li, Y.; Wang, Y.; Dai, J.; Yao, Y.; Song, J.; Liu, B.; Fu, K.; Das, S.; Hu, L. Mesoporous, Three-Dimensional Wood Membrane Decorated with Nanoparticles for Highly Efficient Water Treatment. *ACS Nano* **2017**, *11*, 4275-4282.

152. Arora, B.; Attri, P. Carbon Nanotubes (CNTs): A Potential Nanomaterial for Water Purification. *J. Composites Sci.* **2020**, *4*, 135.

153. Zhang, Z.; Wen, L.; Jiang, L. Nanofluidics for Osmotic Energy Conversion. *Nature Rev. Mater.* **2021**, *6*, 622-639.

154. Li, T., Zhang, X., Lacey, S. D., Mi, R., Zhao, X., Jiang, F., Song, J.; Liu, Z.; Chen, G.; Dai, J.; Yao, Y.; Das, S.; Yang, R.; Briber, R. M.; Hu, L. Cellulose Ionic Conductors with High Differential Thermal Voltage for Low-Grade Heat Harvesting. *Nature Mater.* **2019**, *18*, 608-613.

155. Whitby, M.; Quirke, N. Fluid Flow in Carbon Nanotubes and Nanopipes. *Nature Nanotech.* **2007**, *2*, 87-94.

156. Kavokine, N.; Netz, R. R.; Bocquet, L. Fluids at the Nanoscale: From Continuum to Subcontinuum Transport. *Annu. Rev. Fluid Mech.* **2021**, *53*, 377-410.

157. Majumder, M.; Chopra, N.; Andrews, R.; Hinds, B. J. Enhanced Flow in Carbon Nanotubes. *Nature* **2005**, *438*, 44.

158. Secchi, E.; Marbach, S.; Niguès, A.; Stein, D.; Siria, A.; Bocquet, L. Massive Radius-Dependent Flow Slippage in Carbon Nanotubes. *Nature* **2016**, *537*, 210-213.

159. Arai, N.; Koishi, T.; Ebisuzaki, T. Nanotube Active Water Pump Driven by Alternating Hydrophobicity. ACS Nano **2021**, *15*, 2481-2489.

160. Ihsanullah. Carbon Nanotube Membranes for Water Purification: Developments, Challenges, and Prospects for the Future. *Separation Purification Tech.* **2019**, *209*, 307-337.

161. Oyarzua, E.; Walther, J. H.; Megaridis, C. M.; Koumoutsakos, P.; Zambrano, H. A. Carbon Nanotubes as Thermally Induced Water Pumps. ACS Nano **2017**, *11*, 9997-10002.

162. Maselugbo, A. O.; Harrison, H. B.; Alston, J. R. Boron Nitride Nanotubes: A Review of Recent Progress on Purification Methods and Techniques. *J. Mater. Res.* **2022**, *37*, 4438-4458.

163. Zhang, L.; Jia, L.; Zhang, J.; Li, J.; Liang, L.; Kong, Z.; Shen, J-W.; Wang, X.; Zhang, W.; Wang, H. Understanding the Effect of Chemical Modification on Water Desalination in Boron Nitride Nanotubes via Molecular Dynamics Simulation. *Desalination* **2019**, *464*, 84-93.

164. Thiemann, F. L.; Schran, C.; Rowe, P.; Müller, E. A.; Michaelides, A. Water Flow in Single-Wall Nanotubes: Oxygen Makes It Slip, Hydrogen Makes It Stick. *ACS Nano* **2022**, *16*, 10775-10782.

165. Mistry, S.; Pillai, R.; Mattia, D.; Borg, M. K. Untangling the Physics of Water Transport in Boron Nitride Nanotubes. *Nanoscale* **2021**, *13*, 18096-18102.

166. Casanova, S.; Mistry, S.; Mazinani, S.; Borg, M. K.; Chew, Y. J.; Mattia, D. Enhanced Nanoparticle Rejection in Aligned Boron Nitride Nanotube Membranes. *Nanoscale* **2020**, *12*, 21138-21145.

167. Chava, B. S.; Wang, Y.; Das, S. Boron Nitride Nanotube–Salt–Water Hybrid: Toward Zero-Dimensional Liquid Water and Highly Trapped Immobile Single Anions Inside One-Dimensional Nanostructures. *J. Phys. Chem. C* **2021**, *125*, 14006-14013.

168. Won, C. Y.; Aluru, N. R. Water Phase Transition Induced by a Stone-Wales Defect in a Boron Nitride Nanotube. *J. Am. Chem. Soc.* **2008**, *130*, 13649-13652.

169. Pascal, T. A.; Goddard, W. A.; & Jung, Y. Entropy and the Driving Force for the Filling of Carbon Nanotubes with Water. *Proc. Natl. Acad. Sci. USA* **2011**, *108*, 108(29), 11794-11798.

170. Matsumoto, R. A., Thompson, M. W., Vuong, V. Q., Zhang, W., Shinohara, Y., van Duin, A. C., Kent, P. R. C.; Irle, S.; Egami, T.; Cummings, P. T. Investigating the Accuracy of Water Models through the Van Hove Correlation Function. *J. Chem. Theory Comput.* **2021**, *17*, 5992-6005.

171. van Duin, A. C.; Dasgupta, S.; Lorant, F.; Goddard, W. A. ReaxFF: A Reactive Force Field for Hydrocarbons. *J. Phys. Chem. A* **2001**, *105*, 9396-9409.

172. Aktulga, H. M.; Fogarty, J. C.; Pandit, S. A.; Grama, A. Y. Parallel Reactive Molecular Dynamics: Numerical Methods and Algorithmic Techniques. *Parallel Computing* **2012**, *38*, 245-259.

173. Rappe, A. K.; Goddard III, W. A. Charge Equilibration for Molecular Dynamics Simulations. *J. Phys. Chem.* **1991**, *95*, 3358-3363.

174. Lin, S. T.; Maiti, P. K.; Goddard III, W. A. Two-Phase Thermodynamic Model for Efficient and Accurate Absolute Entropy of Water from Molecular Dynamics Simulations. *J. Phys. Chem. B* **2010**, *114*, 8191-8198.

175. Soper, A. K. The Excluded Volume Effect in Confined Fluids and Liquid Mixtures. *J. Phys. Cond. Matt.* **1997**, *9*, 2399.

176. Hartnig, C.; Witschel, W.; Spohr, E.; Gallo, P.; Ricci, M. A.; Rovere, M. Modifications of the Hydrogen Bond Network of Liquid Water in a Cylindrical SiO_2 Pore. *J. Molecular Liq.* **2000**, *85*, 127-137.

177. Glatter, O.; Kratky, O.; Kratky, H. C. (Eds.). Small Angle X-ray Scattering. Academic press, 1982.

178. Manzano, H.; Zhang, W.; Raju, M.; Dolado, J. S.,;López-Arbeloa, I.; van Duin, A. C. Benchmark of ReaxFF Force Field for Subcritical and Supercritical Water. *J. Chem. Phys.* **2018**, *148*, 234503.

179. Chenoweth, K.; van Duin, A. C.; Goddard, W. A. ReaxFF Reactive Force Field for Molecular Dynamics Simulations of Hydrocarbon Oxidation. *J. Phys. Chem. A* **2008**, *112*, 1040-1053.

180. Lamoureux, G.; Roux, B. Modeling Induced Polarization with Classical Drude Oscillators: Theory and Molecular Dynamics Simulation Algorithm J. Chem. Phys. **2003**, 119 (6) 3025– 3039.

181. Verma, A. K.; Rajan, A. G. Surface Roughness Explains the Observed Water Contact Angle and Slip Length on 2D Hexagonal Boron Nitride. *Langmuir* **2022**, *38*, 9210-9220.

182. Rajan, A. G.; Strano, M. S.; Blankschtein, D. Liquids with Lower Wettability Can Exhibit Higher Friction on Hexagonal Boron Nitride: The Intriguing Role of Solid–Liquid Electrostatic Interactions. *Nano Lett.* **2019**, *19*, 1539-1551.

183. Wu, Y.; Wagner, L. K.; Aluru, N. R. Hexagonal Boron Nitride and Water Interaction Parameters. *J. Chem. Phys.* **2016**, *144*, 164118.

184. Tocci, G.; Joly, L.; Michaelides, A. (2014). Friction of Water on Graphene and Hexagonal Boron Nitride from Ab Initio Methods: Very Different Slippage Despite Very Similar Interface Structures. *Nano Lett.* **2014**, *14*, 6872-6877.

185. Al-Hamdani, Y. S.; Ma, M.; Alfè, D.; von Lilienfeld, O. A.; Michaelides, A. Communication: Water on Hexagonal Boron Nitride from Diffusion Monte Carlo. *J. Chem. Phys.* **2015**, *142*, 181101.

186. Ohto, T.; Tada, H.; Nagata, Y. Structure and Dynamics of Water at Water–Graphene and Water–Hexagonal Boron-Nitride Sheet Interfaces Revealed by Ab Initio Sum-Frequency Generation Spectroscopy. *Phys. Chem. Chem. Phys.* **2018**, *20*, 12979-12985.

187. Hummer, G.; Rasaiah, J. C.; Noworyta, J. P. Water Conduction through the Hydrophobic Channel of a Carbon Nanotube. *Nature* **2001**, *414*, 188-190.

188. Mukherjee, B.; Maiti, P. K.; Dasgupta, C.; Sood, A. K. Jump Reorientation of Water Molecules Confined in Narrow Carbon Nanotubes J. Phys. Chem. B **2009**, 113, 10322– 10330.

189. Misra, R. P.; Blankschtein, D. Insights on the Role of Many-Body Polarization Effects in the Wetting of Graphitic Surfaces by Water. *J. Phys. Chem. C* **2017**, *121*, 28166-28179.

190. Rasaiah, J. C., Garde, S., & Hummer, G. (2008). Water in nonpolar confinement: From nanotubes to proteins and beyond. Annu. Rev. Phys. Chem., 59, 713-740.

191. Lynch, C. I., Rao, S., & Sansom, M. S. (2020). Water in nanopores and biological channels: A molecular simulation perspective. Chemical reviews, 120(18), 10298-10335.

192. Sirkin, Y. P., Tagliazucchi, M., & Szleifer, I. J. M. T. A. (2020). Transport in nanopores and nanochannels: some fundamental challenges and nature-inspired solutions. Materials Today Advances, 5, 100047.

193. Zhu, Z., Wang, D., Tian, Y., & Jiang, L. (2019). Ion/molecule transportation in nanopores and nanochannels: From critical principles to diverse functions. Journal of the American Chemical Society, 141(22), 8658-8669.

194. Chava, B. S., Wang, Y., Sivasankar, V. S., & Das, S. (2020). Water-free Localization of Anion at Anode for Small-Concentration Water-in-Salt Electrolytes Confined in Boron-Nitride Nanotube. Cell Reports Physical Science, 1(11), 100246.

195. Sachar, H. S., Chava, B. S., Pial, T. H., & Das, S. (2021). All-Atom Molecular Dynamics Simulations of the Temperature Response of Densely Grafted Polyelectrolyte Brushes. *Macromolecules*, *54*(13), 6342-6354.

196. Dong, Q., Zhang, X., Qian, J., He, S., Mao, Y., Brozena, A. H., ... & Hu, L. (2022). A cellulose-derived supramolecule for fast ion transport. *Science Advances*, *8*(49), eadd2031.

197. Sachar, H. S., Pial, T. H., Chava, B. S., & Das, S. (2020). All-atom molecular dynamics simulations of weak polyionic brushes: influence of charge density on the properties of polyelectrolyte chains, brush-supported counterions, and water molecules. *Soft Matter*, *16*(33), 7808-7822.

198. Agrawal, K. V., Shimizu, S., Drahushuk, L. W., Kilcoyne, D., & Strano, M. S. (2017). Observation of extreme phase transition temperatures of water confined inside isolated carbon nanotubes. Nature nanotechnology, 12(3), 267-273.

199. Knight, A. W., Kalugin, N. G., Coker, E., & Ilgen, A. G. (2019). Water properties under nano-scale confinement. Scientific reports, 9(1), 8246.

200. Byl, O., Liu, J. C., Wang, Y., Yim, W. L., Johnson, J. K., & Yates, J. T. (2006). Unusual hydrogen bonding in water-filled carbon nanotubes. Journal of the American Chemical Society, 128(37), 12090-12097.

201. Dalla Bernardina, S., Paineau, E., Brubach, J. B., Judeinstein, P., Rouzière, S., Launois, P., & Roy, P. (2016). Water in carbon nanotubes: the peculiar hydrogen bond network revealed by infrared spectroscopy. Journal of the American Chemical Society, 138(33), 10437-10443.

202. Sachar, H. S., Chava, B. S., Pial, T. H., & Das, S. (2021). Hydrogen bonding and its effect on the orientational dynamics of water molecules inside polyelectrolyte brush-induced soft and active nanoconfinement. Macromolecules, 54(4), 2011-2021.

203. de Freitas, D. N., Mendonça, B. H., Köhler, M. H., Barbosa, M. C., Matos, M. J., Batista, R. J., & de Oliveira, A. B. (2020). Water diffusion in carbon nanotubes under directional electric frields: Coupling between mobility and hydrogen bonding. Chemical Physics, 537, 110849.

204. Chen, Q., Wang, Q., Liu, Y. C., & Wu, T. (2014). The effect of hydrogen bonds on diffusion mechanism of water inside single-walled carbon nanotubes. The Journal of chemical physics, 140(21), 214507.

205. Barati Farimani, A., & Aluru, N. R. (2011). Spatial diffusion of water in carbon nanotubes: from fickian to ballistic motion. The Journal of Physical Chemistry B, 115(42), 12145-12149.

206. Wu, M., Wei, W., Liu, X., Liu, K., & Li, S. (2019). Structure and dynamic properties of stretched water in graphene nanochannels by molecular dynamics simulation: effects of stretching extent. Physical Chemistry Chemical Physics, 21(35), 19163-19171.

207. Duan, H., Ying, Z., Tian, L., Cheng, Y., & Shi, L. (2022). Aqueous Proton Transportation in Graphene-Based Nanochannels. Langmuir, 38(49), 15413-15421.

208. Ishii, Y., Matubayasi, N., Watanabe, G., Kato, T., & Washizu, H. (2021). Molecular insights on confined water in the nanochannels of self-assembled ionic liquid crystal. Science Advances, 7(31), eabf0669.

209. Clark II, J. K., & Paddison, S. J. (2014). Ab initio molecular dynamics simulations of water and an excess proton in water confined in carbon nanotubes. *Physical Chemistry Chemical Physics*, 16(33), 17756-17769.

210. Chava, B. S., Chandel, G. R., & Das, S. (2023). Water-Structure-Specific Entropic Dominance in the Filling of Boron Nitride Nanotubes. *The Journal of Physical Chemistry C*, *127*(14), 7009–7018.

211. Wernet, P., Nordlund, D., Bergmann, U., Cavalleri, M., Odelius, M., Ogasawara, H., ... & Nilsson, A. (2004). The structure of the first coordination shell in liquid water. *Science*, *304*(5673), 995-999.

212. Luzar, A., & Chandler, D. (1996). Hydrogen-bond kinetics in liquid water. *Nature*, *379*(6560), 55-57.

213. Luzar, A., & Chandler, D. (1996). Effect of environment on hydrogen bond dynamics in liquid water. *Physical review letters, 76*(6), 928.

214. Kumar, R., Schmidt, J. R., & Skinner, J. L. (2007). Hydrogen bonding definitions and dynamics in liquid water. *The Journal of chemical physics*, *126*(20), 05B611.

215. Van der Spoel, D., van Maaren, P. J., Larsson, P., & Tîmneanu, N. (2006). Thermodynamics of hydrogen bonding in hydrophilic and hydrophobic media. *The Journal of Physical Chemistry B, 110*(9), 4393-4398.

216. Zaman, W., Matsumoto, R. A., Thompson, M. W., Liu, Y. H., Bootwala, Y., Dixit, M. B., ... & Hatzell, K. B. (2021). In situ investigation of water on MXene interfaces. Proceedings of the National Academy of Sciences, 118(49), e2108325118.

217. Ma, X., Zhu, X., Huang, C., & Fan, J. (2022). Revealing the effects of terminal groups of MXene on the water desalination performance. Journal of Membrane Science, 647, 120334.

218. Sun, Y., Zhan, C., Kent, P. R., Naguib, M., Gogotsi, Y., & Jiang, D. E. (2019). Proton redox and transport in MXene-confined water. ACS applied materials & interfaces, 12(1), 763-770.

219. Hong, S., Ming, F., Shi, Y., Li, R., Kim, I. S., Tang, C. Y., ... & Wang, P. (2019). Two-dimensional Ti3C2T x MXene membranes as nanofluidic osmotic power generators. ACS nano, 13(8), 8917-8925.

220. Li, J., Li, L., Xu, Y., Zhu, J., Liu, F., Shen, J., ... & Lin, J. (2022). MXene nanosheet stacks with tunable nanochannels for efficient molecular separation. Chemical Engineering Journal, 427, 132070.

221. Geng, X., Zhang, Y., Han, Y., Li, J., Yang, L., Benamara, M., ... & Zhu, H. (2017). Two-dimensional water-coupled metallic MoS2 with nanochannels for ultrafast supercapacitors. Nano letters, 17(3), 1825-1832.

222. Wang, B., Kalia, R. K., Nakano, A., & Vashishta, P. D. (2018). Dewetting of monolayer water and isopropanol between MoS2 nanosheets. Scientific Reports, 8(1), 16704.

223. Cheng, P., Chen, Y., Gu, Y. H., Yan, X., & Lang, W. Z. (2019). Hybrid 2D WS2/GO nanofiltration membranes for finely molecular sieving. Journal of Membrane Science, 591, 117308.

224. Danda, G., Masih Das, P., Chou, Y. C., Mlack, J. T., Parkin, W. M., Naylor, C. H., ... & Drndic, M. (2017). Monolayer WS2 nanopores for DNA translocation with light-adjustable sizes. ACS nano, 11(2), 1937-1945.

225. Yadav, P., Cao, Z., & Barati Farimani, A. (2021). DNA detection with single-layer Ti3C2 MXene nanopore. ACS nano, 15(3), 4861-4869.

226. Mojtabavi, M., VahidMohammadi, A., Liang, W., Beidaghi, M., & Wanunu, M. (2019). Single-molecule sensing using nanopores in two-dimensional transition metal carbide (MXene) membranes. ACS nano, 13(3), 3042-3053.

227. Prasongkit, J., Jungthawan, S., Amorim, R. G., & Scheicher, R. H. (2022). Single-molecule DNA sequencing using two-dimensional Ti2C (OH) 2 MXene nanopores: A first-principles investigation. Nano Research, 15(11), 9843-9849.

228. Seitak, A., Shanti, A., Al Adem, K., Farid, N., Luo, S., Iskandarov, J., ... & Lee, S. (2023). 2D MXenes for controlled releases of therapeutic proteins. Journal of Biomedical Materials Research Part A, 111(4), 514-526.

229. Chao, M., He, L., Gong, M., Li, N., Li, X., Peng, L., ... & Wan, P. (2021). Breathable Ti3C2T x MXene/Protein Nanocomposites for Ultrasensitive Medical Pressure Sensor with Degradability in Solvents. ACS nano, 15(6), 9746-9758.

230. Rastin, H., Zhang, B., Mazinani, A., Hassan, K., Bi, J., Tung, T. T., & Losic, D. (2020). 3D bioprinting of cell-laden electroconductive MXene nanocomposite bioinks. Nanoscale, 12(30), 16069-16080.